RADAR OBSERVATIONS OF GRAVITY WAVES IN THE MESOSPHERE

by
MAMORU YAMAMOTO

December 1987

Radio Atmospheric Science Center,
Kyoto University, Uji, Kyoto 611, JAPAN

RADAR OBSERVATIONS OF GRAVITY WAVES IN THE MESOSPHERE

by
MAMORU YAMAMOTO

December 1987

Radio Atmospheric Science Center,
Kyoto University, Uji, Kyoto 611, JAPAN

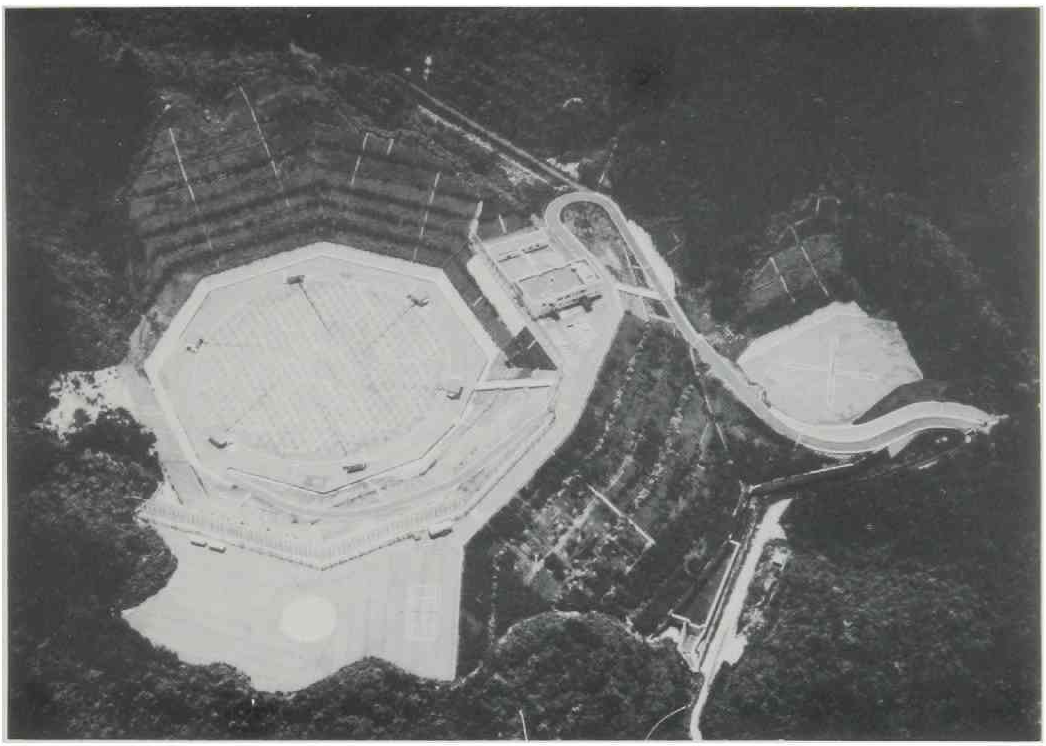

Shigaraki MU (Middle and Upper atmosphere) observatory of Radio Atmospheric Science Center, Kyoto University (34°51′N, 136°06′E).

Acknowledgements

The author wishes to express his sincere appreciation to Professor Susumu Kato for his guidance, inspiration and stimulating supervision in the present work, and for the careful reading of the manuscript.

The author deeply thanks Professors Iwane Kimura and Hiroshi Matsumoto for many important advices in performing the present work.

Special thanks are due to Dr. Toshitaka Tsuda for his kind guidance, continuous encouragements throughout the present work, and careful reading of the manuscript. The author thanks Drs. Shoichiro Fukao and Toru Sato for useful discussions, criticism and careful reading of the manuscript.

The author thanks Professor Adolf Ebel and Drs. Basil H. Briggs, William L. Oliver and Thomas E. VanZandt for discussions and careful reading of the manuscript. Thanks are also due to Drs. David C. Fritts, J. Klostermeyer and Richard J. Doviak for helpful discussions and suggestions. The author wishes to thank Dr. Peter T. May for cooperative studies of the estimation error of spectral parameters and careful reading of the manuscript.

The author is grateful to Messrs. Minoru Okumura, Yasushi Ayaki, Shigeki Morimoto, Toshio Nishida and Kouhei Hasegawa for providing fine software to control the MU radar system, to Messrs. Rei Ito and Takuji Nakamura for helping the continuous operation of the Kyoto meteor radar, to Mr. Takashi Inoue for his help in drawing figures and careful reading of the manuscript, to Dr. Masao Kitano for his technical support in typesetting the present text by using TEX.

The author is indebted to all staff of Radio Atmospheric Science Center, Kyoto University and operators from Mitsubishi Electric Corporation for the countless effort to maintain and operate the MU radar.

Part of computations of the present work were performed at the Data Processing Center, Kyoto University. The MU radar belongs to, and is operated by the Radio Atmospheric Science Center, Kyoto University.

Abstract

The altitude region from 10 to 120 km of the earth's atmosphere, the stratosphere, mesosphere and lower thermosphere, is called the middle atmosphere. The remote-sensing of wind velocities in this region by using coherent radars has been carried out for more than ten years, and provided data with better time-height resolution than that of the *in situ* observations with rockets and/or balloons. Radio Atmospheric Science Center, Kyoto University constructed the Kyoto meteor radar in Shigaraki, Shiga prefecture (35°N, 136°E) in 1977. The meteor radar observes wind velocities in 80–110 km region by utilizing meteor trails as a tracer. In 1982–1985, the Middle Atmosphere Program (MAP) was carried out as the first international project to investigate the middle atmosphere from various aspects. The MU (Middle and Upper atmosphere) radar was completed in 1984 as one of the MAP activities in Japan.

Recently, theoretical studies have revealed that the mean zonal wind in the mesosphere is decelerated by the breaking of gravity waves which is generated in the lower atmosphere. It is required to study the gravity waves in the middle atmosphere in order to understand the global circulation of the earth's atmosphere. The present thesis is concerned with radar observations of gravity waves in the mesosphere by using the MU radar and the Kyoto meteor radar.

After showing the system configuration of the MU radar and data processing techniques, the estimation error of the spectral parameters are discussed by means of computer simulations. We have also investigated a technique to achieve the theoretical lower bound of the estimation error. As the performance evaluation of the MU radar, comparison observations between the MU radar and the Kyoto meteor radar were carried out on 14–15 August 1984. Both facilities have provided fairly consistent wind profiles in 65–105 km region. The wind profile observed by the the meteorological rocket sounding has shown overall continuity to the winds observed by the MU radar.

The MU radar observations in the mesosphere with good time-height resolution have found gravity waves in the wind fields. We could observe the intrinsic frequency and horizontal propagation direction of the gravity waves as well as the vertical wavelength and phase velocity. By assuming a monochromatic gravity wave in the wind fields, the dynamic stability of the atmosphere is calculated, and it was shown that turbulence layers in the mesosphere appeared around the most unstable altitudes. Large wind fluctuations were found in the radial wind velocities when the inertia gravity wave generated the region with the negative Richardson number. Although the nature of the wind fluctuations was not determined, it was a clear evidence of the gravity wave saturation in the mesosphere.

A full-correlation analysis has been applied to the echo power fluctuations of the MU radar data in order to investigate the horizontal motion and structure of the scattering region. It was shown that the horizontal motion did not agree with the background wind velocity, but with the horizontal propagation of the saturated gravity wave. The observed scattering region seemed to be associated with the region where turbulence was being generated by the saturated gravity wave.

The data obtained by the continuous observation of the Kyoto meteor radar in 1983–1985 has been utilized for the gravity wave observations. The annual average of power spectral densities of wind fluctuations were calculated in 1983 and 1984, which showed consistent results with other observations performed with MST and partial reflection radars. The horizontal phase velocity of gravity waves has been observed by dividing the observation range of the Kyoto meteor radar according to the horizontal distance from the radar. Gravity waves with westward phase velocities were more frequently observed than that with eastward ones in the whole observation period.

Contents

List of Figures

List of Tables

Chapter 1

General introduction

1.1 The middle atmosphere

Figure 1.1 shows a typical height profile of temperature in the mid-latitude region. The atmosphere is classified according to the temperature profile [e.g., Kato, 1980]. The region from the ground up to approximately 11 km is called the troposphere, where the temperature decreases at about 6.5°C per 1 km. Almost all the solar radiation reaches the ground and heats it. The atmospheric layer just above the ground is heated and can become unstable. Thus, convection is generated in the troposphere. The temperature of an air parcel decreases as it moves upward because of the adiabatic expansion. Water vapor in the air, on the other hand, releases heat when it condenses. The temperature lapse rate in the troposphere is thus determined by the balance of these effects.

The region above 10–15 km is called the stratosphere, and the boundary layer is named as the tropopause. Just above the troposphere, the temperature is almost constant with height till 20 km, and then increases up to approximately 270 K at around 50 km. This region is very stable and no convective motion is generated because of the structure of the temperature profile. Vertical mass transport is suppressed and we can recognize laminar structures like the ozone and aerosol layers. The upper boundary of the stratosphere is called the stratopause.

Above the stratopause, the temperature lapse rate becomes negative again, and we find a globally averaged temperature minimum of approximately 180 K around 80 km. This region is called the mesosphere and its upper boundary is called the mesopause. Although the temperature lapse rate is negative, the gentle lapse rate does not make this region unstable. Strong turbulence is a characteristic feature of the mesosphere, which seems to be generated by the

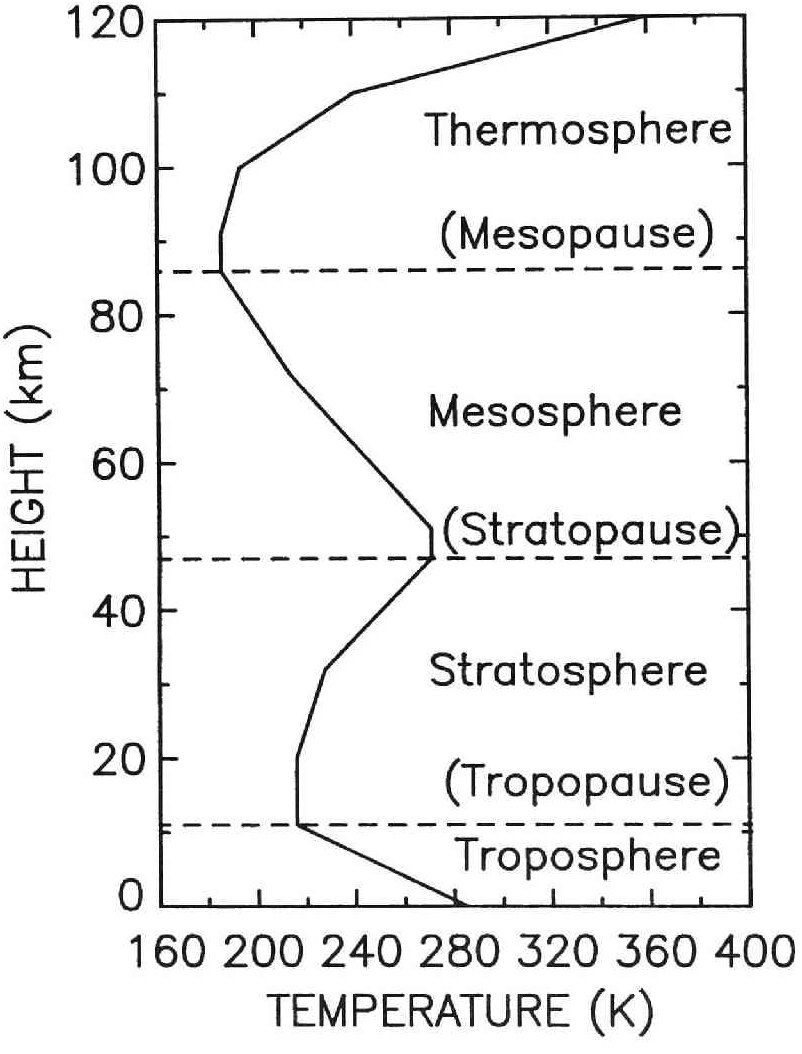

Figure 1.1: Temperature distribution and nomenclature of the earth's atmosphere [U.S. Standard Atmosphere, 1976].

breaking of gravity waves.

The region above the mesopause is called the thermosphere. The temperature in this region rapidly increases with height because constituents of the atmosphere are ionized and strongly heated by solar ultraviolet (UV) and extreme ultraviolet (EUV) radiation and solar X-rays. The vertical transport due to macroscopic motions of the atmosphere becomes less important in this region than the vertical diffusion because the mean free path of the molecule increases according to the decreasing density.

There exists another classification for the atmosphere. The region from 10 to 120 km is called the middle atmosphere, which consists of the stratosphere, mesosphere and the lower thermosphere. It is needless to say that the energy source for driving the atmospheric circulation is the solar radiation, which is absorbed in three regions in the atmosphere [e.g., Matsuno and Shimazaki, 1981]. The thermosphere is the region where the UV and X-rays with wavelength less than 175 nm are absorbed by the atomic oxygen and nitrogen. The UV rays with wavelength less than approximately 300 nm are absorbed in the lower layers of the middle atmosphere. It is known that the temperature profile is determined by the radiative equilibrium, and the peak around the stratopause is generated through UV absorption by ozone (O_3). The heating due to the UV radiation is the major energy source in the middle atmosphere. The visible and infrared part of the solar radiation is mainly absorbed at or near the surface of the earth. This heating generates the convective motion and the energy is transported vertically to maintain the temperature gradient in the troposphere. The temperature peaks shown in Fig. 1.1 correspond to these three regions of the heat source in the atmosphere.

Figure 1.2 shows distribution of the mean zonal wind at the solstice as a latitude-height section [CIRA, 1972]. Note that 'E' and 'W' in the figure correspond to easterly (westward) and westerly (eastward) winds, respectively. We recognize two different wind systems in the lower and middle atmosphere. Near the tropopause (10 km), there are eastward jets in both summer and winter hemisphere. The other wind system is in the mesosphere (60–70 km). We find strong eastward and westward wind in winter and summer hemisphere, respectively. The solar heating near the surface generates hot equator and cold both summer and winter poles. Considering the relation between mean wind and horizontal distribution of the temperature, the heating corresponds to the strong eastward jets in the mid-latitude near the tropopause. Around 50 km, the heating of the ozone layer generates the hot summer pole and the cold winter pole. This corresponds to the increasing westward and eastward mean wind up to 60–70 km in the summer and winter hemisphere, respectively. These wind systems can be basically explained by the radiative equilibrium of

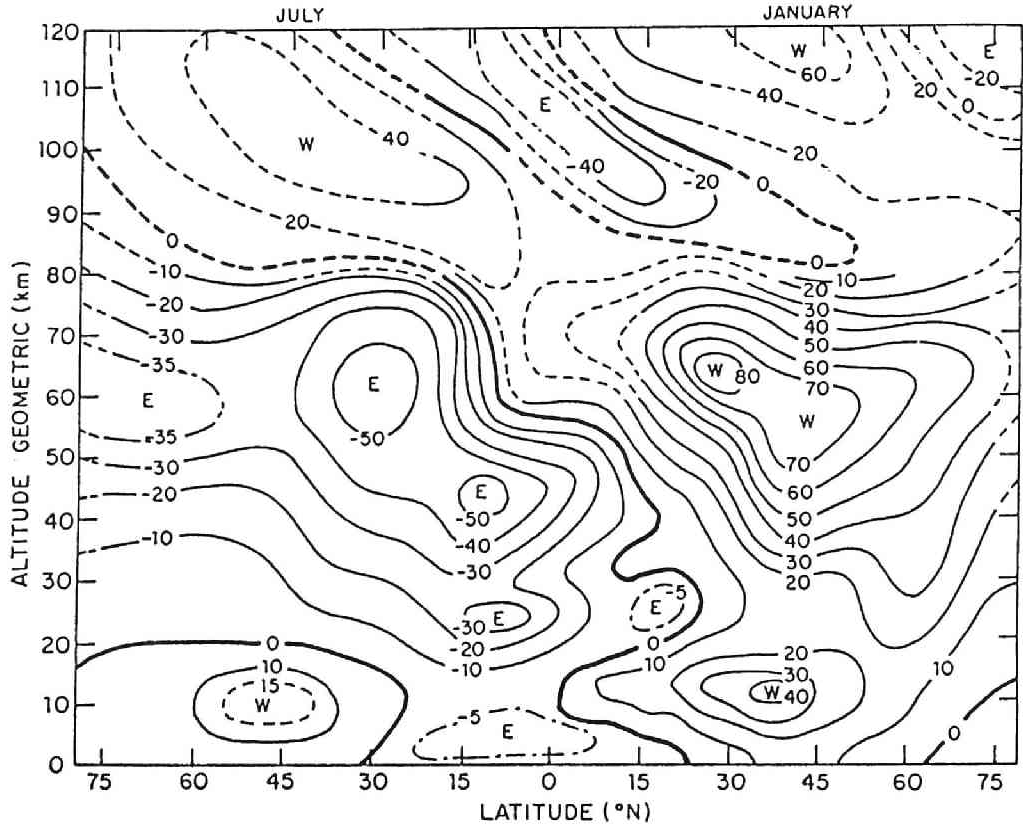

Figure 1.2: Zonal wind contours as a function of height and latitude for July and January [CIRA, 1972]. The positive and negative zonal winds correspond to westerly (eastward) and easterly (westward) winds, respectively.

the earth's atmosphere.

The main characteristics of the middle atmosphere is that many kinds of waves with various temporal and spatial scales are superimposed on the mean winds. These waves are classified according to their typical periods as planetary waves (> 1 day), atmospheric tides and gravity waves (24 hr~10 min). Turbulence is also an important process causing wind perturbations. When the atmospheric waves propagate vertically without being attenuated, their amplitudes increase with height as the background density decreases. If the amplitude exceeds a certain value, the waves are saturated and give their energy to the background winds, other waves and turbulence through either convective or dynamic instabilities. Therefore, the study of interactions of atmospheric waves with mean winds and waves become as important as the investigation of the excitation, propagation and dissipation of single waves. As regards these waves, many theoretical and experimental studies have been done concerning the behavior of gravity waves. The studies stressed the importance of gravity waves in controlling the large scale motions in the middle atmosphere.

Here, we briefly review the atmospheric dynamics including the basic characteristics of gravity waves by following Gossard and Hooke [1975] and Beer [1974]. Atmospheric motions are described by the following hydrostatic and thermodynamic equations for variables $\boldsymbol{v} = (u, v, w)$, T, p and ρ, which are the velocity vector, temperature, pressure and density, respectively. The basic equations are:

$$\rho\left(\frac{\mathrm{d}\boldsymbol{v}}{\mathrm{d}t}\right) + \nabla p - \rho g + 2\rho\boldsymbol{\Omega}_z \times \boldsymbol{v} = \boldsymbol{F} \tag{1.1}$$

$$\frac{\mathrm{d}\rho}{\mathrm{d}t} + \rho\nabla\cdot\boldsymbol{v} = 0 \tag{1.2}$$

$$\tilde{Q} = C_v\rho\frac{\mathrm{d}T}{\mathrm{d}t} - \frac{p}{\rho}\frac{\mathrm{d}\rho}{\mathrm{d}t} \tag{1.3}$$

$$p = \rho RT \tag{1.4}$$

where x, y and z-axes are eastward, northward and upward, respectively, and $\mathrm{d}/\mathrm{d}t = \partial/\partial t + \boldsymbol{v}\cdot\nabla$ is the total derivative following the atmospheric motion. The first equation is the equation of motion, in which $\boldsymbol{F}$ is external force and the term $2\rho\boldsymbol{\Omega}_z \times \boldsymbol{v}$ represents the Coriolis force, where $\boldsymbol{\Omega}_z$ is the vertical component of angular velocity of the earth $\boldsymbol{\Omega}$ in radians. The second equation is the equation of continuity which describes the conservation of mass in the air parcel. The first law of the thermodynamics is Eq. (1.3), where $\tilde{Q}$ and C_v are the heat input per unit mass and time and the specific heat capacity per unit mass at constant volume, respectively. Also, we need the equation of state for the ideal gas as shown in Eq. (1.4), where R is the gas constant. When

$\boldsymbol{F} = 0$ and $\tilde{Q} = 0$, an inviscid and adiabatic atmosphere, this set of equations is closed.

When we assume that the zero-order state is a steady, frictionless, horizontally homogeneous, static medium, we find

$$\frac{\partial p_0}{\partial z} = -\rho_0 g \tag{1.5}$$

which is called hydrostatic equilibrium, where the subscript 0 denotes the zero-order state. Integration of Eq. (1.5) with the aid of Eq. (1.4) yields

$$p_0(z) = p_s \exp\left(-\int \frac{dz}{H}\right) \tag{1.6}$$

$$\rho_0(z) = \rho_s \frac{T_s}{T_0} \exp\left(-\int \frac{dz}{H}\right) \tag{1.7}$$

where p_s and ρ_s are pressure and density at a reference height, respectively, and H is called a scale height defined by

$$H = \frac{RT_0}{g} \tag{1.8}$$

Equation (1.1) can be used to find the components of the wind that exists when the pressure gradient forces are balanced with Coriolis forces. This wind is called the geostrophic wind and is expressed as

$$u_0 = -\frac{1}{f\rho}\frac{\partial p_0}{\partial y} \tag{1.9}$$

$$v_0 = \frac{1}{f\rho}\frac{\partial p_0}{\partial x} \tag{1.10}$$

$$w_0 = 0 \tag{1.11}$$

where $f = 2\Omega \sin\phi$ is the inertial frequency determined by the angular velocity of the earth Ω and the latitude ϕ. Considering Eqs. (1.4) and (1.5), we can write

$$\frac{\partial}{\partial z}(\boldsymbol{U}_g/T_0) = -\frac{g}{fT_0}\left(\frac{\partial T_0}{\partial y}, -\frac{\partial T_0}{\partial x}, 0\right) \tag{1.12}$$

where $\boldsymbol{U}_g = (u_0, v_0, w_0)$. This equation relates the vertical shear in the geostrophic wind to the horizontal temperature gradients, and is called "thermal wind equation" [Beer, 1974].

The potential temperature θ is the temperature of a dry air parcel when the parcel is brought adiabatically to the reference level of 1000 mb, which is written as follows

$$\theta = T(1000/p)^{\frac{\gamma-1}{\gamma}} \tag{1.13}$$

where $\gamma = C_p/C_v$, and C_p is the specific heat capacity at constant pressure. The static stability of the atmosphere is expressed by the vertical derivative of θ. When $\partial\theta/\partial z > 0$, the air parcel is stable and shows an oscillation if the parcel is displaced vertically. The frequency of the oscillation is called Brunt-Väisälä frequency N, which is given by

$$N^2 = \frac{g}{\theta}\frac{\partial\theta}{\partial z} \tag{1.14}$$

On the other hand, the dynamic stability of the atmosphere is described by the Richardson number:

$$Ri = \left(\frac{g}{\theta}\frac{\partial\theta}{\partial z}\right) \Big/ \left[\left(\frac{\partial u}{\partial z}\right)^2 + \left(\frac{\partial v}{\partial z}\right)^2\right] \tag{1.15}$$

The Richardson number represents the ratio of the work required to interchange vertically adjacent air parcels against the acceleration of gravity, to the kinetic energy available to do the work [Gossard and Hooke, 1975]. When $Ri < 1/4$, the atmosphere becomes dynamically unstable and generates dynamical instabilities such as the Kelvin-Helmholtz instability [Drazin, 1958].

1.2 Gravity waves

Assuming an inviscid atmosphere and adiabatic process, we can obtain perturbation equations from Eq. (1.1)–(1.4). Hereafter, we use u, v, w, p and ρ to show the first order perturbations. It is convenient to use the transform of the variables

$$\begin{aligned} &U \equiv (\rho_0/\rho_s)^{1/2}u,\ V \equiv (\rho_0/\rho_s)^{1/2}v,\ W \equiv (\rho_0/\rho_s)^{1/2}w, \\ &P \equiv (\rho_0/\rho_s)^{-1/2}p,\ Q \equiv (\rho_0/\rho_s)^{-1/2}\rho \end{aligned} \tag{1.16}$$

where ρ_0 is the zero-order state of density, and ρ_s is the density at some reference height. The perturbation equations are given as follows:

$$\frac{\mathrm{D}U}{\mathrm{D}t} + \frac{1}{\rho_s}\frac{\partial P}{\partial x} - fV = 0 \tag{1.17}$$

$$\frac{\mathrm{D}V}{\mathrm{D}t} + \frac{1}{\rho_s}\frac{\partial P}{\partial y} + fU = 0 \tag{1.18}$$

$$\frac{\mathrm{D}W}{\mathrm{D}t} + \frac{1}{\rho_s}\left(\frac{\partial}{\partial z} - \Gamma\right)P + \frac{g}{\rho_s}Q = 0 \tag{1.19}$$

$$\frac{1}{\rho_s c_s^2}\frac{\mathrm{D}P}{\mathrm{D}t} + \frac{\partial U}{\partial x} + \frac{\partial V}{\partial y} + \left(\frac{\partial}{\partial z} - \Gamma\right)W = 0 \tag{1.20}$$

$$\left(\frac{\mathrm{D}^2}{\mathrm{D}t^2} + N^2\right)W + \frac{1}{\rho_s}\frac{\mathrm{D}}{\mathrm{D}t}\left(\frac{\partial}{\partial z} + \Gamma\right)P = 0 \tag{1.21}$$

where c_s is the speed of sound given by $c_s^2 = \gamma R T_0$. Γ is the Eckert's coefficient given by

$$\Gamma = \frac{g}{2c_s^2} = \frac{1}{2\gamma H} \tag{1.22}$$

and $\mathrm{D}/\mathrm{D}t$ is the total derivative following the zero-order flow shown as

$$\frac{\mathrm{D}}{\mathrm{D}t} = \frac{\partial}{\partial t} + u_0\frac{\partial}{\partial x} + v_0\frac{\partial}{\partial y} \tag{1.23}$$

In order to investigate the characteristics of gravity waves, we assume the propagation of waves to be in the x-direction and $v_0 = 0$. This provides solutions of the form

$$\begin{aligned} U &= A_U \exp[\mathrm{i}(kx + mz - \sigma t)] \\ V &= A_V \exp[\mathrm{i}(kx + mz - \sigma t)] \\ W &= A_W \exp[\mathrm{i}(kx + mz - \sigma t)] \\ P &= A_P \exp[\mathrm{i}(kx + mz - \sigma t)] \\ Q &= A_Q \exp[\mathrm{i}(kx + mz - \sigma t)] \end{aligned} \tag{1.24}$$

for variables U, V, W, P and Q, where A_U, A_V, A_W, A_P and A_Q are the amplitude of each variable, and k, m and σ are horizontal and vertical wavenumber and frequency observed from the ground, respectively. When the perturbations are small enough to allow the linear assumption, and the coefficients ρ_s, c_s, N and Γ are constant, we obtain a system of homogeneous polynomials from Eqs. (1.17)–(1.21). The dispersion equation of the waves can be calculated from the determinant of the coefficient matrix of the polynomials, and is described as follows:

$$m^2 = \frac{N^2 - \omega^2}{\omega^2 - f^2}k^2 + \frac{1}{c_s^2}(\omega^2 - N_a^2) \tag{1.25}$$

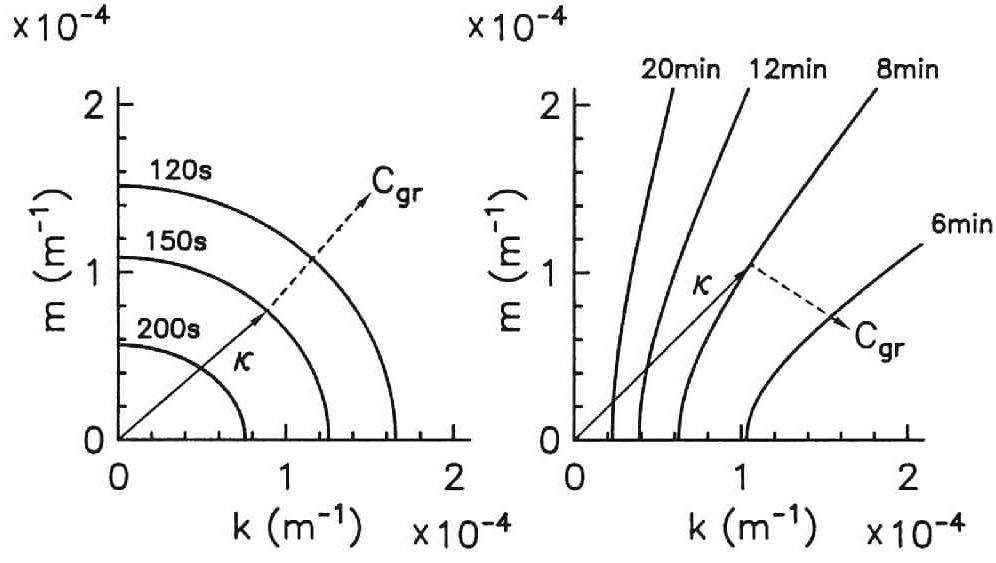

Figure 1.3: Dispersion relations of (left) acoustic waves and (right) gravity waves in the km-plane. Curves represent the propagation surfaces for waves in an isothermal atmosphere. The diagrams indicate the group velocity $\boldsymbol{C}_{gr}$ and wavenumber vector $\boldsymbol{\kappa}$. Wave periods are shown near the curves, and we assumed $N = 2.1 \times 10^{-2}$ [s^{-1}] and $f = 8.3 \times 10^{-5}$ [s^{-1}].

where $N_a^2 = N^2 + c_s^2\Gamma^2$. In this equation, ω is the frequency of the wave noted by an observer drifting with the zero-order flow, and is called the "intrinsic frequency". The relationship between ω and σ is

$$\omega = \sigma - u_0 k \tag{1.26}$$

This equation shows the Doppler shift of the wave.

As shown by Eq. (1.24), m should be real in order that the waves should propagate vertically. Otherwise, the waves die off exponentially with height (i.e., they are evanescent). From Eq. (1.25), we find that the condition for the propagating waves is that $\omega^2 > N_a^2$ or $N^2 > \omega^2 > f^2$. Following Gossard and Hooke [1975], the wave is an acoustic wave when $\omega^2 > N_a^2$ and the dispersion relation between k and m becomes a family of ellipses as shown in Fig. 1.3. Because no acoustic wave can exist with frequencies below N_a, this parameter is called the acoustic cut-off frequency. The other case, $N^2 > \omega^2 > f^2$, corresponds to internal gravity waves, and the relation between k and m for the gravity waves is a family of hyperbolas as shown in Fig. 1.3. The restoring force of this wave is the gravity. A useful form of the dispersion equation for

gravity waves is

$$m^2 = \frac{N^2 - \omega^2}{\omega^2 - f^2} k^2 \tag{1.27}$$

The direction and speed of the energy transfer of the wave are described by the group velocity

$$\boldsymbol{C}_{gr} = \left(\frac{\partial \omega}{\partial k}, \frac{\partial \omega}{\partial m} \right) \tag{1.28}$$

rather than the phase velocity

$$\boldsymbol{C}_{ph} = \frac{\omega}{k^2 + m^2} (k, m) \tag{1.29}$$

In the km-plane, we find that the direction of $\boldsymbol{C}_{ph}$ is parallel to the wavenumber vector $\boldsymbol{\kappa}$, but $\boldsymbol{C}_{gr}$ is directed perpendicularly to the contours of constant ω. As shown in Fig. 1.3, therefore, the direction of $\boldsymbol{C}_{gr}$ for gravity waves is quite different from that of $\boldsymbol{C}_{ph}$ although $\boldsymbol{C}_{gr}$ for acoustic waves is in almost the same direction of $\boldsymbol{C}_{ph}$. It is a distinct characteristic of gravity waves that the direction of the energy flow is almost perpendicular to that of the phase propagation.

The amplitude of gravity waves also varies with vertical propagation. Considering Eqs. (1.7) and (1.16) and assuming an isothermal atmosphere, it is found that the amplitude of u, v and w is proportional to $\exp(z/2H)$. Figure 1.4 schematically shows the behavior of a gravity wave with downward phase propagation.

By using Eqs. (1.17)–(1.21) and (1.24), relationships between the variables of gravity waves are obtained as the "polarization equations", which are given as follows:

$$V = -\mathrm{i} \frac{f}{\omega} U \tag{1.30}$$

$$U = \frac{\omega k}{\rho_s (\omega^2 - f^2)} P \tag{1.31}$$

$$W = -\frac{\omega m'}{\rho_s (N^2 - \omega^2)} P \tag{1.32}$$

$$Q = -\mathrm{i} \frac{N^2 m'}{g (N^2 - \omega^2)} P \tag{1.33}$$

where $m' \equiv m + \mathrm{i}\Gamma$. Equation (1.30) shows that U and V are 90° out of phase and the ratio is proportional to f/ω, which means that the horizontal wind vector of a gravity wave moves elliptically with time and in the vertical direction. Assuming that the vertical wavelength of a gravity wave is less than

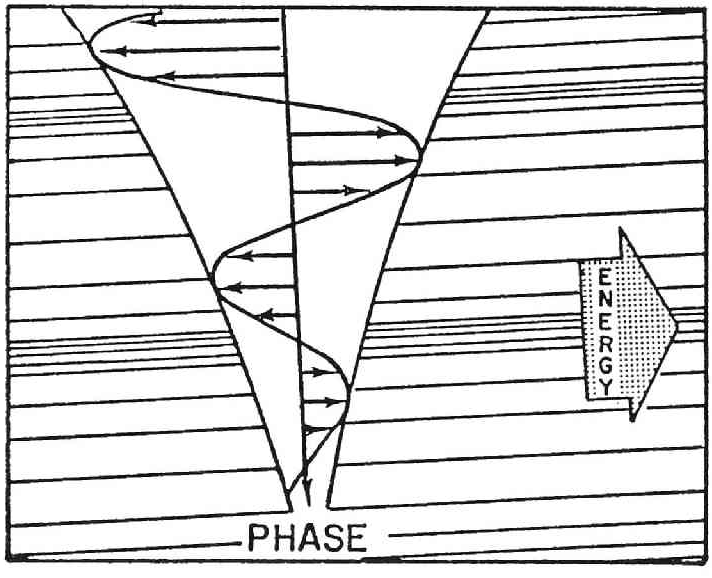

Figure 1.4: Pictorial representation of gravity waves. Instantaneous velocity vectors are shown, together with their instantaneous and over-all envelopes. Density variations are depicted by a background of parallel lines lying in surfaces of constant phase. Phase progression is essentially downward in this case, and energy propagation obliquely upwards. Note that the density and wind fluctuations are 90° out of phase [Hines, 1960].

the scale height H, we can assume $m' \approx m$. Thus, for typical gravity waves, we find from Eqs. (1.27) and (1.32) that

$$W = -\frac{k}{m}U \tag{1.34}$$

This means that the gravity wave is a transverse wave because the wave motion in the xz-plane is perpendicular to the wavenumber vector. It is also shown by Eqs. (1.33) and (1.34) that Q and U are 90° out of phase, which is recognized in Fig. 1.4.

Next, we discuss the dynamic stability of gravity waves which should be described by the Richardson number. Because the wave motion we consider is an adiabatic process, the potential temperature is conserved, so we can write,

$$\frac{\mathrm{D}\theta}{\mathrm{D}t} = 0 = \frac{\mathrm{D}\theta'}{\mathrm{D}t} + w\frac{\partial\theta_0}{\partial z} \tag{1.35}$$

where $\theta = \theta_0 + \theta'$, and θ' is the perturbed component of θ due to the wave motion. By using the vertical displacement η, we can write that $w = \mathrm{D}\eta/\mathrm{D}t$ in Eq. (1.35). Then, we see that $\theta - \theta_0 = -\eta(\partial\theta_0/\partial z)$. If $\partial\theta_0/\partial z$ is constant, it follows that

$$\frac{\partial\theta}{\partial z} = \frac{\partial\theta_0}{\partial z}\left(1 - \frac{\partial\eta}{\partial z}\right) \tag{1.36}$$

By using Eq. (1.34) and the relation between w and η, the polarization equation for the displacement of gravity waves is

$$\eta = -\mathrm{i}\frac{k}{\omega m}u \tag{1.37}$$

From Eq. (1.15), the Richardson number modified by the gravity wave motion is therefore,

$$Ri = \frac{\frac{g}{\theta_0}\frac{\partial\theta_0}{\partial z}\left(1 - \frac{k}{\omega}u\right)}{\left[\frac{\partial}{\partial z}(u + u_0)\right]^2 + \left[\frac{\partial}{\partial z}(v + v_0)\right]^2} \tag{1.38}$$

When a gravity wave propagates in the background wind $u_0(z)$ which is a function of height, the frequency σ observed from the ground is invariant, but the intrinsic frequency ω varies as

$$\omega = \sigma - ku_0(z) = k\{C - u_0(z)\} \tag{1.39}$$

where $C = \sigma/k$ is the horizontal phase velocity of the gravity wave. Following Gossard and Hooke [1975], we can refer to the dispersion equation of Eq. (1.27)

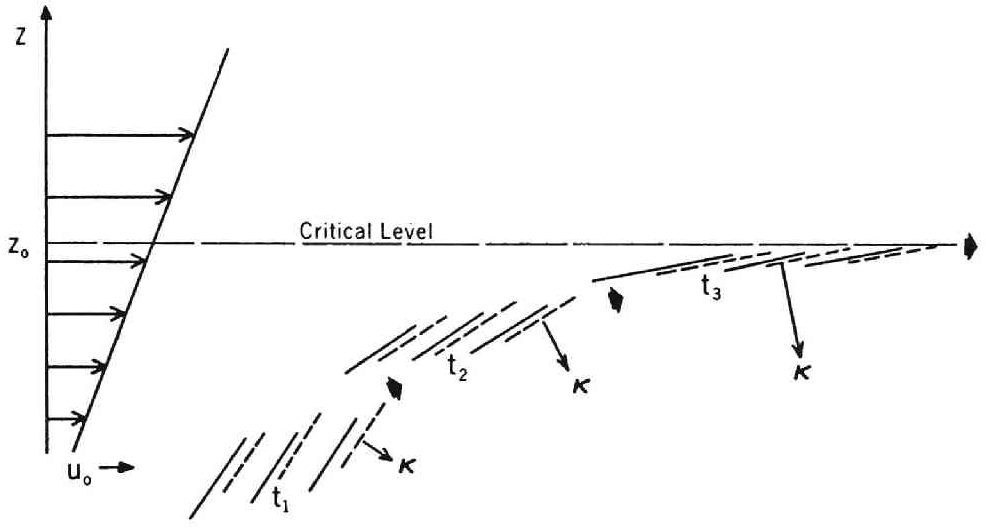

Figure 1.5: Schematic of progression of wave packet upward toward a critical level z_0 at successive times t_1, t_2 and t_3. Dashed lines represent new position of equiphase contours a moment after that represented by the solid lines [Gossard and Hooke, 1975].

when the vertical shear of u_0 is small. Figure 1.5 schematically shows a wave packet of the gravity wave which is propagating upward with the background wind increasing with height. It is found from Eq. (1.39) that the intrinsic frequency decreases as the mean wind velocity u_0 approaches the phase velocity C. This means that the vertical wavelength and the vertical phase velocity become smaller. The height where $C = u_0$ is called the "critical level", which corresponds to $\omega = 0$, and gravity waves cannot propagate across the critical level. Thus, in the real atmosphere, the wave is dissipated, and deposits the momentum flux $\rho_0\overline{uw}$ to the mean flow. The acceleration of the mean flow is given by the following equation:

$$\frac{\partial u_0}{\partial t} = -\frac{1}{\rho_0}\frac{\partial}{\partial z}\rho_0\overline{uw} \tag{1.40}$$

As shown in Fig. 1.2, in the 60–70 km region, we recognize the strong eastward and westward wind systems in the winter and summer hemisphere, respectively. Basically, these wind systems should be generated by the major heat sources in the atmosphere, i.e. the ozone layer, as shown in Section 1.1. Considering the thermal wind relation of Eq. (1.12), the heating of the ozone layer in the middle atmosphere generates the hot summer pole and the cool winter pole. This results in the increasing zonal wind velocities up to 60–70 km

in both hemispheres. Above this region, however, the zonal wind velocity decreases with altitude, and direction of the wind is reversed around 80 km. The thermal wind relation, therefore, requires that the temperature in the upper mesosphere should be higher in winter than in summer. Observations show the cooler summer pole near the mesopause [e.g., Murgatroyd, 1969]. In order to maintain the reversed horizontal distribution of temperature, some dynamic process is required to decelerate the mean zonal wind because the temperature distribution in the mesosphere is not in the radiative equilibrium, and the thermal wind equation describes just the balance between distributions of mean wind velocity and temperature.

Leovy [1964] simulated the departure from radiative equilibrium by using Rayleigh friction, which did not represent any relevant physical mechanism. Houghton [1978] suggested the importance of the gravity wave breaking in explaining the reversal of the vertical shear of the mean zonal wind. Lindzen [1981], Holton [1982] and Matsuno [1982] have parameterized the momentum deposition by the upgoing gravity wave breaking, resulting in the deceleration of the mean winds.

Fig. 1.6 illustrates the schematic diagram of the linear saturation theory proposed by Lindzen [1981]. Eqs. (1.17)–(1.21) are modified for the gravity waves with variable N and u_0 when we consider the gravity wave propagating in the x-direction and neglecting the Coriolis force ($f = 0$). Here, we assume solutions which are proportional to $\exp[\mathrm{i}(kx - \sigma t)]$, and obtain the following equation [Gossard and Hooke, 1975]

$$\frac{\partial^2 W}{\partial z^2} + \left[\frac{N^2}{(u_0 - C)^2} - k^2 - \frac{u_0''}{u_0 - C} - \frac{2\Gamma u_0'}{u_0 - C}\right] W = 0 \qquad (1.41)$$

where primes ($'$) denote derivatives with respect to the z-axis. This is known as the Taylor-Goldstein equation which describes the vertical structure of the vertical perturbation velocity of gravity waves. For our purposes, however, it is reasonable to assume that N^2 is constant, u_0'' is small and H is large. Following Holton [1982] and Fritts [1984], we may neglect k^2, and Eq. (1.41) becomes

$$\frac{\partial^2 W}{\partial z^2} + \left[\frac{N^2}{(u_0 - C)^2}\right] W = 0 \qquad (1.42)$$

This equation has the approximate WKB solution [Bender and Orszag, 1978] of

$$W = Am^{1/2} \exp\left(\mathrm{i} \int m dz\right) \qquad (1.43)$$

where m is the local vertical wavenumber of gravity waves given by

$$m^2 = \frac{N^2}{(u_0 - C)^2} \qquad (1.44)$$

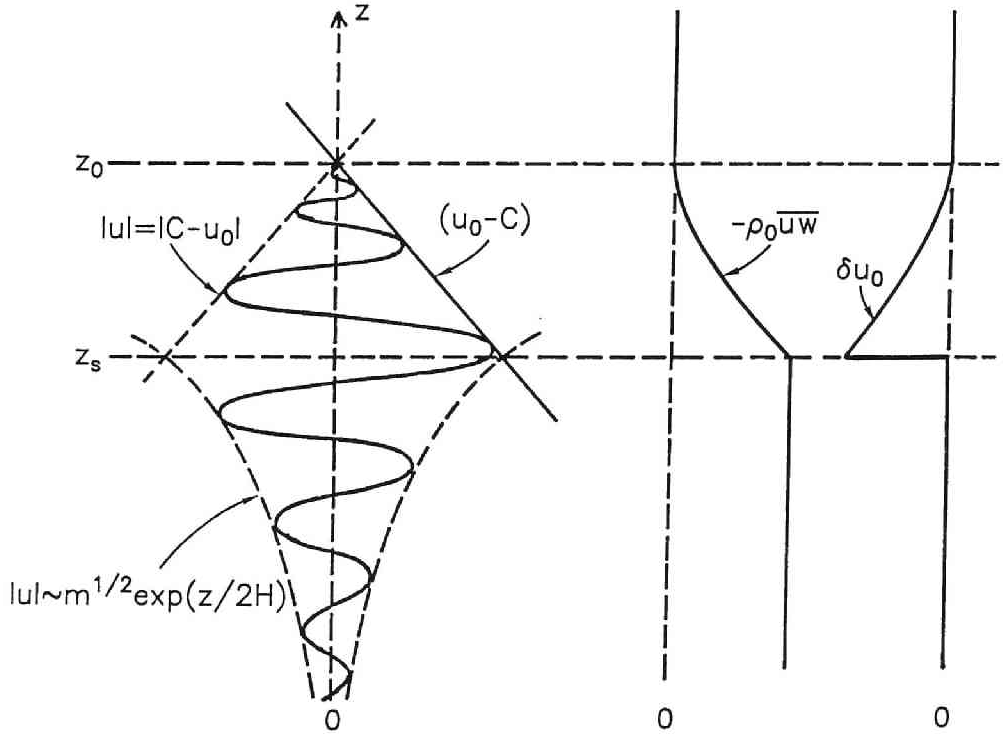

Figure 1.6: Schematic of the growth with height and saturation of a gravity wave due to convective instability. Wave damping produces both a divergence of the vertical flux of horizontal momentum and an acceleration of the mean flow δu_0 toward the phase speed of the wave. Deceleration and diffusion cease above the critical level $z = z_0$ in the linear theory [Fritts, 1984].

Following Lindzen [1981], the basic premise of the linear saturation theory is that convectively unstable regions appearing within the wave field result in the production of turbulence [Fritts, 1984]. Because the atmosphere is statically stable when $\partial\theta/\partial z > 0$, we can write this condition from Eqs. (1.36), (1.37) and (1.39) as follows;

$$| u | \leq | C - u_0 | \tag{1.45}$$

As shown in Fig. 1.6, we assume that gravity waves propagate from source regions until they achieve saturation amplitudes at $z = z_s$, and thereafter, wave amplitudes are limited by the saturation conditions of Eq. (1.45). From Eqs. (1.34), (1.44) and (1.45), saturation amplitudes of gravity waves are

$$| u_s | = | C - u_0 | \tag{1.46}$$

and

$$w_s = -\frac{k}{m}u_s = \frac{k}{N}(u_0 - C)^2 \tag{1.47}$$

The momentum flux associated with the saturated gravity wave is then

$$\rho_0\overline{u_s w_s} = \frac{\rho_0}{2}u_s w_s = -\frac{\rho_0}{2}\frac{k}{N}(u_0 - C)^3 \tag{1.48}$$

Using Eq. (1.40), the induced mean wind acceleration due to the wave saturation is

$$\frac{\partial u_0}{\partial t} = -\frac{k(u_0 - C)^2}{2N}\left[\frac{u_0 - C}{H} - 3\frac{\partial u_0}{\partial z}\right] \tag{1.49}$$

In an environment where $u_0 - C$ varies little, the induced mean wind acceleration is approximately constant with height and given by

$$\frac{\partial u_0}{\partial t} \approx \frac{\overline{u_s w_s}}{H} = -\frac{k(u_0 - C)^3}{2NH} \tag{1.50}$$

1.3 Radar technique

The middle atmosphere was called the "ignorosphere" because there were few observation techniques available in this region. Direct measurements of the atmosphere using balloons, aircraft, and rockets can observe the middle atmosphere with a good height resolution, although it is difficult to obtain the data continuously in time. On the other hand, the ground-based observations using radio and optical remote sensing techniques can provide data with a relatively good temporal and spatial resolution although it is not easy to move the observational sites.

MST radars The MST (Mesosphere Stratosphere Troposphere) radars are ultrasensitive VHF (30–300 MHz) and UHF (300–3000 MHz) radars to study the weak backscattering arising from refractive index fluctuations in the neutral atmosphere and lower ionosphere [Balsley and Gage, 1980]. The radial wind velocity is measured from the mean Doppler frequency shift of the return signal of the MST radar. Turbulence intensity can be deduced from the width or power of the echo spectrum [e.g., Hocking, 1985]. The first observations with MST radars were carried out by Woodman and Guillén [1974] at Jicamarca (12°S, 77°W). They obtained wind velocities in the mesosphere with time resolution of 1 min, which allows the study of atmospheric waves from gravity waves to tidal and planetary waves as well as the prevailing winds.

We consider the radar echo power P_r from isotropic scattering volume. The scattering cross-section per unit scattering volume is called "reflectivity" η and has a dimension of $[m^2/m^3]$. Because echo power is proportional to the scattering volume, the radar equation for uniformly distributed targets is

$$P_r = \frac{\pi}{64} \frac{P_t A_e \Delta r}{r^2} \eta \tag{1.51}$$

where P_t, A_e, r and Δr are transmitted power, effective area of antenna, range and range resolution, respectively [Probert-Jones, 1962].

The volume reflectivity η is expressed in terms of the three-dimensional wavenumber $\boldsymbol{K}$ of turbulent fluctuations as

$$\eta = \frac{\pi^2}{2} K^4 \Phi_n(\boldsymbol{K}) \tag{1.52}$$

where $\boldsymbol{K} = \boldsymbol{K}_i - \boldsymbol{K}_s$, and $\boldsymbol{K}_i$ and $\boldsymbol{K}_s$ are the wavenumber of incident and scattered radio wave, respectively [Tatarskii, 1971]. In the case of the backscatter, $\boldsymbol{K}_s$ is equal to $-\boldsymbol{K}_i$, thus, $\boldsymbol{K}$ becomes equal to $2\boldsymbol{K}_i$. K is expressed in terms of the wavelength of the radio wave λ as

$$K = \mid \boldsymbol{K} \mid = 2\left(\frac{2\pi}{\lambda}\right) = \frac{4\pi}{\lambda} \tag{1.53}$$

The radio wave is backscattered mainly by the $\lambda/2$ Fourier component of irregularities of atmospheric refractive index due mainly to turbulence. It is also known that the index of refraction of the atmosphere is expressed as a function of pressure P [mb], temperature T [K], water vapor pressure e [mb], and electron density N_e $[m^{-3}]$ as follows [e.g., Röttger, 1980]:

$$n = 1 + \frac{3.73 \times 10^{-1} e}{T^2} + \frac{7.76 \times 10^{-5} P}{T} - \frac{40.3 N_e}{f^2} \tag{1.54}$$

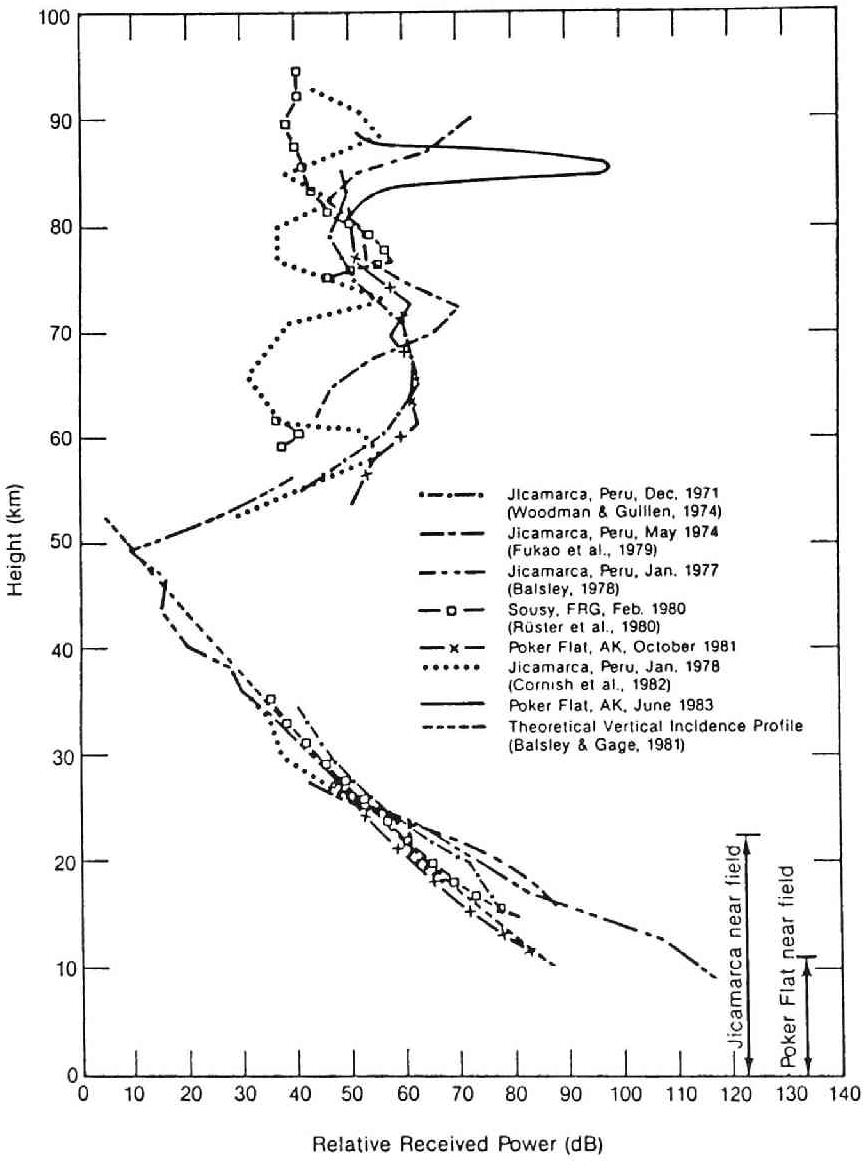

Figure 1.7: Relative echo power profiles for various MST radar facilities (Curves normalized at lower stratospheric heights) [Gage and Balsley, 1984].

where f is transmission frequency [Hz] of the radar.

The MST technique is capable of obtaining useful returns over the height range of 1–100 km. Figure 1.7 shows the relative echo power profiles for various MST radar facilities [Gage and Balsley, 1984], and indicates intense echo power in the lower stratosphere (10–30 km) and the mesosphere (60–90 km). Echoes coming from heights below the stratopause ($\simeq$ 50 km) arise primarily from refractive index fluctuations due to small-scale turbulence in the inertial subrange. Water vapor pressure is usually the most important factor in the lower troposphere because of the high humidity. Above this region, pressure (dry air term) dominates up to the stratopause. Echoes returned from the mesosphere are normally observed only during daylight hours, and is much stronger than the level of incoherent scatter caused by free electrons. The mesospheric echo arise from the neutral turbulence fluctuations which is enhanced by free electrons at these heights. The most difficult region to be observed by the MST radar technique is the region near the stratopause because of the combined effect of the exponentially decreasing atmospheric density and the lack of sufficient free electrons [Balsley and Gage, 1980].

Meteor radars One of the other ground-based techniques is a meteor radar. When a meteoroid is attracted by the earth's gravitational force and penetrates into the atmosphere, it ionizes neutral particles of the atmosphere and produces an ionization column, which is called a meteor trail. Back-scatter echoes are obtained from the meteoric ionization trails at HF and VHF frequencies. The magnitude and sign of the doppler shift in the received echo frequency provides a measure of the radial wind velocity of the meteor trail with the neutral wind.

The meteor radar method for measuring atmospheric winds was first applied by Manning *et al.* [1950] at Stanford University. Since then, more than forty meteor radars had been constructed around the world for observations of atmospheric wind and waves [Tsuda, 1982]. In 1977, the Kyoto meteor radar was constructed by Radio Atmospheric Science Center, Kyoto University. It is located at Shigaraki, Shiga prefecture (34°51′N, 136°06′E), and operates at 31.57 MHz and 10-kW peak transmitted power with a duty factor of 0.084 with height resolution of 2 km. The meteor radar can continuously monitor the wind field at 80–110 km altitudes at a relatively low cost compared with the MST radar observations. The meteor radar is useful to observe the fundamental state of synoptic scale wind motions such as mean winds, planetary waves, and atmospheric tides.

Partial reflection radars At MF and HF frequencies, weak partial reflections are observed from the lower ionosphere both during day and at night.

The first wind measurements from this region using partial reflections (PR) are reported by Fraser [1965, 1968] at Christchurch (44°S, 173°E), who adapted the spaced antenna method which was originally applied to total reflection measurements of ionospheric drifts [Vincent, 1984b]. The spaced antenna method measures the temporal and spatial variations of the field pattern of the radar echoes with vertically beamed antennas. As the scattering irregularities move through the beam, they produce a moving diffraction pattern on the ground which is detected at three or more spaced receiving antennas. Wind velocities are obtained from the time delay between receiving antennas by cross-correlating the received signals [Briggs *et al.*, 1950]. It is shown by Briggs [1980] that the spaced antenna method and the Doppler method are principally use the same information by process it in different ways in order to obtain winds [Vincent, 1984b].

1.4 Observations in the middle atmosphere

As cited above, there are several ground-based techniques for the measurement of wind fields in the mesosphere [Gage and VanZandt, 1981]. In the last two decades, many attempts have been made to make comparisons among different techniques by using data collected with each technique, in order to understand the limitations and advantages of the different techniques. Meteorological rocket sounding were compared with partial reflection radar observations [Vincent *et al.*, 1973] and MST radars [Fukao *et al.*, 1979; Fukuyama, 1981; Smith and Fritts, 1984]. Meteor radar measurements were also compared with partial reflection measurements [Felgate *et al.*, 1975; Wright *et al.*, 1976; Stubbs, 1973]. They have shown good overall agreement between techniques which seem to provide equivalent wind fields in the mesosphere, although some discrepancies were found because of temporal and spatial differences between sites and the averaging or smoothing of wind fields because of the different time-height resolutions implicit in each technique [Tsuda *et al.*, 1985a].

Mean wind, long-period waves and atmospheric tides are well studied by using PR and meteor radars. This is because PR and meteor radars can provide wind fields continuously on a 24 hr basis in the height range of 80–105 km and 80–110 km, respectively [Vincent, 1984b; Tsuda, 1982]. By using these radars, mean winds are observed, for example, at Adelaide (35°S, 138°E) [Elford, 1976], Garchy (47°N, 3°E) and Kiruna (68°N, 20°E) [Massebeuf *et al.*, 1979], Atlanta (34°N, 84°W) [Dolas and Roper, 1981], Saskatoon (52°N, 107°W) [Manson *et al.*, 1981a], and Kyoto [Tsuda *et al.*, 1987a]. Seasonal variations of the prevailing winds have been analyzed by Manson *et al.* [1981a] and Tsuda *et al.* [1987a] at Saskatoon and Kyoto, respectively. An attempt

has been made to construct latitudinal cross-section of the mean zonal and meridional winds in the Australia–Newzealand sector in the period of 1980–1982 by using PR radar data [Vincent, 1984b]. These data are compared with CIRA 1972 model for zonal winds and Groves [1969] for meridional winds in order to produce a new model atmosphere [Manson *et al.*, 1985]. It is reported that the winter eastward wind velocity in the mesosphere centered at 30° is less than that shown in CIRA 1972. Also, asymmetry between northern and southern hemisphere was found: the mean zonal wind is, in both summer and winter, stronger in the southern hemisphere than in the northern hemisphere.

Observations of the atmospheric tides are also carried by using the meteor and PR radars cited above. These radars are the main facilities for the tidal observations in the mesosphere [Forbes, 1984]. The early results of tidal observations by using the Kyoto meteor radar are summarized by Aso *et al.* [1979, 1980]. Height variations of tidal components at both summer solstice and vernal equinox were reported by Tsuda *et al.* [1980]. Seasonal variations of tides were examined, for example, over Saskatoon by Manson *et al.* [1981b]. The radars at Kyoto and Adelaide are located at almost complete conjugate points with respect to the equator. Aso and Vincent [1982] utilized the data of both radars to observe the hemispheric differences in the tides in 1979. Recently, the comparison of the tides between Kyoto and Adelaide was examined by Vincent *et al.* [1987] again. They operated both radars in the years 1983–1985 and found distinct hemispheric asymmetries in the components of tides. The diurnal tide was usually much larger in amplitude at Adelaide, and the zonal and meridional wind components of the semidiurnal tides were about 6 hr out of phase and in-phase in all seasons, respectively [Vincent *et al.*, 1987].

Planetary waves are atmospheric waves with a period longer than 24 hr. It is usually assumed that these oscillations are caused by Rossby normal modes forced in the lower atmosphere. Although these modes of waves are usually evanescent, the waves can be locally propagating with westward winds and equatorward temperature gradient [Vincent, 1985]. A range of wave periods has been identified, but the waves with periods around sixteen, five and two days are most commonly reported [Vincent, 1985]. Among them, the 'quasi-2-day' wave has been extensively studied [e.g., Craig and Elford, 1981; Ito *et al.*, 1984]. It is generally accepted that the quasi-2-day wave is enhanced in summer months [Vincent, 1985]. By using the data of the Kyoto meteor radar in 1983–1985, Tsuda *et al.* [1987b] have reported the seasonal variation of the quasi-2-day wave. It is shown that the period of the wave was 52–55 hr in summer, and became 46–48 hr in autumn. This change seemed to be coincide with the seasonal variation of the mean zonal wind. Also, Tsuda *et al.* [1987b] compared the data with those at Adelaide, which implied the antisymmetry

of the quasi-2-day wave between northern and southern hemispheres.

Although the MST radars cannot receive any turbulence echoes in the nighttime, exceptions occur by utilizing the meteor echoes to determine winds [Avery *et al.*, 1983], or in the summertime high-latitude mesosphere, which is continuously sunlit [Gage and Balsley, 1984]. At Poker Flat MST radar (65°N, 147°W), in the summer under these conditions, mean winds and tides were observed [Carter and Balsley, 1982; Balsley and Riddle, 1984; Tetenbaum *et al.*, 1986]. Balsley and Riddle [1984] showed that the mean zonal wind agreed well with the other observations. Observations of the tides were also tried by using Jicamarca VHF radar by Countryman and Dolas [1982], Maekawa [1985] and Maekawa *et al.* [1986]. Planetary waves with periods of 2–8 days were observed over Jicamarca [Fukao *et al.*, 1980a] and Arecibo [Hirota *et al.*, 1983; Maekawa *et al.*, 1987a].

The good time-height resolution of the MST radar enables gravity wave observations in the middle atmosphere. Quasi-sinusoidal short period waves are often observed in the mesosphere [Woodman and Guillén, 1974; Rastogi and Bowhill, 1976; Miller *et al.*, 1978; Fukao *et al.*, 1979]. Fig. 1.8 shows radial wind fluctuations observed by the Urbana VHF radar [Miller *et al.*, 1978]. The antenna was tilted 1.5° off the zenith toward the southeast. Wave-like structures with periods of several minutes can be recognized, and were attributed to the short period gravity waves. Maekawa *et al.* [1987b] have reported that gravity waves with periods of 1–4 hr, on average, show downward phase propagation, which indicates an upward energy flux. Also, low-frequency gravity waves were observed by Balsley *et al.* [1983]. As shown in Fig. 1.9, zonal and meridional components showed gradual downward phase propagation, and they were nearly in phase quadrature [Balsley *et al.*, 1983; Fritts, 1984]. The vertical wavelength and period of the wave were approximately 14.5 km and 10 hr, respectively [Fritts, 1984].

A number of authors have computed the spectral energy density of atmospheric motions including gravity waves by using various kinds of radars: Frezal *et al.* [1981] by using meteor radars, Carter and Balsley [1982] by using the Poker Flat MST radar, and Fukao *et al.* [1985a] at Arecibo. Evidence of the wave dissipation is observed by using radars by obtaining the profile of the wave amplitude [Vincent and Stubbs, 1977; Manson *et al.*, 1979, 1981c; Balsley *et al.*, 1983]. From the decay of energy with height, Manson *et al.* [1981c] have reported that the typical vertical eddy diffusion coefficient is 200–600 m^2s^{-1}. Recently, it is reported that Doppler radars can measure the mean wind acceleration due to the gravity wave breaking [Vincent and Reid, 1983; Fritts and Vincent, 1987; Reid and Vincent, 1987]. The method uses two radar beams each offset from zenith to measure the atmospheric motions by the Doppler

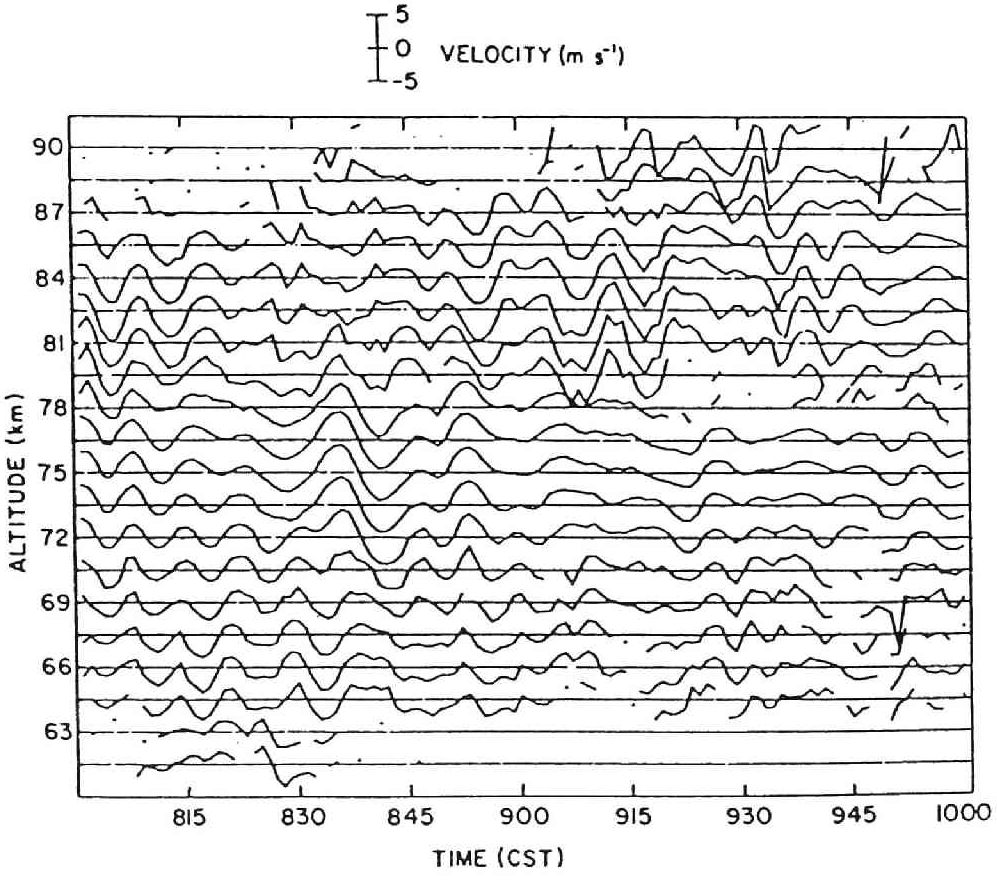

Figure 1.8: Mesospheric radial velocity versus time at different heights observed by the Urbana VHF radar on 11 April 1978. The antenna beam was tilted about 1.5° from zenith toward the southeast [Miller *et al.*, 1978].

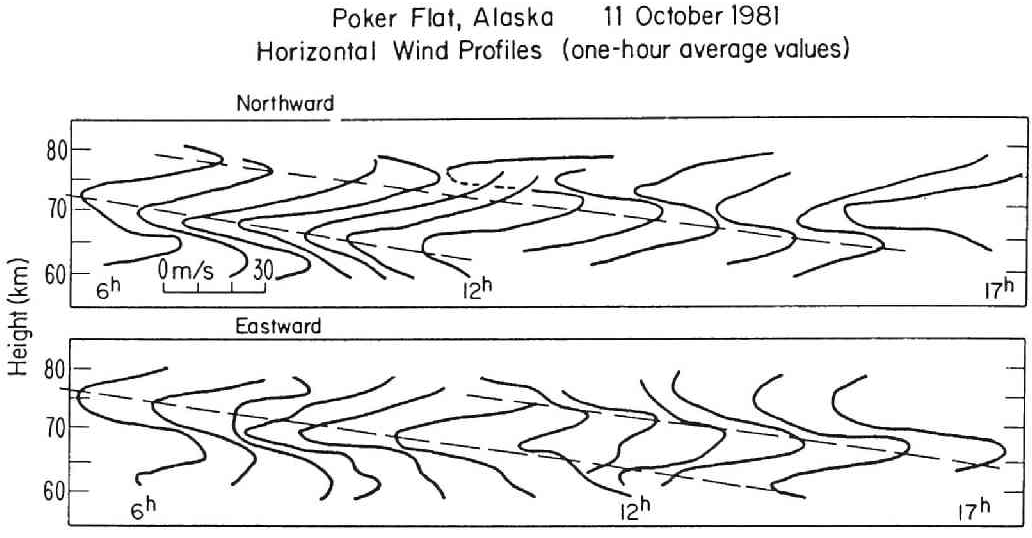

Figure 1.9: Time sequence of horizontal velocity profiles on orthogonal antenna systems for winter echoes at Poker Flat on 11 October 1981. Velocity scale is shown in lower left corner of upper panel. Dashed lines indicate approximate height of velocity extremes of the quasi-sinusoidal contours [Balsley *et al.*, 1983].

technique [Vincent and Reid, 1983]. Provided there is horizontal homogeneity, the momentum flux is proportional to the difference of the variances of the radial velocities measured in each beam.

1.5 Contents of the thesis

As shown in the previous section, The MST, meteor and PR radars are powerful tools to investigate the dynamics of the middle atmosphere. In 1982–1985, Middle Atmosphere Program (MAP) has been carried out in order to improve the knowledge on the middle atmosphere, and many kinds of facilities including these kinds of radars have been utilized for a variety of observations. In Japan, as one of the projects of MAP activities, the MU (Middle and Upper atmosphere) radar has been constructed in November 1984 by the Radio Atmospheric Science Center, Kyoto University. This type of MST radar is suitable for gravity wave observations because the radar can steer its main beam every transmitting pulse. Also, the Kyoto meteor radar, which has been operated since 1977, provides much data in the 80–110 km region. The purpose of this thesis is to investigate the behavior of gravity waves in the mesosphere through

observations with the MU radar and the Kyoto meteor radar. The contents of the thesis are as follows.

Chapter 2 shows the system configuration of the MU radar which is the main facility used in the present work. The chapter describes the antenna array system and the transmitter-receiver (TR) modules of the MU radar, which organize the active phased array system. The software system is also described here because one of the characteristics of the MU radar is that it is fully controlled under the supervision of computers.

In Chapter 3, a performance evaluation of the MU radar is presented. They consists of techniques to increase the signal-to-noise ratio and to reduce statistical fluctuations of echo power spectra. Methods of spectral parameter estimation are also shown, and errors expected in the estimated parameters are also discussed in this chapter. As a performance check of the MU radar with real data, wind velocities observed by using the MU radar are compared with that of the Kyoto meteor radar observations and a meteorological rocket sounding.

Chapter 4 is devoted to gravity wave observations by using the MU radar. Observations were carried out on February 8, 1985 and February 13 and 14, 1986. Gravity waves with large intrinsic periods (inertia gravity waves) are observed in the wind fields, and the dynamic stability of the atmosphere in the presence of gravity waves is discussed. A new technique to observe horizontal structures of the turbulence layers is also shown.

In Chapter 5, gravity wave observations with the Kyoto meteor radar are presented. The Kyoto meteor radar was operated continuously from May 1983 to April 1985. The chapter discusses power spectral density of wind velocities in the frequency range of 2–24 hr. It also shows a technique to analyze the apparent horizontal phase velocity of gravity waves and its statistical distribution.

The summary and conclusion of this thesis are presented in Chapter 6.

Chapter 2

The MU radar

The main facility used in this thesis is the MU (Middle and Upper atmosphere) radar located at Shigaraki, Shiga prefecture (34°51′N, 136°06′E). It has been completed in November 1984 after four years of construction. This chapter describes the system configuration of the MU radar by following the technical reviews of Fukao *et al.* [1985b, c]. For the Kyoto meteor radar, another radar used in this thesis, we do not discuss its hardware and software system because they are shown by Tsuda [1982] in detail.

Basic parameters of the MU radar are shown in Table 2.1 [Fukao *et al.*, 1985b]. The MU radar is a monostatic pulse Doppler radar operating at a frequency of 46.5 MHz. The maximum peak and average transmit power are 1 MW and 50 kW, respectively. The antenna is a circular array with an aperture of 8330 m^2. The one way half-power full width of the main beam is 3.6°. The shortest pulse with 1-μs width is available in the 1.65-MHz bandwidth reserved exclusively for the MU radar. The outline of the MU radar system and a few preliminary results obtained by using a partial system were presented by Kato *et al.* [1984]. The early results of the MU radar observations were reported by Fukao *et al.* [1986] and Kato *et al.* [1986].

2.1 System outline

The MU radar gains great advantages over other existing high power MST radars in steerability of its antenna main beam. This feature is achieved by an active phased array system [Fukao *et al.*, 1980b]. As shown in Fig. 2.1, in a conventional MST radar, the system provides with a passive antenna array, and a high-power transmitter feeds all array elements via an appropriate cascading feeding network. Each element of the antenna array of the MU radar, on the other hand, is provided with a low-power power amplifier, and all the

Parameter	Value
Location	Shigaraki, Shiga, Japan (34°51′N, 136°06′E)
Radar system	monostatic pulse radar; active phased array system
Operational frequency	46.5 MHz
Antenna	circular array of 475 crossed yagis
apperture	8330 m^2 (103 m in diameter)
beam width	3.6° (one way; half power full-width)
steerability	steering is completed in each IPP
beam directions	1657; 0°–30° off zenith angle
polarizations	linear and circular
Transmitter	475 solid state amplifiers (TR modules; each with output power of 2.4 kW peak and 120 W average)
peak power	1 MW (maximum)
average power	50 kW (maximum duty ratio is 5 %)
bandwidth	1.65 MHz (maximum)
IPP	400 μs to 65 ms (variable)
Receiver	
bandwidth	1.65 MHz (maximum)
dynamic range	70 dB
IF	5 MHz
A/D converter	12 bits × 8 channels
Pulse compression	binary phase coding up to 32 elements; Barker and complementary codes

Table 2.1: Basic Parameters of the MU radar [Fukao *et al.*, 1985b]

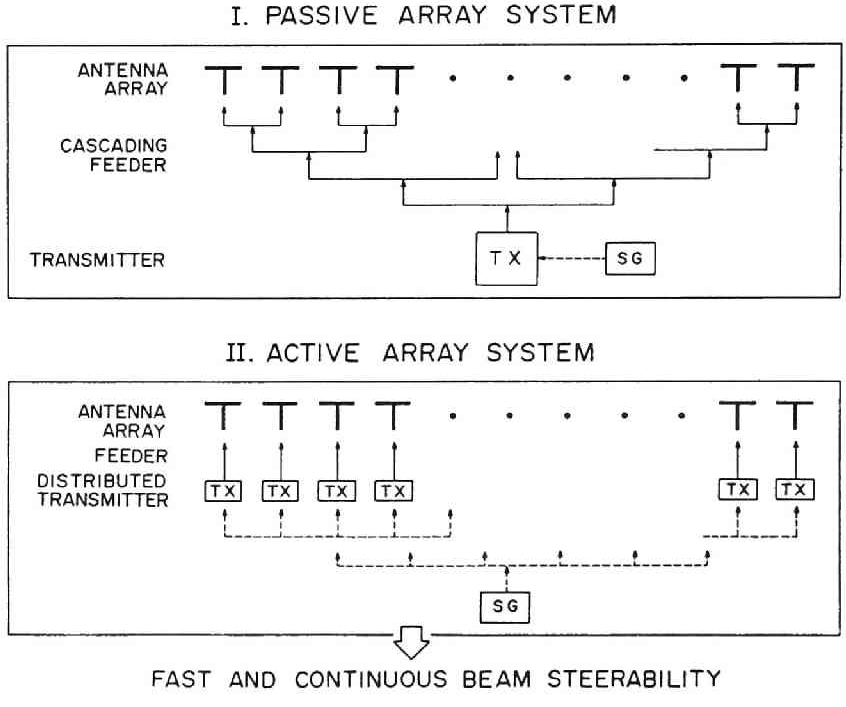

Figure 2.1: A schematic diagram of passive and active phased array systems [Fukao *et al.*, 1985b].

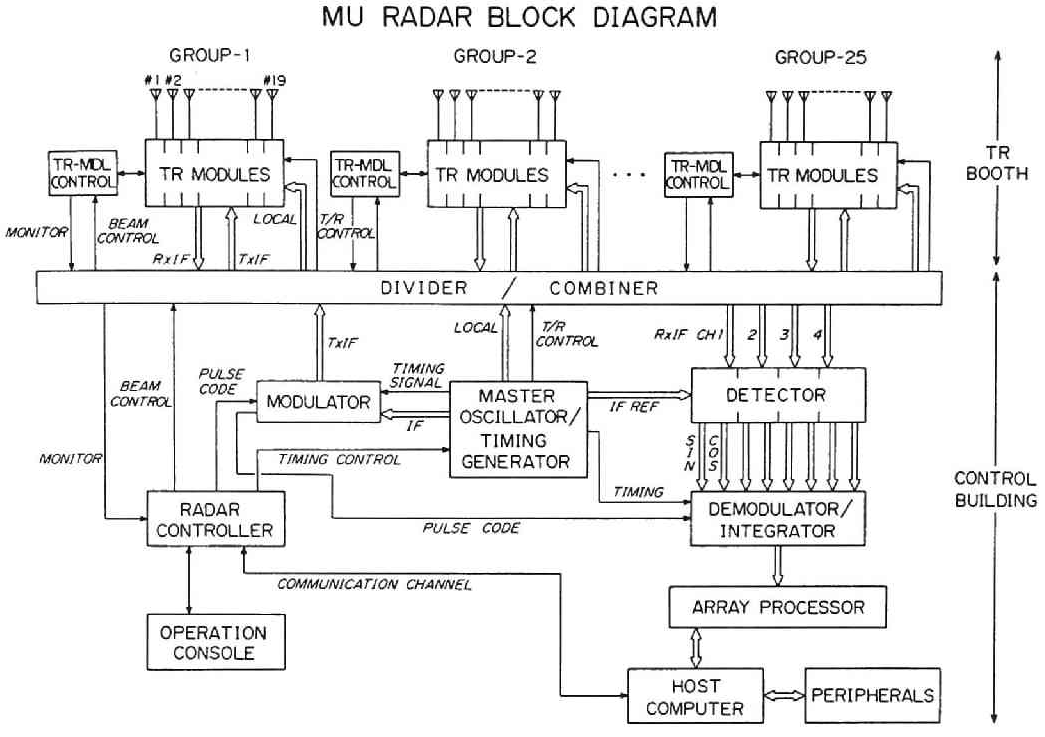

Figure 2.2: Block diagram of the MU radar. The TR modules and TR module controllers (TR-mdl control) are housed in TR booths built in the antenna field. Other system equipment is installed in the control building [Kato *et al.*, 1984].

amplifiers are driven by low-level pulses. This system configuration enables the radar very fast beam steering as well as various operation modes, which are obtained by the flexible system control with the aid of computers.

Figure 2.2 shows a block diagram of the whole MU radar system [Fukao *et al.*, 1985b]. The system is composed of 475 array elements and an identical number of transmitter-receiver (TR) modules. The TR modules are accommodated in six TR booths near the antenna array. The whole system can be divided into 25 groups (i.e. one group consists of 19 array elements and 19 TR modules). Each array element is driven by its own TR module. The main constituents of the TR module are a solid state transmitter, a receiver preamplifier, a T/R switch, and a digital phase shifter.

Both the upconvert and the downconvert to the intermediate frequency (IF) of 5 MHz are performed in the TR modules. The signal is transferred at the IF between the control building and the remote TR booths. This way

of frequency conversion prevents instabilities in the power amplifier due to possible leakage of output power into the input signal.

An antenna element consists of two orthogonally crossed three-subelement yagis pointed toward the zenith direction. Linear and circular polarizations of any sense are available with the aid of a polarization-selection switch in each TR module.

The overall operation of the MU radar is supervised by a programable radar controller linked with the 25 TR module controllers. The main constituent of the radar controller is a desktop computer HP9835A. Various timing signals necessary for real time system control are generated according to instructions from the radar controller. Sophisticated software in the radar controller makes a variety of flexible operations possible. For instance, it is possible to steer the antenna beam in each inter-pulse period (IPP), i.e. up to 2500 times every second, virtually to any direction within 30° off the zenith. Moreover, it is possible to excite only a portion of the antenna array and receive the echo by other portions, and/or to steer multibeams in different directions.

A large amount of data (up to 1024 samples) can be processed in real time. A minicomputer (VAX-11/750) and an array processor (MAP-300) with a 2-Mbyte random access memory (RAM) are installed for this purpose. Before being processed by the computer, the echo signals are decoded for pulse compression, and then coherently integrated in order to reduce the amount of data by using the special purpose hardware.

High reliability of the system is expected to be achieved by means of a network of the radar controller and 25 TR module controllers which monitor the TR modules during the operation.

2.2 Hardware configuration

2.2.1 Antenna array

The antenna array system of the MU radar is designed subject to the following restrictions:

1. The antenna aperture is to be less than about 100 m in diameter at radar site.

2. The number of antenna elements/TR modules necessary to attain the total peak power of 1 MW is approximately 500, because the output power of each TR module is expected to be about 2 kW.

3. Neither spatial nor electrical tapering is incorporated.

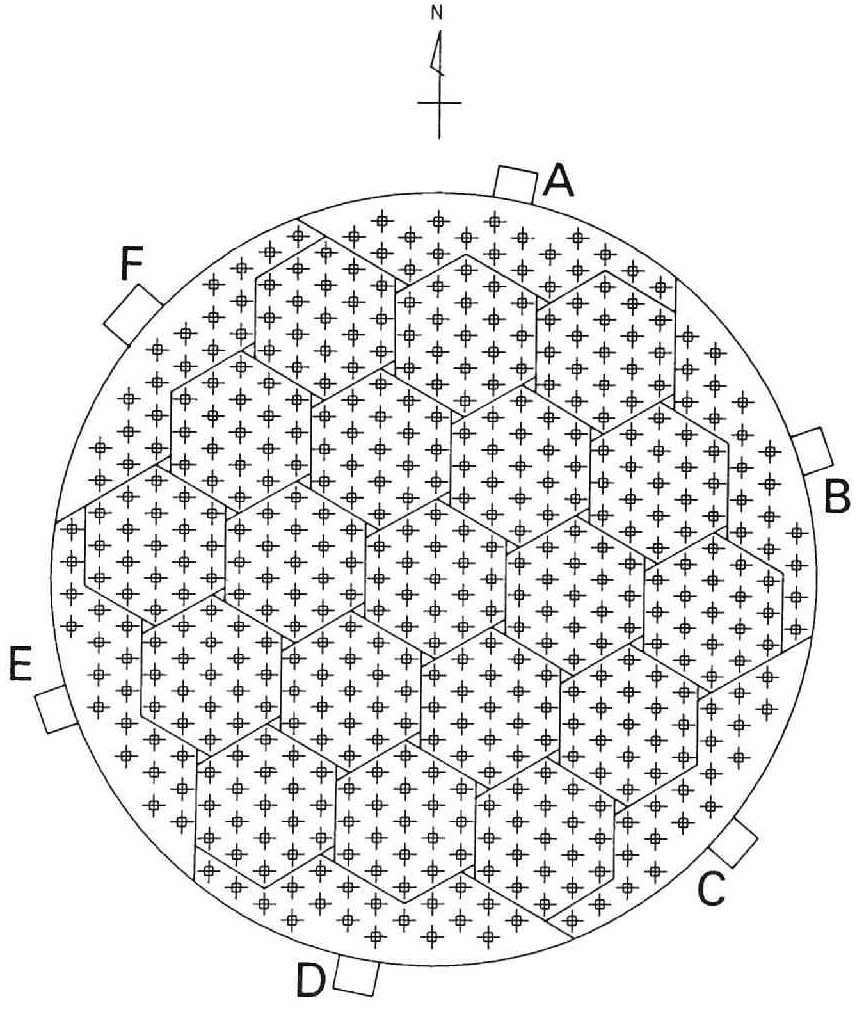

Figure 2.3: MU radar antenna array. Each cross represents a crossed three-subelement yagi. The small square at each array element position is a concrete block for the element foundation. The six boxes outside the antenna array, indicated as A–F, represent the booths which accommodate the TR modules. All booths except F accommodate TR modules for three hexagonal subarrays and one peripheral subarray. The TR modules for the central hexagon are housed in booth F [Fukao *et al.*, 1985b].

The array configuration is designed to be nearly circular in order to obtain almost symmetrical sidelobes with respect to azimuth angle. The diameter of the array is 103 m, and the antenna apperture is 8330 m^2. As for arranging the array elements, a triangular grid is used, since it generally allows a wider range of antenna beam steering than a rectangular grid with the same element density [Sato, 1981].

The actually constructed antenna array is shown in Fig. 2.3, where 475 array elements indicated by crosses are periodically arranged on the grids of equilateral triangles, with one of their sides pointed to the geographical meridian. The two dipoles are mounted in the east-west (EW) and north-south (NS) directions, respectively. The element spacing is 0.7λ (λ is wavelength), for which no grating lobe is formed at beam positions within 40° away from the zenith.

The antenna array can be divided into 25 groups, each consisting of 19 array elements connected to the same number of TR modules. Nineteen of the groups are identical hexagonal subarrays composing the main part of the antenna array, while the remaining six are subarrays distributed around the periphery making the array nearly circular. Each group can be driven separately, and even individual array elements can be driven independently. However, the maximum number of separate beams is limited to four due to the number of available detector channels [Fukao *et al.*, 1985c]. The peak radiation power of 1 MW is attained when all groups are coherently activated.

The elements of the array have been designed to be matched well to the feed line impedance of 50 Ω in the required bandwidth of 1.65 MHz. They are also required to have a high front-back ratio in order to avoid change of array pattern due to variation in the reflectivity of the ground plane [Sato, 1981]. Figure 2.4 illustrates the dimensions of the optimized three-subelement yagi. The radiator and reflector/director are made of aluminum and steel pipe, respectively. At a point frequency of 46.5 MHz, the calculated element gain of the three-subelement yagi in the infinite array coincides with the theoretical limit of 7.24 dB in the zenith direction. The active impedance is very close to 50 Ω, proving excellent matching to the feed line. Frequency dependence of the element properties is fairly small, and VSWR is kept below 1.25 at the zenith direction within the required bandwidth.

Figure 2.5 shows a computed array pattern for three different beam directions using optimized three-subelement yagis as array elements. Only the NS-aligned elements are excited, and the beam is changed in the meridional plane. The beam width of the main lobe is approximately 3.6°, corresponding to a gain of 34 dB. The first side lobe is suppressed by more than 18 dB with respect to the main lobe. The spillover radiation at elevation angles below

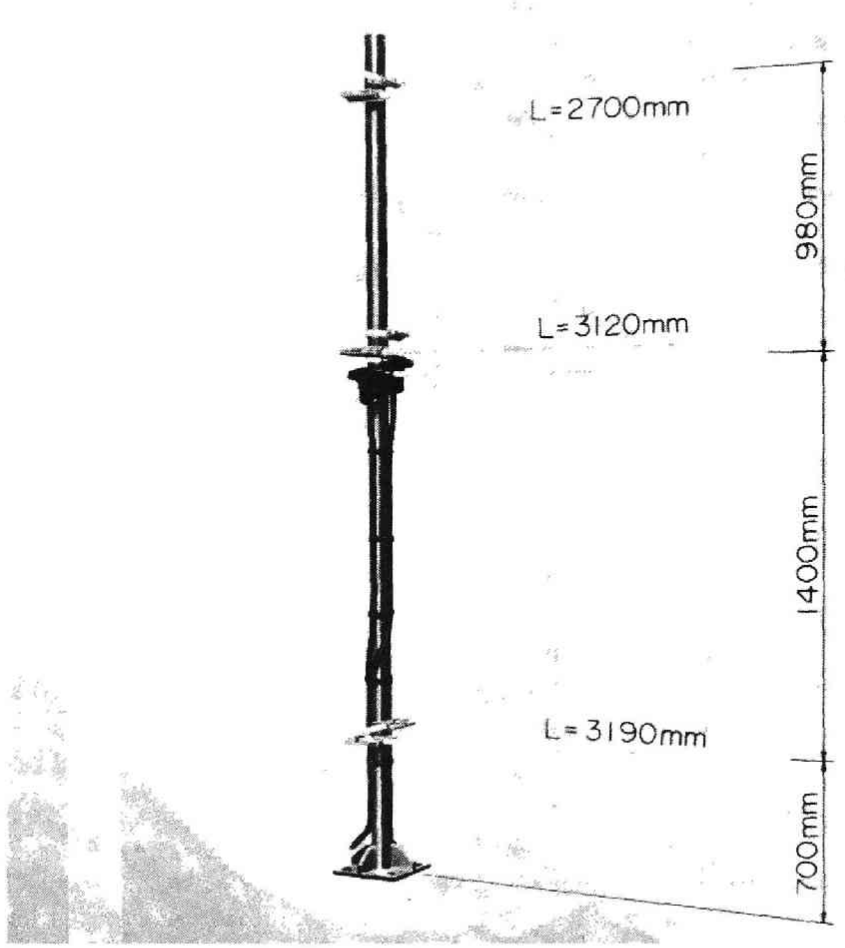

Figure 2.4: Optimized crossed three-subelement yagi [Fukao *et al.*, 1985b].

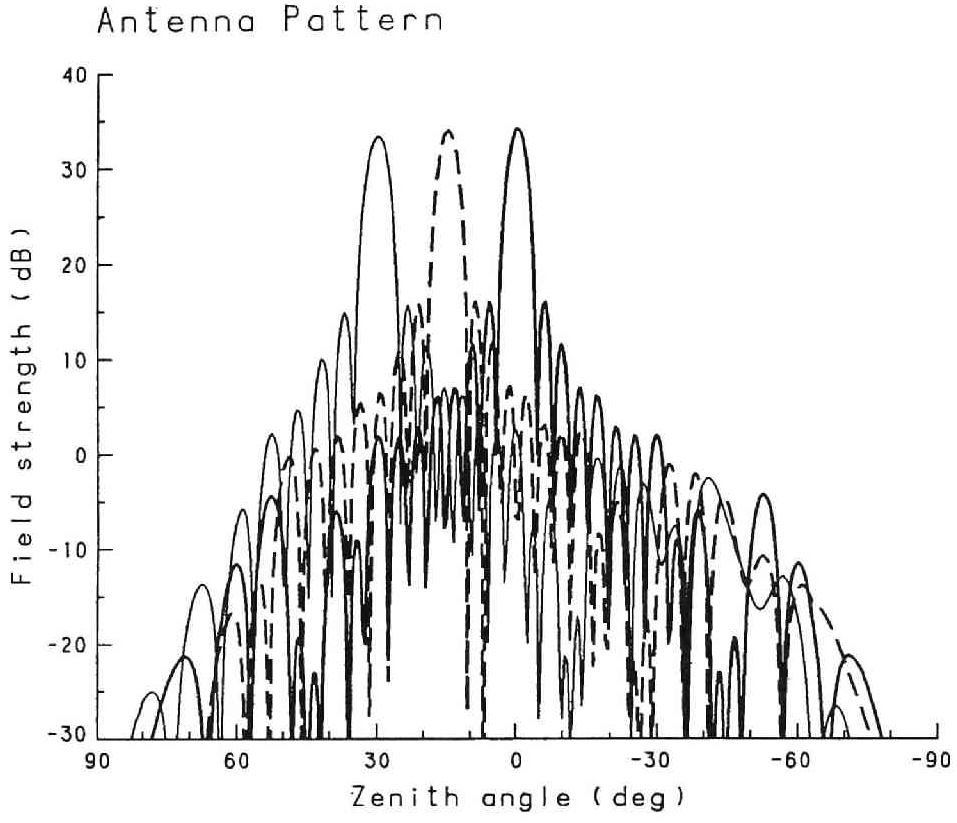

Figure 2.5: Computed radiation patterns of the MU radar antenna array employing optimized three-subelement crossed yagis as array elements. Only the NS-aligned elements are excited. The field strength is normalized to the radiation field of an isotropic antenna matched to feed line impedance. The antenna beam is tilted by 0° (zenith), 15° and 30° from the zenith along the NS direction [Fukao *et al.*, 1985b].

20° is reduced by more than 40 dB even when the antenna beam is tilted 30° from the zenith. It is found that in the azimuth directions the sidelobes are distributed almost symmetrically and uniformly without any outstanding peak in any particular direction.

2.2.2 Transmitter-receiver module and other equipment

As described in 2.1, both upconvert and downconvert are conducted in the remote booths, so that the IF (5 MHz) and local signals (LO, 41.5 MHz) are transferred between the booths and the control building. The signals are sent to each booth through coaxial cables of equal length. Figure 2.6 is a block diagram of one group of TR modules. Upon arrival at the booth, the IF and LO signals are divided into four (or five) groups by the TX IF divider and local divider, respectively, and distributed to the 19 TR modules in each of the groups. The received IF signals from the 19 TR modules, On the other hand, are combined into one by the RX IF combiner and sent directly to the control building. The timing signals for T/R switching and initial set pulse (ISPL) are split in the same way.

The main constituents of the TR module are a mixer (MIX) unit and a power amplifier (PA) unit, whose block diagrams are shown in Figs. 2.7 and 2.8, respectively. The frequency conversion is performed in the MIX unit. The 41.5 MHz local signal fed to the MIX unit passes through a digital phase shifter for beam steering and TX/RX phase correction. The MIX unit also contains a buffer amplifier, a gate for transmission and preamplifier for reception.

The PA unit amplifies the radio frequency (RF, 46.5 MHz) signal supplied from the MIX unit up to 63.7 dBm (2350 W), and feeds it to an array element. An exciter consisting of a three-stage amplifier operates in A-class with a gain of 39.5 dB. The final power amplifier stage is composed of four push-pull circuits operating in parallel mode with a gain of 12 dB.

A TR switch consists of a combination of two 3-dB hybrids and high-power PIN diodes [Czechowsky *et al.*, 1984]. Three additional diode switches are inserted in the RX channel in order to obtain a total isolation of 100 dB between TX and RX signals. Switching requires 10 μs, limiting the time for TX and sampling start. A band pass filter is inserted after the TR switch to prevent transmission of unnecessary harmonics. The second and third harmonics are reduced by 85 dB and more than 90 dB, respectively, in comparison with the fundamental frequency.

Phase and intensity of the TX signal are monitored by TR module controller via a directional coupler. During observation, the radar controller polls the TR module controller for monitor data. Also, output VSWR is detected by the

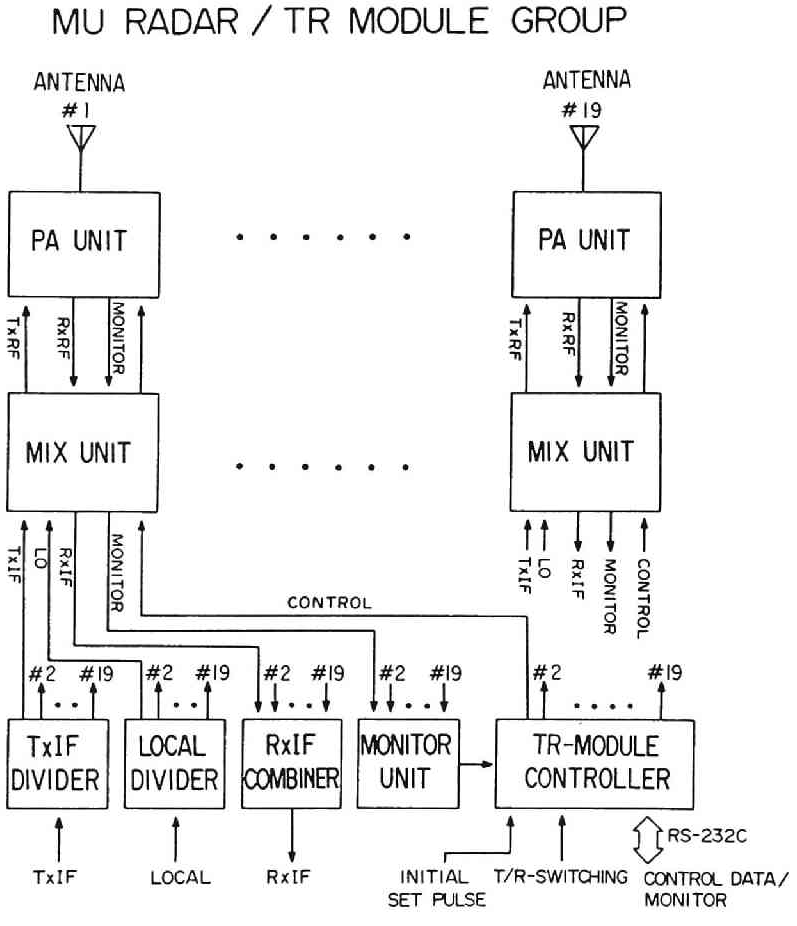

Figure 2.6: Block diagram of one group of TR modules. Nineteen array elements and the same number of TR modules constitute one group, with common equipment consisting of TX IF divider, local divider, RX IF combiner, monitor unit and TR module controller [Fukao *et al.*, 1985b].

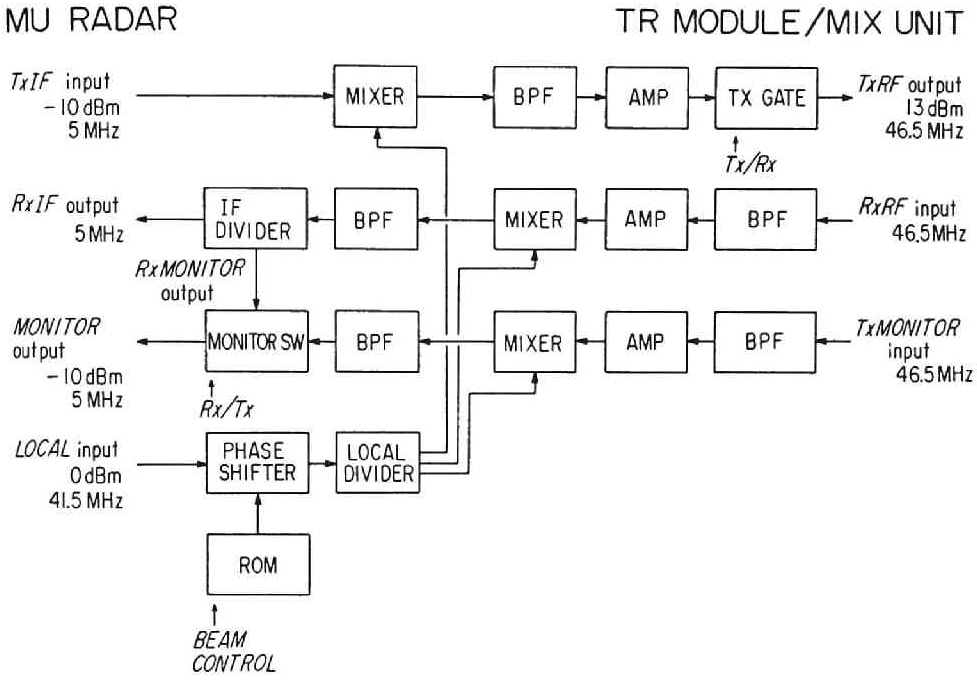

Figure 2.7: Block diagram of the mixer (MIX) unit in a TR module [Fukao *et al.*, 1985b].

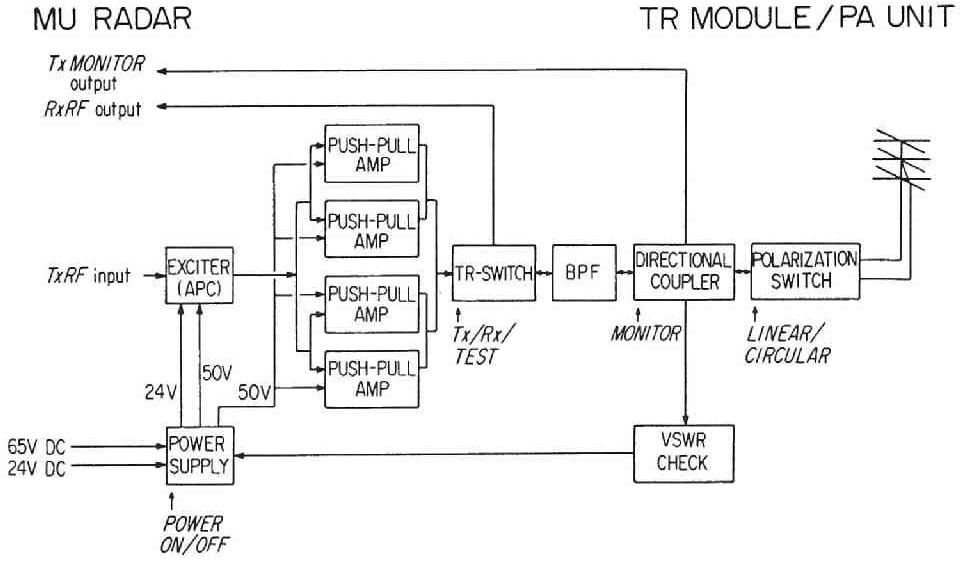

Figure 2.8: Block diagram of the power amplifier (PA) unit in a TR module [Fukao *et al.*, 1985b].

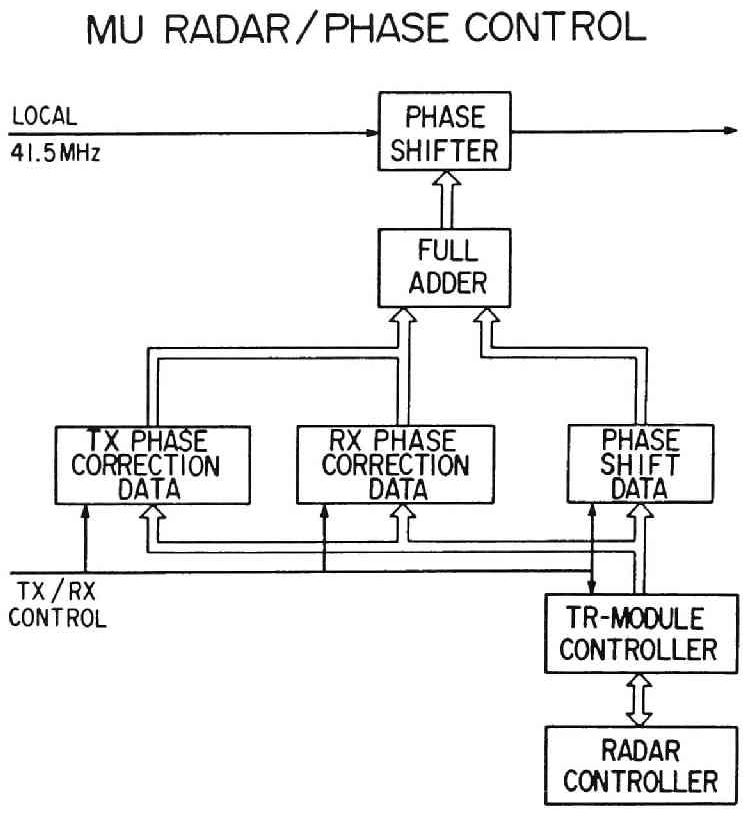

Figure 2.9: The basic phase control concept of the MU radar. Phase shift data is used for beam steering, while TX/RX phase correction data are required to compensate for phase differences caused by individual differences in the power amplifiers, varying cable lengths, etc [Fukao *et al.*, 1985b].

hardware in order to protect high-power transistors. The polarization selection switch is comprised of two relays and a 3-dB hybrid, which gives two linear and right- and left-hand circular polarizations.

The RF outputs of the TR modules are sent to array elements through coaxial cables. However, cables length varies, the longest being 77 m and the shortest 11 m. The delay time differs by 250 ns between the longest and the shortest cables. This difference is compensated by inserting delay lines into both TX IF and RX IF channels so that the delay time is equal to that of the longest cable. The phase differences among array elements which is caused primarily by individual differences among TR modules is equalized by adding proper phase rotation to the TX and RX channels. The basic concept for

the phase control is shown in Fig. 2.9. The phase correction data for both TX and RX channels are sent from the radar controller and stored in the one-word RAM in the TR module controller prior to observations. By using this correction data, all antenna elements are fed in an equal phase, and the antenna beam is directed toward the zenith. All phase shift data required for beam steering are stored in the read-only memory (ROM) installed in the MIX unit of each TR module. The data are read out according to instructions from the TR module controller, and added alternately either to the TX or RX phase correction data by an full adder.

The phase shifter is essentially the same type as employed for the SOUSY radar [Schmidt *et al.*, 1979; Czechowsky *et al.*, 1984], but it is composed of eight coaxial cables with length of $\lambda/2^n$ ($n = 1, 2, \ldots, 8$). The phase can be changed in steps of $\lambda/256$ (approximately 1.4°). This causes the beam to be steered in the zenith direction in steps of 1° up to 16° from the zenith, in 2° steps in 16°–30° zenith angle, and in 5° steps in the azimuth direction. The total number of the available beam direction is 1657.

As shown in Fig. 2.10, various analog signals required for transmission (TX) and reception (RX) and timing signals for system control are generated by a combination of a Rubidium-vapor master oscillator, a frequency synthesizer and a timing signal generator, which are installed in the control building. The IF signal (5 MHz) for transmission and detection, and the LO signal (41.5 MHz) are synthesized from the reference signals of 1 and 5 MHz. The frequency synthesizer also generates the reference digital clock of 4 MHz. The 4-MHz clock is utilized in the timing signal generator where various timing signals required for real time system control are generated according to instructions from the radar controller.

Some details of the control data are as follows. The MU radar starts/stops its operation by means of TX start/stop control data. The number of subpulses is indicated when pulse compression is conducted. In the case that the transmission of multiple pulses [Farley, 1972] (up to seven pulses) is incorporated, a TX pulse sequence and the total length of this sequence are set. The RX gate is opened at a preset time to begin signal sampling. Sampling ends when the desired number of samples have been taken. The coherent-integration-end signal is generated when transmission and reception are repeated the number of times needed for coherent integration. Sampling start timing can be changed by a half or quarter of the sampling interval in order to stagger range gates within a scattering volume. Other control data and timing signals are referred to in Fig. 2.10.

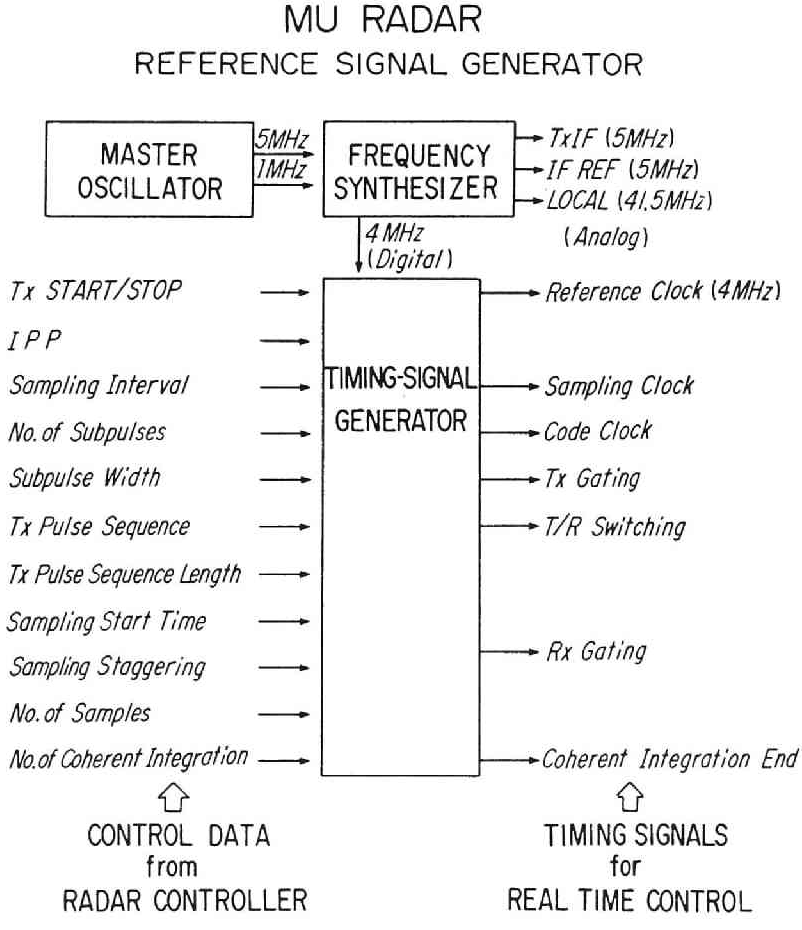

Figure 2.10: Block diagram of the reference signal generator. Control data are set by the radar controller. Timing signals are sent to various system hardware for real time control [Fukao *et al.*, 1985c].

2.3 Software configuration

2.3.1 Radar controller

Because the MU radar system is more flexible than other existing MST radars, it can realize new observation techniques which is difficult with other facilities. In order to fully control the MU radar system without losing its flexibility, a desktop computer (HP9835A) is utilized for the system control, which is called the radar controller. A program on this computer is named the "observation control software". The peripheral equipments of the radar controller are floppy disk driver, printer and several input/output (I/O) interfaces. Programs and data for the radar control are read out from the floppy disk drive, and the printer is used to list parameters of the MU radar observations.

The radar controller has two types of I/O interface. Parallel I/O (PIO) interface is used by the radar controller to communicate with the in-house equipment installed in the control building, i.e. master oscillator/timing generator, modulator, demodulator/integrator, divider/combiner and detector. Serial I/O (SIO) connects the radar controller to the TR module controllers in six TR booths, host computer and operation console. The transfer speed is 1200 baud.

The control and communication items of the radar controller are shown in Fig. 2.11. To the in-house equipment, the controller sends signals which control the transmission, reception and signal processing for the received data. To the TR module controller, it sends the instruction for the antenna usage, and, during the operation, monitors the diagnostic data of the TR booths and TR modules. For the data acquisition and processing, the radar controller first instructs the host computer to choose the appropreate data taking program, and then transfers all the observation parameters. Because start/stop of observations are controlled by the clock installed in the host computer, it shows time to start/stop the observation, and/or number of data to be obtained in the observation. The operating console also sets the observation parameters, and sends them to the radar controller. During the operation of the radar, the operating console displays the observation parameters and monitors received signal. The usage of the antenna array and observation height range are shown graphically on the display board.

The flexibility and the wide range of choise of the system parameters concerned with the MU radar hardware complicate to control the system. The performance of the observation control software is an important factor for the performance of the MU radar itself. When we use the MU radar for observations, we set up a file which contains various observation parameters with the

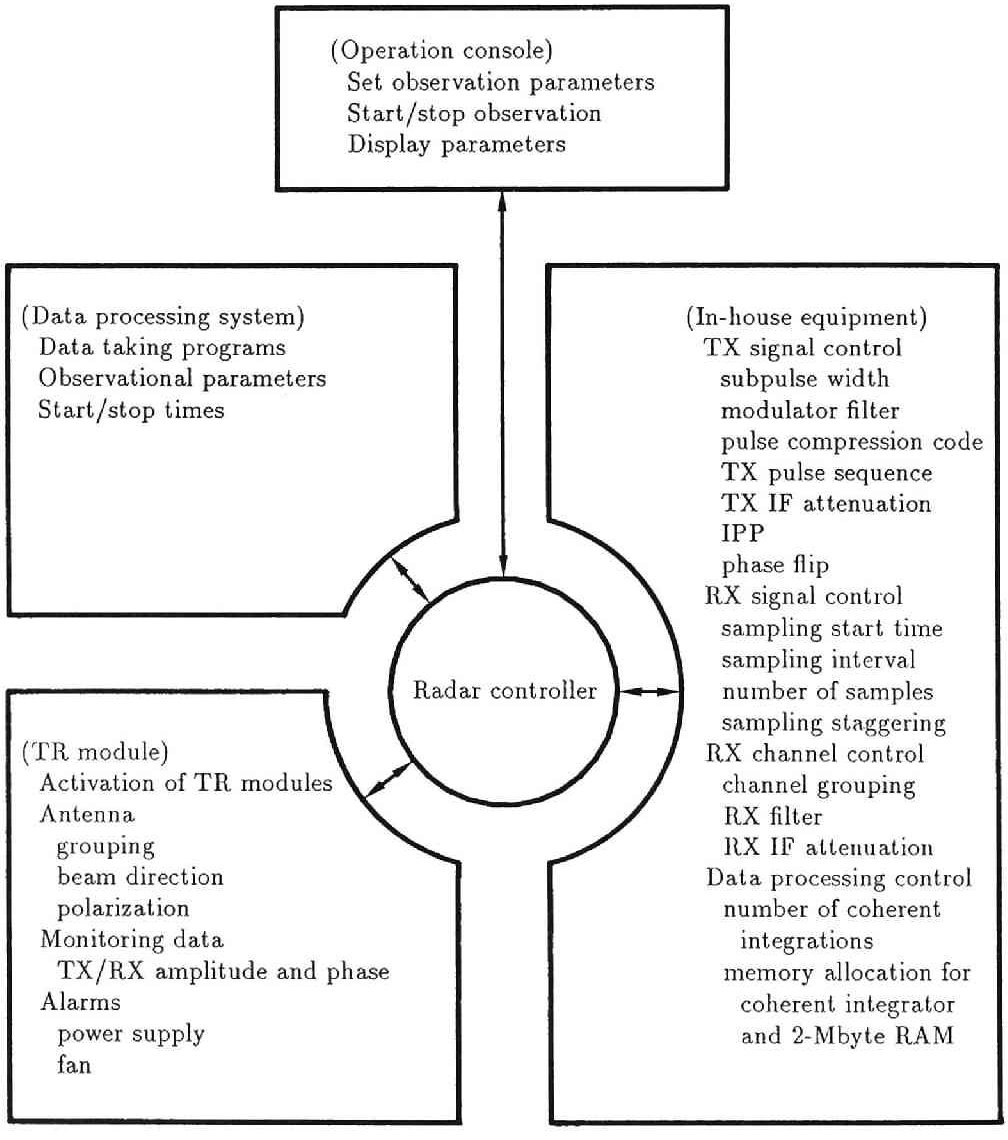

Figure 2.11: Control and communication items of the radar controller [Fukao *et al.*, 1985c].

aid of the radar controller. The radar controller operates the MU radar system according to the parameters stored in the file. The control program should be easy for users to set observation methods and to operate the radar. We need the following functions,

1. The program should manage the files on the floppy disk which stores observation parameters. This function is needed to utilize existing parameters for new observations. A function to schedule observations is also needed because this makes it possible to operate the MU radar automatically for long time according to the schedule.

2. A function to test the MU radar system is needed. When we operate the radar for tests, it is often required to change parameters. Also, the program should be able to operate all functions of the radar including special modes for the tests, e.g., continuous transmission for the antenna pattern monitoring.

3. Because not all of users are familiar with the radar hardware, the program for the parameter setting and the operation must be easy to use, and should not require any further knowledge of the MU radar system. We should use physical values to specify parameters, e.g., observation altitude range [km] instead of sample start time [μs] and number of samples.

4. By using the operating console, users can operate the radar even if they are not accustomed to using computers. This function requires a special program on the radar controller because there are restrictions on the operations by using the operating console.

In order to satisfy these requirements, the observation control software is designed to consist of three parts, which are a program for the system test (TEST), programs for universal observation control (SET, INDEX, OPERATE) and a program to operate the radar by using the operating console (CONSOLE).

The program "TEST" provides users with all functions which are needed to test the system of the MU radar. The characteristic of TEST is that the commands to operate the system are divided into the smallest unit, e.g., parameter setting, parameter transfer and TX start/stop.

The "CONSOLE" is a program to operate the MU radar from the operation console. When we use this program, the MU radar can be operated only in six standard observation modes with changing a portion of parameters. However,

the operation is the simplest, and users can start observations by just pushing several switches on the operation console.

The program for universal observation control is divided into three parts. This program can be used for almost all the observations with the MU radar. The part to set observation parameters is called "SET". Users can input and change observation parameters in the physical values instead of the system numbers through an interactive editor. By using the program named "INDEX", parameter files are managed and users can obtain a list of observation parameters. The operation of the radar is managed by a program "OPERATE". The parameter file is read out from the floppy disk and utilized for the next observation. This program also manages a schedule of observations.

2.3.2 Data acquisition

As shown in Fig. 2.12, the data processing sub-system is a part of the radar system which processes and records the data received by the MU radar. The main constituent of this part is the host computer VAX-11/750 (hereafter referred to as VAX). The peripheral equipments of VAX are magnetic disk units, two magnetic tape drives and color graphic displays. In order to accelerate the data processing speed, an array processor MAP-300 (MAP) is utilized. The calculation of fast Fourier transformation (FFT) or autocorrelation function is performed by MAP which is equipped with 2-Mbyte external RAM. The 2-Mbyte RAM is used as both buffer for input data from the demodulator/integrator, and for incoherent integration of power spectra or autocorrelation functions.

The data flow of the data processing sub-system is shown by arrows in Fig. 2.12. The detected signals are integrated by the integrator and written in the input buffer of the 2-Mbyte RAM. When the input buffer is filled with the data, MAP reads the data and calculates the power spectra by FFT. The results are added with the former power spectra which are stored in the incoherent integration buffer of the 2-Mbyte RAM, and stored again into the buffer. This summation of power spectra or autocorrelation function is called "incoherent integration". After finishing a preset number of incoherent integrations, the data are transferred to VAX through MAP and stored on the magnetic disk, and are also recorded on the magnetic tape. The data file on the magnetic disk is called the "ring buffer" which can contain the last ten observation records. The data in the ring buffer can be shown on the graphic display during the observations by an interactive quicklook program.

The software for the real time signal processing consists of three programs as follows,

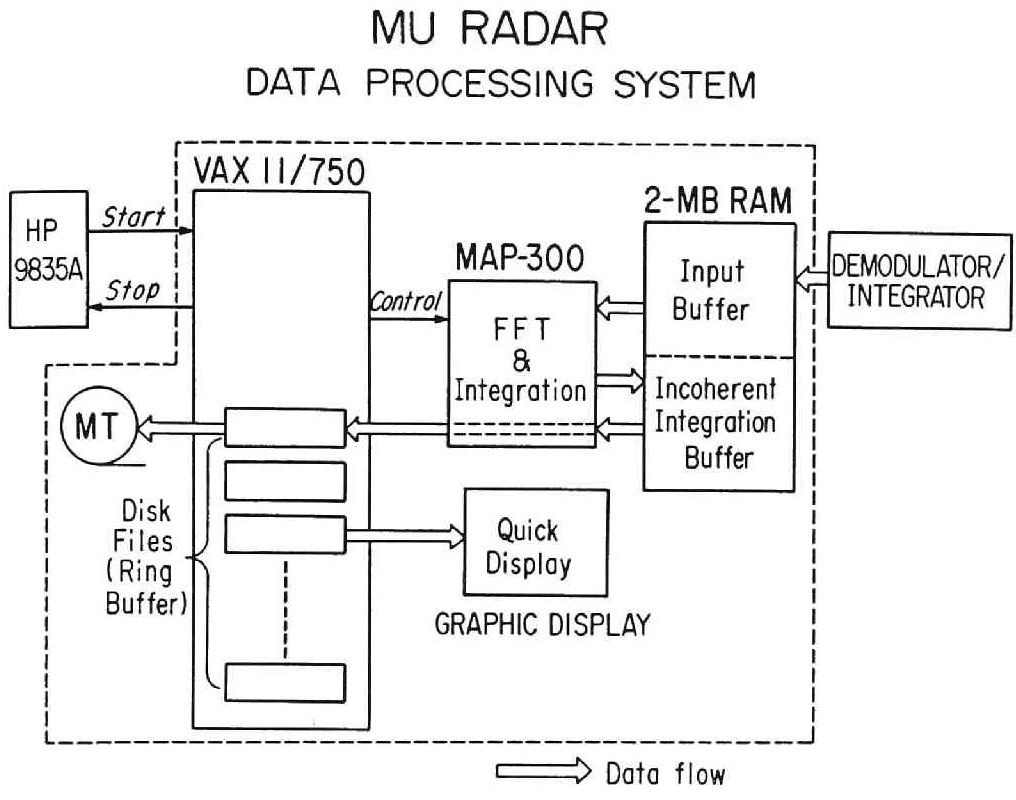

Figure 2.12: Principal constituents for on-line data processing (inside the dotted line). Data flow is indicated by thick arrows [Fukao *et al.*, 1985c].

- Control program
- Data taking program
- Quicklook program

The data taking program controls MAP and processes the data. Because programs for MAP are different for different observational techniques, the data taking program is specialized for each technique. The control program manages several data taking programs, and generates a subprocess to execute the data taking program which is specified by the radar controller. The control program also monitors behavior of the data taking program and MAP, and manages two magnetic tape drives for the data recording. The quicklook is a program to read the processed data from the ring buffer and show them on the graphic display in order to monitor the data taken by the observations.

When observations are started, the radar controller sends name of the data taking program to the control program on VAX. The control program starts the specified data taking program, then the data taking program receives the observation parameters from the radar controller. These parameters consist of SIO and PIO data sent to the hardware, and parameters required for data processing on VAX. The data taking program initiates MAP, and defines the calculations performed on MAP as a 'function list'. The function list is a series of operations to be performed by a single command from the host computer. It largely reduces the time loss due to handshakes between VAX and MAP during these operations. After starting the calculation of MAP, the data taking program sends data to start observation. When MAP is invoked, it send the "READY" signal to the hardware, which starts the transmission. MAP is interrupted by the 2-Mbyte RAM when it is filled with the received data. MAP reads the data from the input buffer, performs the pre-defined calculations, and write the results into the buffer for incoherent integrations. The transmission is discontinued during the calculation of MAP, but is started again by means of the READY signal sent by MAP. When number of incoherent integration is satisfied, the data taking program reads the data from the 2-Mbyte RAM through MAP, transfers them to the ring buffer on the magnetic disk, and continues the observation by restarting the calculation of MAP. The control program reads the data from the ring buffer, and records them on the magnetic tape immediately after the data taking program writes new data on the ring buffer. The control program also monitors MAP, and, in case of some errors, stops the observation, and sends caution to the radar controller. The radar controller can also interrupt the data taking program to stop the observation. The quicklook program is executed asynchronously, and users can interactively operate the quicklook program to read the data from the ring buffer, and obtain various kinds of graphic outputs.

Chapter 3

Performance evaluation of the MU radar

This chapter describes the basic data processing techniques used with the MST radar observation and the performance of the MU radar in the middle atmospheric observations. When we observe wind velocities in the middle atmosphere, two integration techniques, "coherent" and "incoherent" integrations, are adapted in order to increase signal-to-noise ratio (SNR) and/or to reduce statistical fluctuation in the echo power spectra, respectively. There are several techniques to estimate mean Doppler shift in the echo power spectra. These techniques are explained first, and then the estimation error of the spectral parameters are shown. This chapter also contains comparison of wind velocities in the mesosphere observed by the MU radar and the Kyoto meteor radar. The result of a meteorological rocket sounding is also compared with the MU radar results.

3.1 Observational techniques

3.1.1 Data processing

As shown in Fig. 3.1, with a monostatic pulse radar, the range r from the radar to the scattering volume is calculated by means of time delay τ between transmitted and received pulses as follows:

$$r = \frac{1}{2}c\tau \tag{3.1}$$

where c is speed of light. And, range resolution Δr is given by

$$\Delta r = \frac{1}{2}c\Delta\tau \tag{3.2}$$

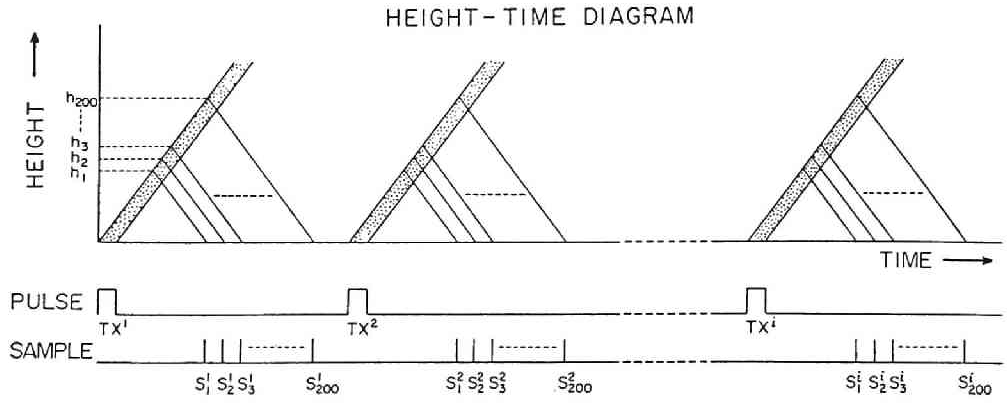

Figure 3.1: Height-time diagram of transmitted pulses of a monostatic pulse radar. The range between the radar and the scattering volume is measured by the time lag until the transmitted pulse returns.

where $\Delta\tau$ is transmitted pulse length. It is shown that the pulse length should be small in order to obtain better range resolution. Considering the radar equation Eq. (1.51), however, short transmitted pulse decreases the echo power obtained by the radar.

A pulse compression technique is used to increase the range resolution of radars while using a long transmitted pulse [e.g., Skolnik, 1980]. This is a technique to modulate the transmitted pulse by flipping the phase by 180° according to a code. The demodulation is made by correlating the time series of the received signal with the reference code. Figure 3.2 shows an example of the complementary code which is usually used in MST observations in the middle atmosphere. These codes were first introduced by Woodman [1980] to the lower stratospheric observations at Arecibo. The 32-element complementary codes are composed of a pair of binary codes each with a length of 32 μs. Because autocorrelation functions of the code 1 and code 2 have sidelobes of the same amplitude with the opposite sign, we can obtain an autocorrelation function without any sidelobes by adding the two autocorrelation functions.

In the middle atmosphere, the correlation time of the VHF and UHF return signals from turbulence ranges from 0.1 to 10 s. This is very long compared with the inter-pulse period (IPP) of the radar of approximately 1 ms. Thus, many samples, which are outputs of the quadrature detector, are accumulated in order to reduce the number of data sampled. This procedure is called "coherent integration" because data are integrated so as not to lose its phase information. By executing N coherent integrations, the signal and noise power increases by N^2 and only by N times, respectively, and, so we increase the SNR

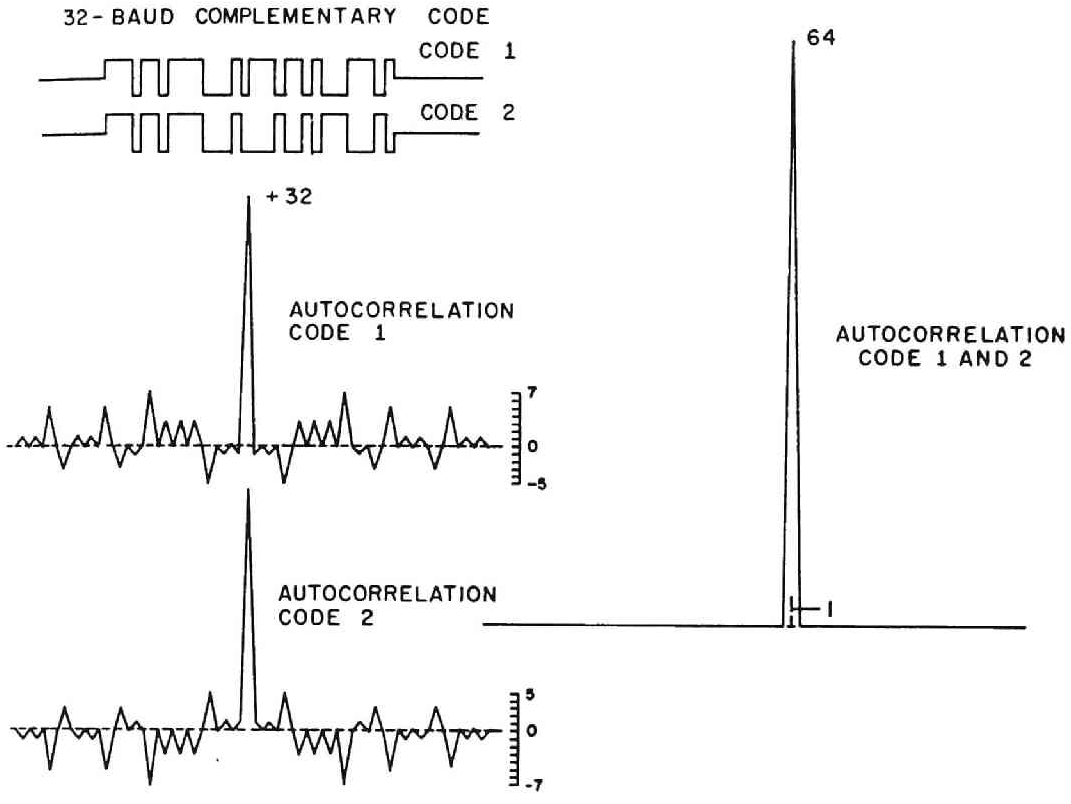

Figure 3.2: The 32-element complementary code patterns and the respective autocorrelation functions. The combined autocorrelation function is presented on the right [Woodman, 1980].

by N times.

In order to detect the Doppler shift caused by the motion of the scattering volume, we need to obtain the frequency spectral information of the return signal. The most popular way is to calculate the power spectrum of the radar returns by using the fast Fourier transformation (FFT) algorithm. The power spectrum shows a statistical fluctuation due to random nature of turbulence. The output of the receiver, which is a time series of data, is a random process with a Gaussian distribution. Because the Fourier transform is a linear transformation and power spectral density is a squared sum of both real and imaginary parts of the spectral component, the power spectral density shows a statistical fluctuation with a χ^2-distribution [e.g., Bendat and Piersol, 1971]. Thus, the standard deviation of the power spectrum is proportional to the spectral density itself. The amplitude of the statistical fluctuation in

the spectra can be reduced by averaging successive power spectra, which is called "incoherent integration". When we execute N incoherent integrations, the standard deviation of the power spectrum is equal to $S(f)/\sqrt{N}$, where $S(f)$ is the power spectral density at frequency f. Thus, for example, when we do not apply any incoherent integration, the statistical fluctuations of the power spectral estimates are 100%.

3.1.2 Spectral parameter estimation

In MST radar observations there are several techniques to estimate parameters such as echo power, radial wind velocity and spectral width. For the return signal of MST radars we can assume that a power spectrum of the radar returns show a Gaussian distribution which is described as follows [e.g., Woodman, 1985],

$$S(f) = \frac{P}{\sqrt{2\pi}\sigma} \exp\left[-\frac{(f - f_d)^2}{2\sigma^2}\right] \tag{3.3}$$

where P, f_d and σ are echo power, mean Doppler shift and spectral width, respectively.

One of the techniques to determine these parameters is a moment method. The zeroth, first and second moments of the spectral density correspond to the echo power, mean Doppler shift and spectral width, respectively. For an observed spectrum $S'(f_i)$ obtained at M discrete frequencies f_i,

$$P = \sum_{i=1}^{M} S'(f_i) \tag{3.4}$$

$$f_d = \frac{1}{P} \sum_{i=1}^{M} f_i S'(f_i) \tag{3.5}$$

$$\sigma^2 = \frac{1}{P} \sum_{i=1}^{M} (f_i - f_d)^2 S'(f_i) \tag{3.6}$$

Another technique is a least squares fitting method. A Gaussian spectrum is fitted to the observed one so as to minimize the squared sum of the residual

$$\varepsilon^2 = \sum_{i=1}^{M} [S'(f_i) - S(f_i; P, f_d, \sigma)]^2 \tag{3.7}$$

by changing the parameters P, f_d and σ. The spectral parameters may also be estimated from the autocorrelation function of the time series of the radar returns. The radial velocity is estimated from the phase angle of the autocorrelation function at the first lag [e.g., Woodman and Guillén, 1974]. Also, Sato

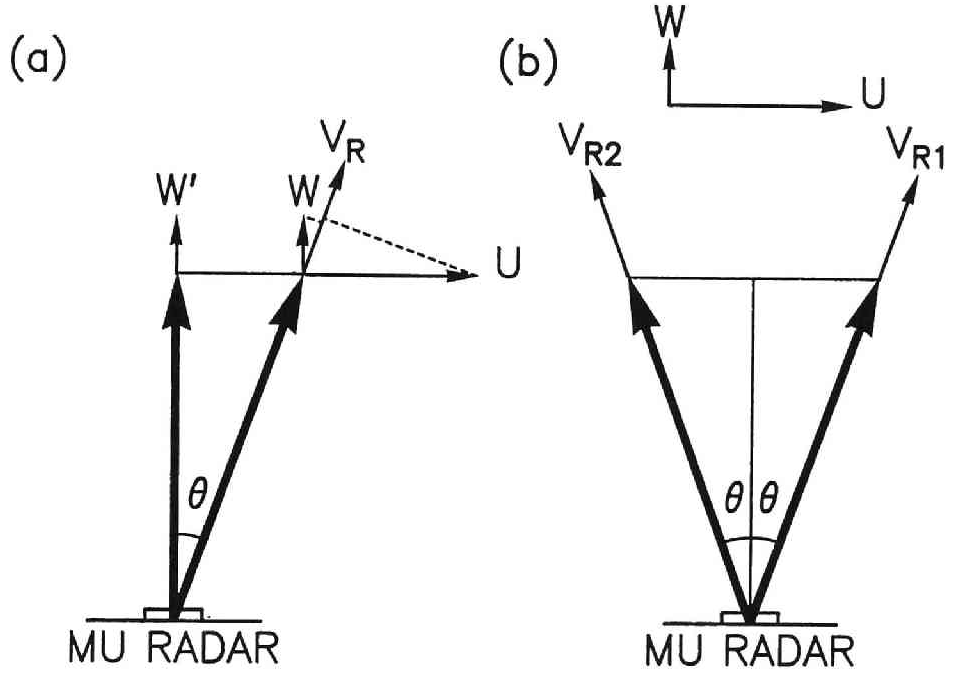

Figure 3.3: Schematic diagram of the typical beam directions used in the MU radar observations. The left (a) and right (b) panels show the vertical and oblique beams, and two oblique beams in the opposite directions with the same zenith angle θ, respectively. The horizontal velocity is calculated by assuming no spatial difference in the wind field within these beams.

and Woodman [1982] applied a least squares fitting technique to the autocorrelation at multiple delays when radar returns consist of a component from fading ground clutter together with the turbulence echo.

For parameter estimation, the fitting method is utilized in almost all of the MU radar observations. It is because this technique may be expected to show better results compared with other techniques especially in the region with low SNR. In the next section, we calculate the estimation error of the fitting method by computer simulation.

The main beam of the MU radar can be directed within 30° around the zenith. We need to use at least two beams to obtain horizontal wind velocities. Figure 3.3 schematically shows the typical beam directions in the vertical plain. The radial wind velocity V_R obtained in the oblique beam is given by

$$V_R = U \sin\theta + W \cos\theta \tag{3.8}$$

where U, W and θ are horizontal and vertical wind components and the zenith

angle of the beam, respectively. We neglect the spatial difference in the wind field in order to calculate U. When vertical and oblique beams are used as shown in Fig. 3.3 (a), U is calculated by assuming $W \approx W'$ as follows:

$$U = \frac{V_R - W' \cos\theta}{\sin\theta} \tag{3.9}$$

where W' is the vertical wind velocity observed in the vertical beam. This technique is utilized in the comparison observations shown in this chapter. When two beams are steered in the opposite directions with the same zenith angle, which is shown in Fig. 3.3 (b), radial velocities observed in the beam 1 and 2 are

$$V_{R1} = U \sin\theta + W \cos\theta \tag{3.10}$$

$$V_{R2} = -U \sin\theta + W \cos\theta \tag{3.11}$$

where we assume no spatial difference in the wind field. Thus, U is calculated as follows:

$$U = \frac{V_{R1} - V_{R2}}{2 \sin\theta} \tag{3.12}$$

This equation is used for the observations shown in Chapter 4.

3.2 Accuracy of parameter estimation

The performance of many estimators were compared by Zrnić [1979] and Woodman [1985], and the performance of the pulse-pair method was shown to be better than that of the moment method at low SNR although they are the same at infinite SNR. Zrnić [1979] has shown the theoretical minimum estimation error (Cramér-Rao bound) of spectral parameters which is obtained by maximum-likelihood (ML) estimators. However, there are no theoretical calculations for the performance of the fitting method. By using the computer simulation technique, Yamamoto *et al.* [1987c] have discussed the performance of the fitting method, and compared it with the moment method. They have also investigated problems which may occur with the fitting method when it is applied to the power spectrum of a random process, and have shown a possibility to improve the performance of the fitting method and to approach the Cramér-Rao bound.

3.2.1 Techniques for computer simulations

As shown in Fig. 3.4 (a), we have calculated a power spectral density of $S(f_i) + P_N$ at 128 discrete frequencies f_i, where P_N is noise level density.

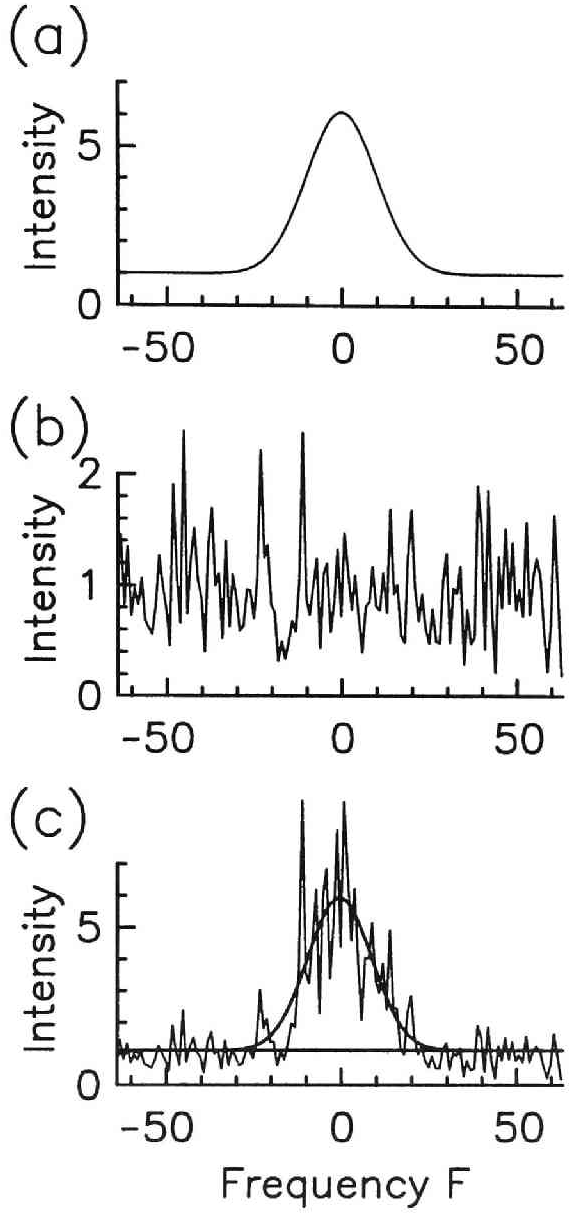

Figure 3.4: An example of (a) Gaussian spectrum, (b) statistical fluctuation and (c) model spectrum utilized in the computer simulation. Frequency F is normalized by the frequency interval between the discrete spectral components. Signal-to-noise ratio, spectral width, number of incoherent integrations and noise level of the model spectrum are $S_N = 1$, $W = 10$, $N = 5$ and $P_N = 1$, respectively.

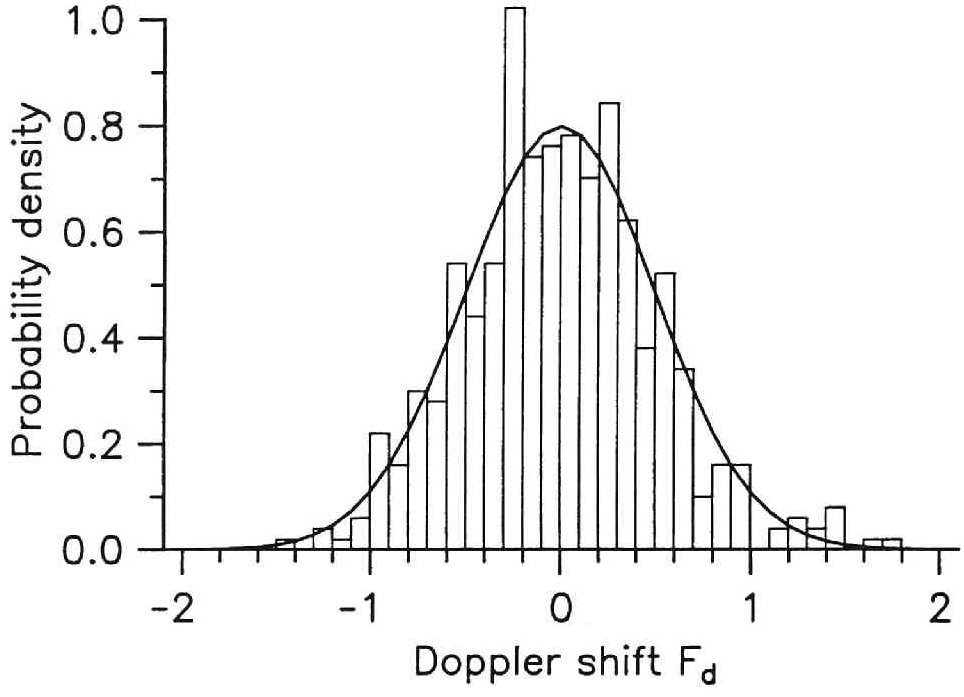

Figure 3.5: Distribution of 500 samples of Doppler shift F_d estimated by the fitting method. The simulation condition is $S_N \to \infty$, $W = 3$ and $N = 5$.

For convenience, the Doppler shift f_d is assumed to be 0. The signal-to-noise ratio of the spectrum is defined as the power ratio between the signal and the noise as follows,

$$S_N = \frac{P}{MP_N} \tag{3.13}$$

where $M = 128$ is the number of discrete frequencies. In the following sections, we use a normalized frequency and spectral width

$$F = \frac{f}{\Delta f} \tag{3.14}$$

$$W = \frac{\sigma}{\Delta f} \tag{3.15}$$

where Δf is a frequency interval between the discrete spectral components.

As cited in Section 3.1, the statistical fluctuation is proportional to the spectral density itself. The statistical fluctuation of the spectrum is simulated by generating random numbers with χ^2-distribution as shown in Fig. 3.4 (b).

This fluctuation corresponds to the number of incoherent integration $N = 5$. Figure 3.4 (c) shows the model power spectrum calculated as a product of the Gaussian spectrum and the statistical fluctuation.

Spectral parameters are estimated for each spectrum by using both the moment and the least squares fitting method. First, the generated spectrum is smoothed by using a numerical low pass filter with a cutoff period of $20\Delta f$. We find the frequency point with the largest spectral density in the smoothed spectrum, which is used as the first guess of the Doppler shift. The low pass filter consists of a running mean with the Hann's window. The goodness of the initial guess depends largely on the shape of the window function, especially for poor SNR. The Hann's window used here gives a substantially better estimates than simple box-car or triangular windows. After subtracting the initial P_N from the original spectrum, we have applied both techniques for 64 spectral points around the first guess.

An additional difference between the two techniques is that we have used all spectral points above and below the noise level in the fitting technique, whereas only positive spectral points are used in the moment method. The smoothed curve in Fig. 3.4 (c) shows an example of the spectrum estimated by the fitting method. It should be noted that the performance of both the fitting and the moment methods rely on the goodness of the initial guess of the Doppler shift. Actually, the low pass filter operation involved in deriving the initial guess takes more computer time than the fitting or the moment method themselves.

In order to obtain the estimation errors of parameters, we have calculated 500 model spectra and obtained the bias and variance of the estimates. Figure 3.5 shows a distribution of the Doppler shift determined by the fitting method. We use a normalized Doppler shift $F_d = f_d/\Delta f$ in this figure. The thick curve shows a Gaussian distribution which corresponds to the bias b_F and variance σ_F^2 of F_d. Because the distribution is close to Gaussian, the number of samples seems to be large enough to apply the statistical procedure. We define the estimation error of the Doppler shift, E_F, as follows:

$$E_F = \sqrt{\sigma_F^2 + b_F^2} \tag{3.16}$$

This is called the "rms error" [Bendat and Piersol, 1971]. E_F in this case is 0.51.

Estimation errors of the spectral width and the echo power are also defined in the same way as shown in Eq. (3.16), and are represented by E_W and E_P, respectively. E_W is normalized by Δf, which is the same as E_F. On the other hand, E_P is described as the ratio to the real echo power P.

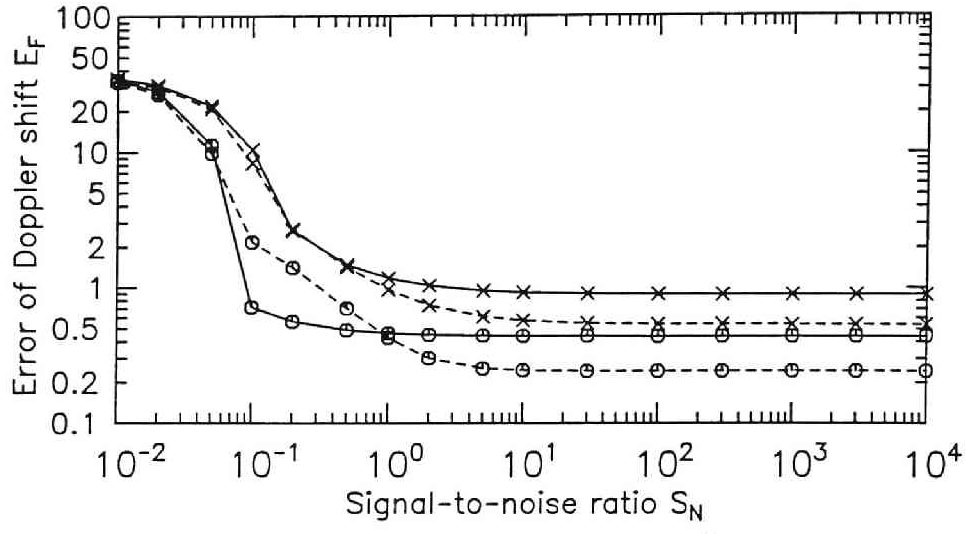

Figure 3.6: Variation of the estimation error of the Doppler shift versus signal-to-noise ratio for $N = 5$. Circle and X symbols show results for $W = 2$ and $W = 10$, respectively. Solid and dotted lines correspond to the error obtained by the fitting and moment methods, respectively.

3.2.2 Estimation error at finite signal-to-noise ratio

Figure 3.6 shows E_F for both the fitting and moment methods versus S_N when $N = 5$. This case corresponds to the estimation error when we averaged five spectra and then applied both methods. When $W = 2$ for the fitting method, E_F is 0.44 in the region with large S_N. The fitting seems to be successful at $S_N > 10^{-1}$ but we recognize a rapid increase of E_F below this level. When we increase the spectral width, the wider spectrum causes a larger estimation error in the Doppler shift; e.g., $E_F = 0.91$ for $W = 10$ at $S_N = 10^4$. However, E_F starts increasing at a similar SNR to that for $W = 2$. It is noted that estimation errors are almost constant with S_N above this level. Comparing the results with that of the moment method, at high S_N, the estimation error of the moment method becomes less than that of the fitting method; at $S_N = 10^4$, $E_F = 0.25$ and 0.52 for $W = 2$ and 10, respectively. The estimation error of the moment method is approximately 60% of the fitting method in this region. As S_N decreases, the estimation error of the moment method gradually increases. The error of moment method at $10^{-1} < S_N < 1$ are almost the same as that of the fitting method for $W = 10$, and worse for $W = 2$. There are no significant bias shown in the low S_N region. Below $S_N = 10^{-1}$, both methods show a rapid increase of the estimation error. The large error is obtained

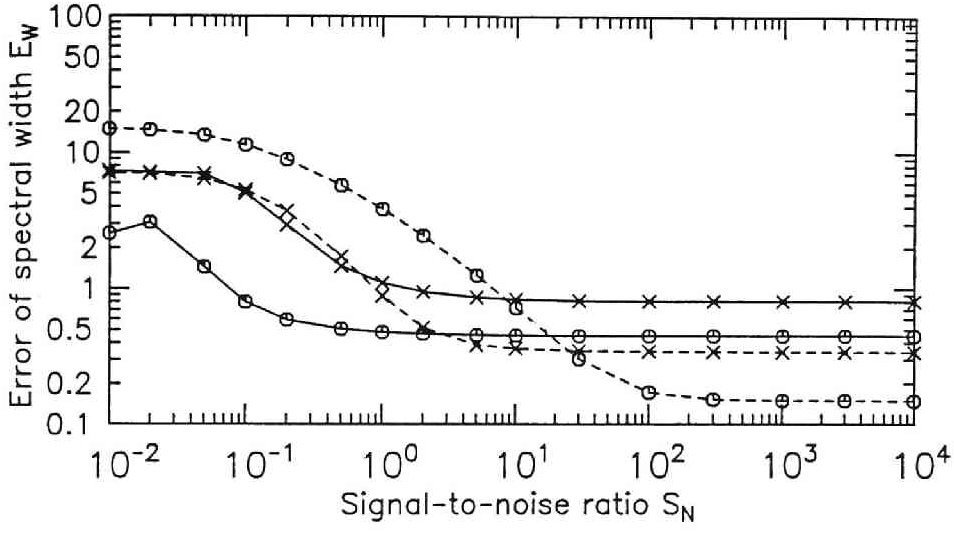

Figure 3.7: The same as Fig. 3.6 except for the estimation error of the spectral width.

because the numerical filter captures the highest peak randomly distributed in the fluctuating noise level, and makes it the first guess of the Doppler shift. When we assume a constant distribution of E_F within the spectral window of $F = \pm 64$, the standard deviation is approximately 37, which is consistent with E_F at $S_N = 10^{-2}$.

Figure 3.7 illustrates the estimation error of the spectral width E_W. At large S_N with $W = 2$, E_W is 0.45 and 0.16 for the fitting and moment method, respectively. Better results by the moment method are also obtained with $W = 10$. E_W of the moment method seem to be about 40% of the fitting method. E_W of both methods does not decrease very much with increasing S_N at $S_N > 10^2$. These results are similar to those of the estimation error of the Doppler velocity. In the low S_N region, W seems to be well estimated for $S_N > 1$ by using the fitting method. However, the performance of the moment method becomes worse at $S_N < 10$. E_W of the moment method is much worse than that of the fitting method for $W = 2$, although E_W for $W = 10$ is not larger than the fitting method at any S_N. The increase of E_W in the low S_N region is due to the increasing bias to the real width. For the fitting method, around $S_N = 10^{-2}$, the estimated spectral width is locked to W of one or two because the estimated spectrum is fixed at the major peak of the statistical fluctuation. On the other hand, the spectral width obtained by the moment method is larger than the real width. It is because the distribution of

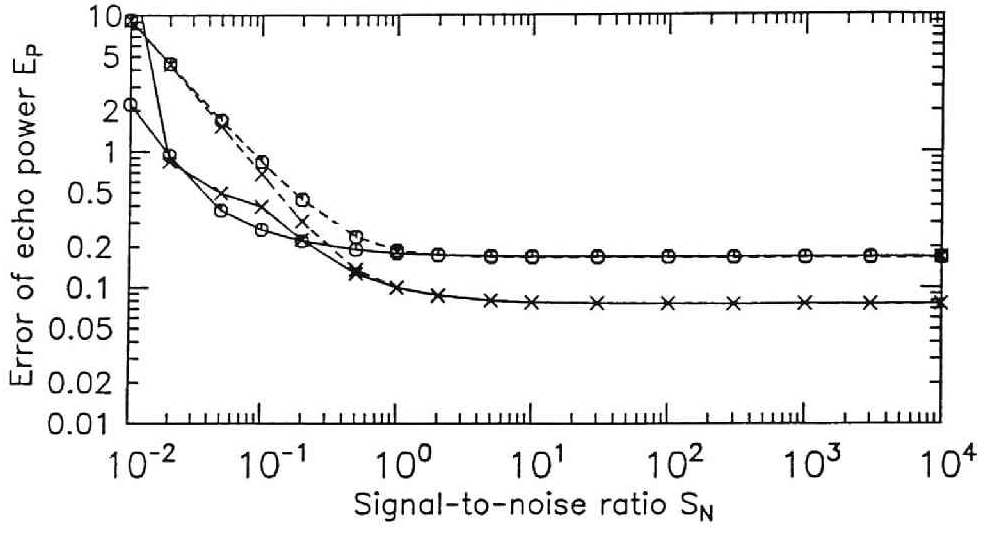

Figure 3.8: The same as Fig. 3.6 except for the estimation error of the echo power.

the spectral density becomes close to the uniform distribution in the spectral points used in the calculation.

As shown in Fig. 3.8, the relative estimation error of the echo power has a different nature compared with E_F or E_W. When $S_N > 1$, the results obtained by both methods are close and almost constant with increasing S_N. E_P is better for larger W; In the high S_N region, the relative estimation errors are approximately 17 and 8% of the real P when W is 2 and 10, respectively. It is because we can average more independent spectral points for the wide spectrum than those for the narrow spectrum.

Comparing the results obtained by the fitting and moment method, the performance of the moment method is better than the fitting technique at high S_N. However, the fitting technique shows better results for the narrow spectrum at $S_N < 1$ for both E_F and E_W. Especially, the fitting technique is the safer estimator for the spectral width in the low S_N region because bias of W in the moment method is largely affected by the number of spectral points used in the calculation.

3.2.3 Estimation error at infinite signal-to-noise ratio

Since the estimation errors of parameters do not vary much according to S_N for high S_N cases, the estimation errors at infinite S_N is a good index for the errors in real observations. Figure 3.9 shows the estimation error of the

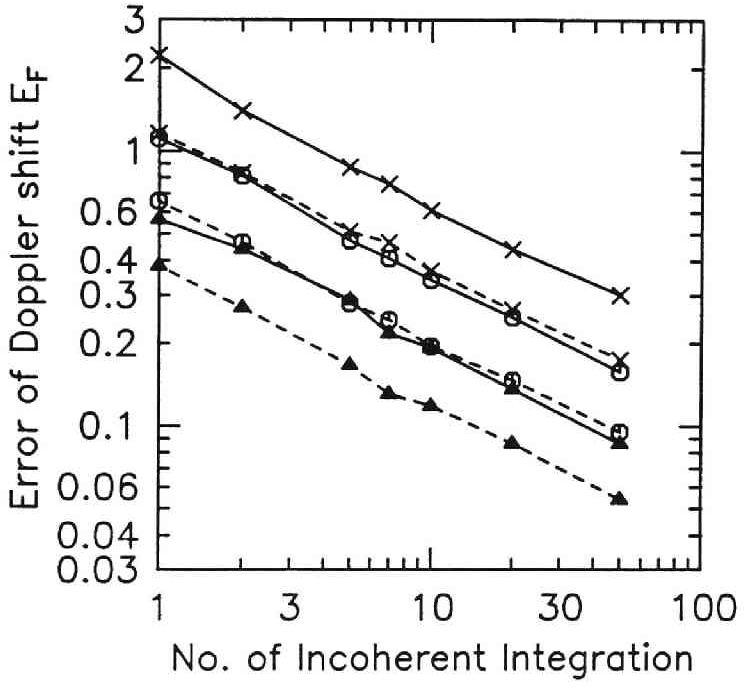

Figure 3.9: Estimation error of the Doppler shift versus number of incoherent integration of the spectra at infinite S_N. Triangle, circle and X symbols show that $W = 1$, $W = 3$ and $W = 10$, respectively. Solid and dotted lines correspond to the error obtained by the fitting and moment methods, respectively.

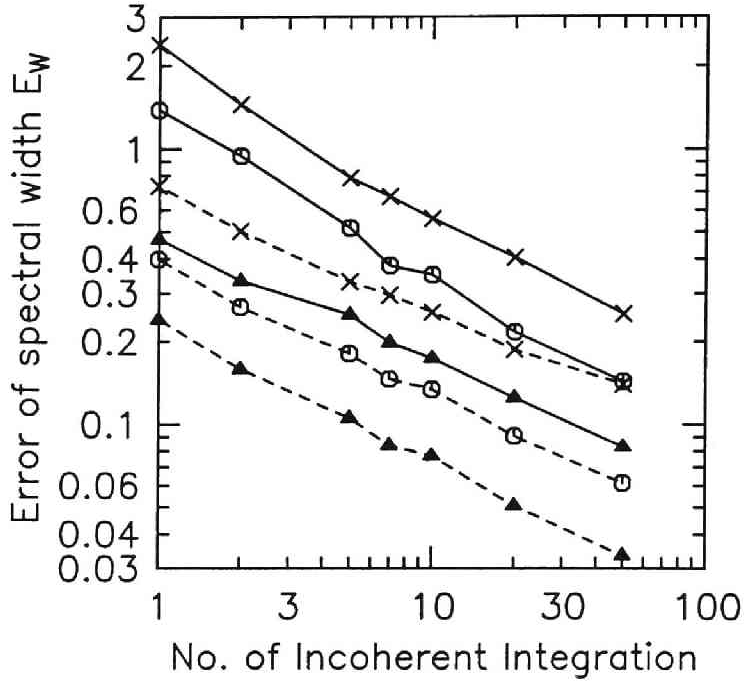

Figure 3.10: The same as Fig. 3.9 except for the estimation error of the spectral width.

Doppler velocity versus number of incoherent integrations of the spectra. The estimation error of the Doppler shift seem to be proportional to $\sqrt{W}$, and inversely proportional to $\sqrt{N}$. For the spectral width, as illustrated in Fig. 3.10, the response of E_W to N and W seems to be the same as that for the Doppler shift. At infinite S_N, the estimation error E of either F_d or W can be described as

$$E = k\sqrt{\frac{W}{N}} \tag{3.17}$$

where k is a constant. By using the data shown in Figs. 3.9 and 3.10, we have determined the constant k for all methods and spectral parameters, which are listed in Table 3.1.

In order to determine the estimation error of the radial wind velocity obtained by both methods, we put physical dimensions to the normalized estimation error E_F. The estimation error ε_v of radial wind v in the unit of ms^{-1} is

$$\varepsilon_v = \frac{c}{2f_0T}E_F \tag{3.18}$$

	Fitting	Moment
F_d	0.63	0.38
W	0.60	0.24

Table 3.1: Coefficient k of Eq. (3.17) for estimation errors of normalized Doppler shift and spectral width.

where c, f_0 and T are the speed of light, the carrier frequency of the radar and the length of the time series of the data, respectively. The spectral width σ_v in the unit of ms^{-1} is also described as follows:

$$\sigma_v = \frac{c}{2f_0T}W \tag{3.19}$$

By substituting Eqs. (3.17) and (3.19) into Eq. (3.18),

$$\varepsilon_v = K\sqrt{\frac{\sigma_v}{T_0}} \tag{3.20}$$

where

$$K = k\sqrt{\frac{c}{2f_0}} \tag{3.21}$$

is a constant and

$$T_0 = TN \tag{3.22}$$

is the total observation period to obtain a set of spectral parameters. Eq. (3.20) shows that, if S_N is infinite, the observation period is the only factor that we can choose when we observe the radial velocity by using the radar. The spectral width in this case should contain all of the broadening effects such as beam and shear broadening besides the spectral broadening caused by the turbulence. We should also note that Eq. (3.20) is valid for the estimation error of the spectral width in the unit of ms^{-1}.

The coefficients K for the estimation error expected in the MU radar observations has been calculated by using the data listed in Table 3.1 and $f_0 = 46.5$ MHz, and shown in Table 3.2. For the moment method, Zrnić [1979] has theoretically calculated the estimation error for both radial velocity and spectral width. The theoretical formulas show that, on the MU radar and with infinite S_N, $K = 0.68$ and $K = 0.41$ for radial wind velocity and spectral width, respectively. These values are consistent with those obtained by the

	Fitting	Moment
Radial velocity	1.1	0.67
Spectral width	1.1	0.43

Table 3.2: Coefficient K of Eq. (3.21) for estimation errors of radial wind velocity and spectral width in the unit of ms^{-1}.

simulations. If we observe the radial wind velocity every 1 min by using the fitting method, $\varepsilon_v = 0.12$ ms^{-1} for $\sigma_v = 0.7$ ms^{-1} which is a typical value in the stratosphere for the MU radar, and $\varepsilon_v = 0.20$ ms^{-1} for $\sigma_v = 2.0$ ms^{-1} which is typical in the mesosphere.

The larger errors with the fitting method seem to occur because of the nature of the statistical fluctuations of spectral coefficients. Because the amplitude of the statistical fluctuations are proportional to the spectral density, components around the spectral peak have larger fluctuations than the spectral components with low spectral density. Thus, the sum of the squared residual is almost solely determined by the spectral components around the peak, which implies that we actually use only a portion of the spectrum when we estimate the parameters by using the fitting method.

3.2.4 Lower bound of the spectral parameter estimation

In order to investigate the performance of both techniques for the parameter estimation, we have calculated the normalized residual of the fitting by subtracting the model spectra $S'(F)$ from the fitted spectra $S(F; P, F_d, W)$ as follows:

$$R(F) = \frac{1}{p}[S(F; P, F_d, W) - S'(F)] \tag{3.23}$$

where p is the real peak power density of the Gaussian spectrum.[1] The solid line in Fig. 3.11 shows $\overline{R(F)}$ for the fitting method which is an average over 500 model spectra with the initial condition of $S_N \to \infty$, $W = 3$ and $N = 5$. If the parameter estimation is successful, $\overline{R(F)}$ should be zero at any F. Considering N and the number of the model spectra, the standard deviation of $\overline{R(F)}$ due to the statistical fluctuation should be 2%. However, we can recognize a systematic variation of the averaged residual. The residual is approximately 2.5% larger than the real spectral density at $F = 0$, and 4% smaller at $F = \pm 4$. The positive $\overline{R(F)}$ means that the estimated spectral component is larger than the real one. Because the residual is positive at the center and negative near the

[1] For the results with the moment method, we assume the Gaussian spectrum $S(F)$ with the estimated parameters, and calculated $R(F)$ as cited above.

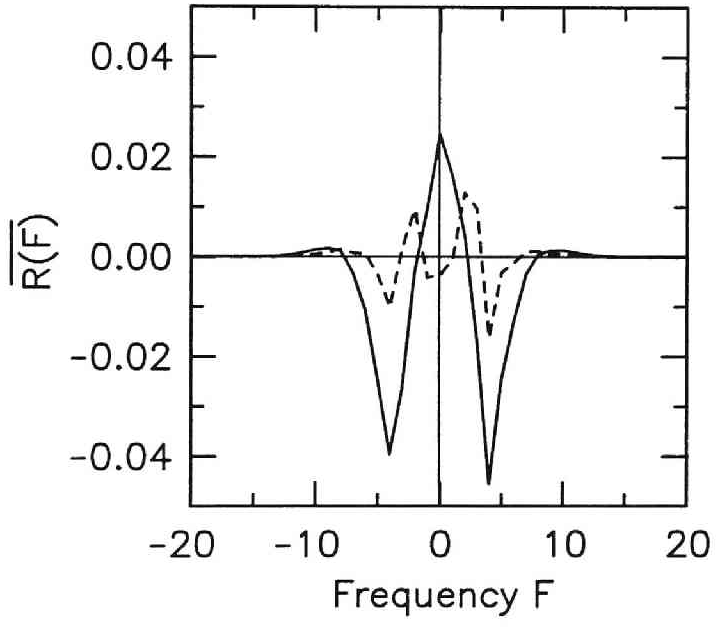

Figure 3.11: Residual of the estimation of the spectra averaged over 500 power spectra. Solid and dotted lines correspond to the results for the fitting and moment methods, respectively.

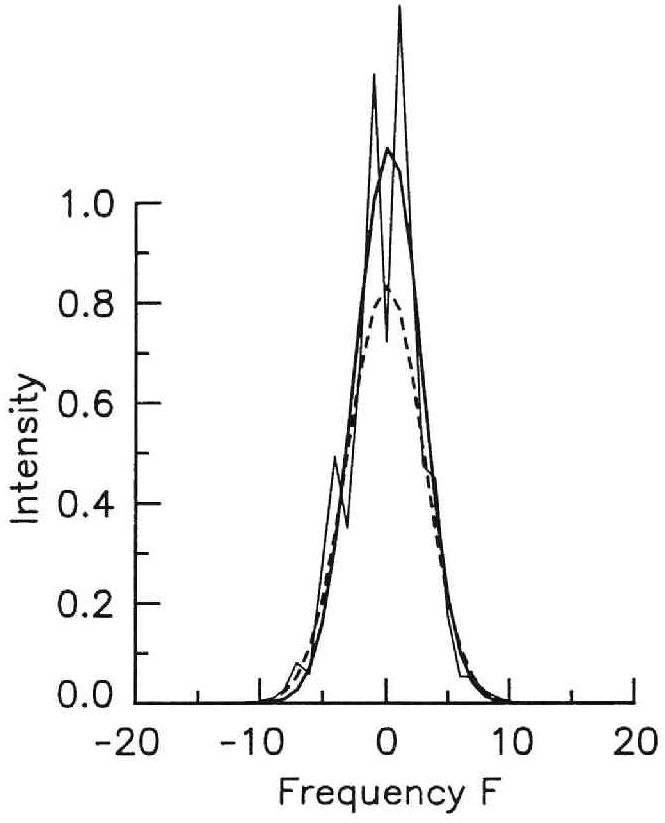

Figure 3.12: Examples of the Gaussian spectrum estimated by two methods at $S_N \to \infty$, $W = 3$ and $N = 5$. Solid and dotted lines show the results estimated by the fitting in the linear domain and the parabolic fitting in the logarithmic domain, respectively. The thin line corresponds to the model spectrum normalized by the real peak power density.

shoulder of the initial spectrum, the spectra are estimated to be narrower than the real spectrum; we can recognize a small negative offset in the distribution of the estimated W. The symmetrical nature of $\overline{R(F)}$ shows that there is no offset in the Doppler shift estimations. The dotted line in Fig. 3.11 shows $\overline{R(F)}$ for the moment method, which is less than about $\pm 1\%$ at any F. Because the amplitude of the fluctuation is less than expected from purely statistical fluctuations, the moment method does not show any significant bias to spectral parameters.

When we apply the least squares fitting method to data, it is required that the observation error should be uncorrelated with the signal and have a Gaussian distribution. Both conditions are not satisfied in the least squares

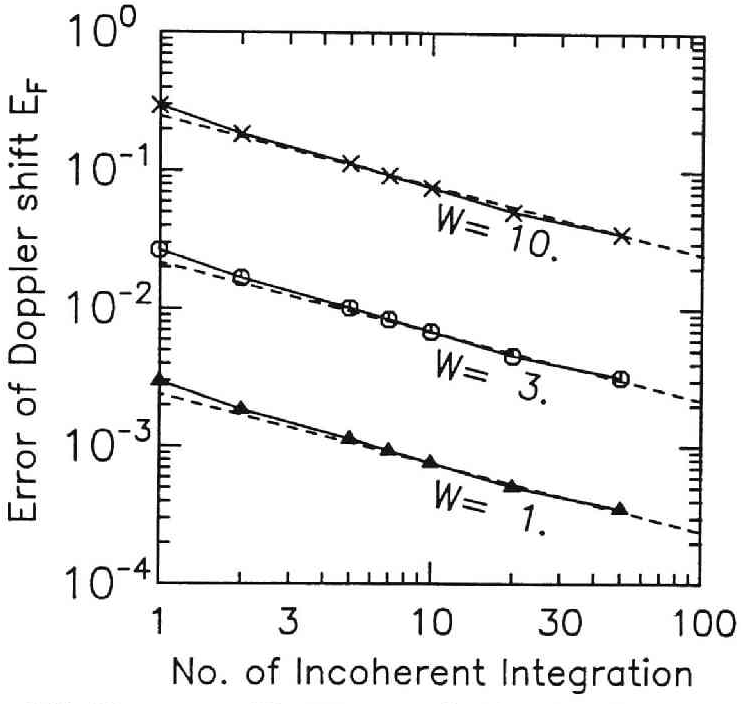

Figure 3.13: The same as Fig. 3.9 except for the estimation error of the parabolic fitting in the logarithmic domain. Dotted lines correspond to the Cramér-Rao bound for the ML estimator shown by Zrnić [1979].

fitting applied to the power spectrum because the statistical fluctuation shows the χ^2-distribution and its amplitude is proportional to the spectral density. This nature of the statistical fluctuation seems to be the reason of the poor performance of the fitting method at large S_N. The χ^2-distribution is not symmetrical against the mean of the spectral coefficient, and tends to have larger spikes on the higher side in its distribution. The solid line in Fig. 3.12 illustrates an example of the estimated spectrum determined by the fitting method. The model spectrum is normalized by the real peak power density of the spectrum. The spikes of the statistical fluctuations which appear around the peak of the Gaussian spectrum seem to cause a large bias to the sum of the squared residual and set the fitted spectrum higher at the center, and narrower than the real one. The estimation of the Doppler shift is also affected by the positions of the spikes.

Since the amplitude of the statistical fluctuation is linearly proportional to the spectral density itself, we can uncorrelate the amplitude of the statistical fluctuations from the spectrum by taking the logarithm of the spectral density.

The amplitude of the statistical fluctuations becomes constant although its statistical distribution is not Gaussian. We can estimate the spectral parameters by fitting a parabolic curve to $\log[S(F)]$ when $S_N \to \infty$. Waldteufel [1976] has shown that fitting in the logarithmic domain constitutes a maximum-likelihood (ML) estimator. As shown by the dotted line in Fig. 3.12, the result of this method fits much better the model spectrum than the fitting in the linear domain in components with low spectral density. We have simulated the estimation error of the Doppler shift for this method. The result of this parabolic fitting is shown in Fig. 3.13. The estimation error obtained by this method is, for example, approximately 20 times less than that by the moment method when $W = 3$. The dashed line is the theoretical lower bound (Cramér-Rao bound) obtained for the error expected for the ML estimator [Zrnić, 1979]. The estimation error of the normalized Doppler shift agrees very well with the Cramér-Rao bound. Although the estimation error is inversely proportional to $\sqrt{N}$, we can recognize that it is almost proportional to W^2. This is different from the $\sqrt{W}$ dependence shown in Eq. (3.17), but agrees well with the theoretical formula given by Zrnić [1979]. The improvement of the estimation error obtained by this fitting in the logarithmic domain is larger for spectra with narrow width than spectra with larger width.

In theoretical evaluations of the accuracy of the pulse-pair or moment method [Doviak and Zrnić, 1984; Woodman, 1985], the accuracy was shown to be comparable to the Cramér-Rao bound. However, they replaced the sampling interval in the equations for the Cramér-Rao bound by the signal correlation time because a sampling faster than the correlation time is redundant in the linear domain since the correlation time determines the spectral width. Faster sampling only introduces higher frequencies with small spectral density. This is not the case for the fitting in the logarithmic domain. Using the original equation for the Cramér-Rao bound, it is much lower than those in previous comparisons.

For a Gaussian spectrum with infinite S_N, every spectral component should have some information no matter how far the component is from the spectral peak. This implies that we can increase the number of independent points in the spectrum, and improve the performance of estimators as much as we wish. The performance of the moment and fitting methods in the linear domain is restricted because the equivalent number of effective spectral components is limited around the spectral peak according to the spectral width. The result clearly shows that at infinite (or very high) S_N, even very high frequency components of the signal spectrum with very small amplitude have substantial importance, and can be used to derive its spectral parameters. In the linear domain, contributions from these components are masked by the much larger

fluctuations of the frequency components around the peak. This simulation shows that the parabolic fitting in the logarithmic domain is one technique to realize the lower bound of the ML estimator by making use of such high frequency components. The disadvantage of this method seems to be accuracy of the echo power. The example of this fitting in Fig. 3.12 shows that the peak spectral density is approximately 10% less than the real value, which is quite a large error considering the excellent performance in the estimation of the Doppler shift. This underestimate comes from the fact that in estimating the echo power, we are basically finding the mean in the logarithmic domain. The mean in the logarithmic domain corresponds to the geometric mean, which is always less than or equal to the arithmetic mean in the linear domain.

This method is not realistic for real data with finite S_N because the spectra are contaminated and distorted by truncation distortion, aliasing effects, quantization error and so on. The estimation error of the noise level will also affect the result. However, if we produce a fitting routine for $\log[S(F)]$ which contains these contaminations, e.g., Waldteufel [1976], it should show much better performance than the existing methods.

3.3 Comparison observations with other techniques

Simultaneous observations of mesospheric winds were carried out on two consecutive days by using the MU radar and the Kyoto meteor radar. The purpose of this section is to make a comparison of the two kinds of data [Tsuda *et al.*, 1985a].

3.3.1 Observations

The data of the MU radar are based on the observation on 14–15 August 1984. Because the MU radar was under construction at that time, we used only 361 TR modules (19/25 of the final system) which operate at a peak transmission power of approximately 750 kW. Therefore, the sensitivity of the radar for the turbulence scattering was 0.58 of the final system. The transmitted pulse was phase-modulated by a 16-bit complementary code with a baud length of 2 μs. The inter pulse period (IPP) was 800 μs, so that the duty factor was 0.04. The antenna main beam was steered every IPP and pointed in the vertical direction and then toward the north and the east at a zenith angle of 10°. Quadrature signals were sampled at intervals of 300 m from 60 km to 98.1 km and were coherently integrated over 30 pulses for echoes in each direction. The

signals were transferred into power spectra by using a 128-point FFT, and then the spectra were incoherently accumulated 10 times. The power spectra were recorded on magnetic tape every 105 s.

Figure 3.14 shows height profiles of echo intensity integrated over 1000–1200 LT on 15 August 1985 in the vertical and the two oblique directions. Below about 80 km the signal power was largest in the vertical direction by several decibels, a feature which has previously been reported for Jicamarca observations [Fukao *et al.*, 1979]. For the turbulence layer at 82–85 km altitudes, the weakest power was detected in the vertical direction, and the eastward pointing antenna received more power than the northward beam.

We have taken two approaches to infer the wind profile in the 65–95 km region.

1. Meteor echoes are removed by using their discontinuous nature along time and height before the integration of power spectra. Then, ten records of power spectra are incoherently integrated. Eastward and northward horizontal wind velocities are calculated taking the vertical wind velocity into account by using Eq. (3.9). This analysis is applicable for constructing the wind profile below 80 km.

2. In the region above 80 km, where meteor echoes dominate turbulence scattering, we have utilized meteor echoes to deduce wind profiles as has been applied to Poker Flat MST radar observations [Avery *et al.*, 1983]. Meteor echoes were received intermittently, so that they usually did not give a complete set of radial wind velocities in three direction at the same time. Therefore the horizontal wind velocity was estimated with the assumption of zero vertical velocity. Because meteor echoes are not necessarily received in the direction of antenna bore sight, accumulation over a longer period than the first method is needed to find the average radial wind in the collecting volume of the main beam. Furthermore, since we did not discriminate against meteor echoes received in the side lobes of the antenna, there is a possibility that radial wind velocities in the directions other than that of the main beam may contaminate to the accumulated wind velocities. To remove random fluctuation of the wind fields, the wind profiles deduced from methods 1 and 2 were smoothed over three and five adjacent altitudes, respectively.

The Kyoto meteor radar has been regularly monitoring mean winds, planetary waves and atmospheric tides at 80–110 km altitudes [Aso *et al.*, 1980; Tsuda *et al.*, 1983; Ito *et al.*, 1984]. For observations in August 1984, the antennas were pointed in the eastward direction at an elevation angle of 45°. At meteor heights, the mean horizontal separation between the meteor radar observations and the MU radar observations is approximately 100 km. Because the antenna beam width is fairly large, the meteor echoes can be distributed

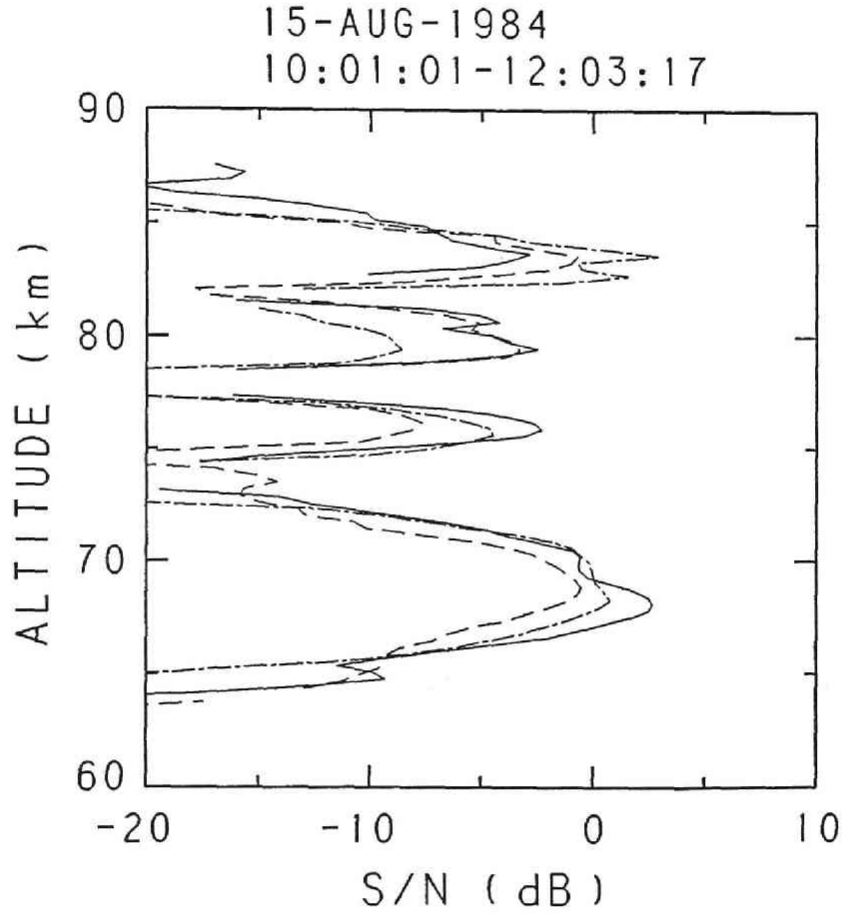

Figure 3.14: Mean signal-to-noise ratio between 1000 and 1200 LT on 15 August 1984, in the vertical (solid curves), northward (dashed curves) and eastward (dashed-dotted curves) directions.

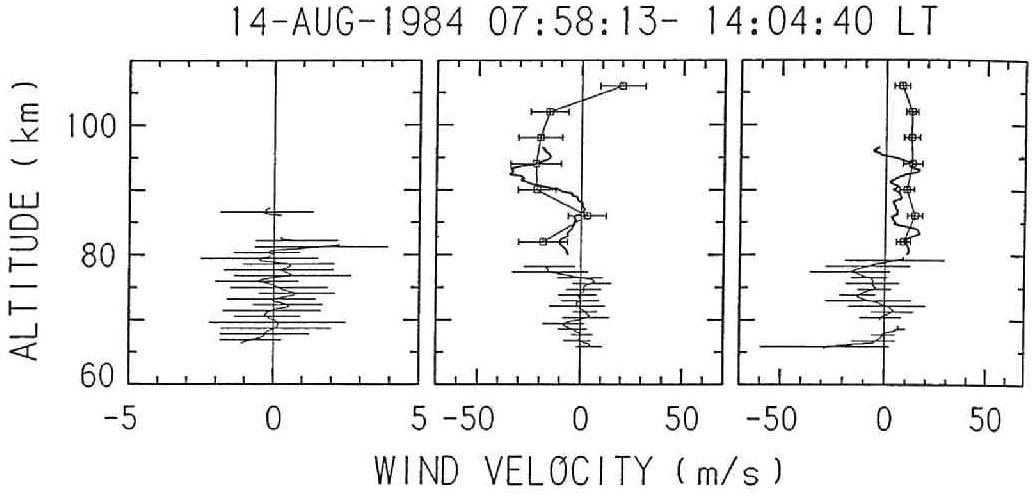

Figure 3.15: Mean wind profiles for (left) vertical, (center) northward and (right) eastward components observed between 8–14 LT on 14 August 1984. MU radar measurements using the turbulence scattering (solid curves with bars) and meteor echoes (thick solid curves) are compared with Kyoto meteor radar observations (Squares).

widely in azimuth. Thus the observed radial wind velocity usually contains both zonal and meridional components. A fitting analysis, using time-height bins of 2 hr $\times$ 4 km, can usually provide both components by using measurements of the arrival angle for each meteor echo obtained using an interferometer analysis. However, the zonal component is more reliably determined than the meridional component. The number of meteor echoes varies diurnally with the maximum rate occurring early in the morning, and the rate is sometimes insufficient to deduce the vertical profile of wind fields around sunset [Tsuda, 1982].

3.3.2 Comparison of wind fields

Figures 3.15 and 3.16 show the mean wind profiles of the vertical, northward and eastward components observed between 65 and 100 km measured from the MU radar observations during 8–14 LT on 14 and 15 August. The two kinds of measurements by the MU radar as described in Section 3.2.1 show a fairly continuous and smooth variation with altitude. Bars for the MU radar measurements using turbulence scattering indicate the standard deviation of the wind fields during the observation period.

Kyoto meteor radar observations of wind profiles in 82–106 km region on 14

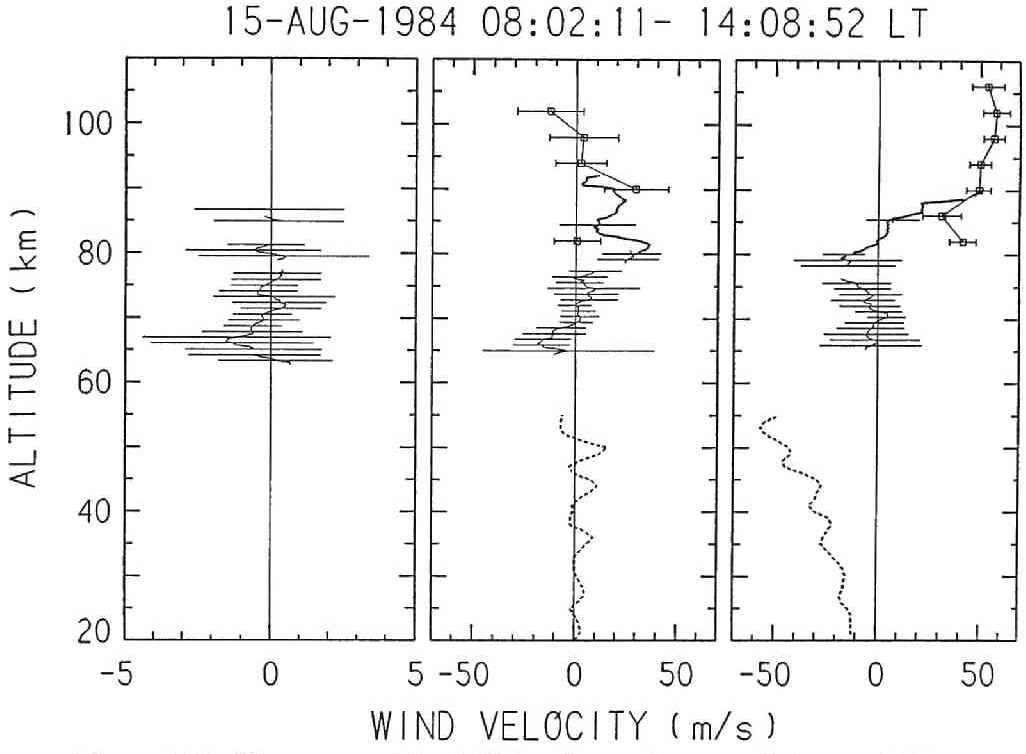

Figure 3.16: The same as Fig. 3.15 for observations on 15 August 1984. Rocket measurements of wind profiles are also plotted (dotted curves).

and 15 August are also shown in Figs. 3.15 and 3.16, respectively. The height range does not overlap with that of the MU radar measurements using turbulent echoes. However, a continuity of vertical profiles with different techniques is recognized on both days. Comparisons of the two kinds of meteor radar measurements by the MU radar and the Kyoto meteor radar show that overall wind profiles agree quite well as in Fig. 3.15. Large wind shears at around 90 km for both northward and eastward components were well deduced in Fig 3.16, although differences are recognized at 82 km. The meridional component from the meteor radar observations at 86 and 106 km could not be delineated because of large deviation in the fitting analysis. Discrepancies might be attributed, first, to the smoothing of smaller scale waves in the relatively large searching volume of the Kyoto meteor radar and, second, to the less uniform temporal distribution of meteors at 82 km.

Figure 3.16 also shows a meteorological rocket measurements made at 1120 LT over Ryori (39°02′N, 141°50′E) located approximately 700 km northeast of the MU radar. Although the MU radar observations did not overlap

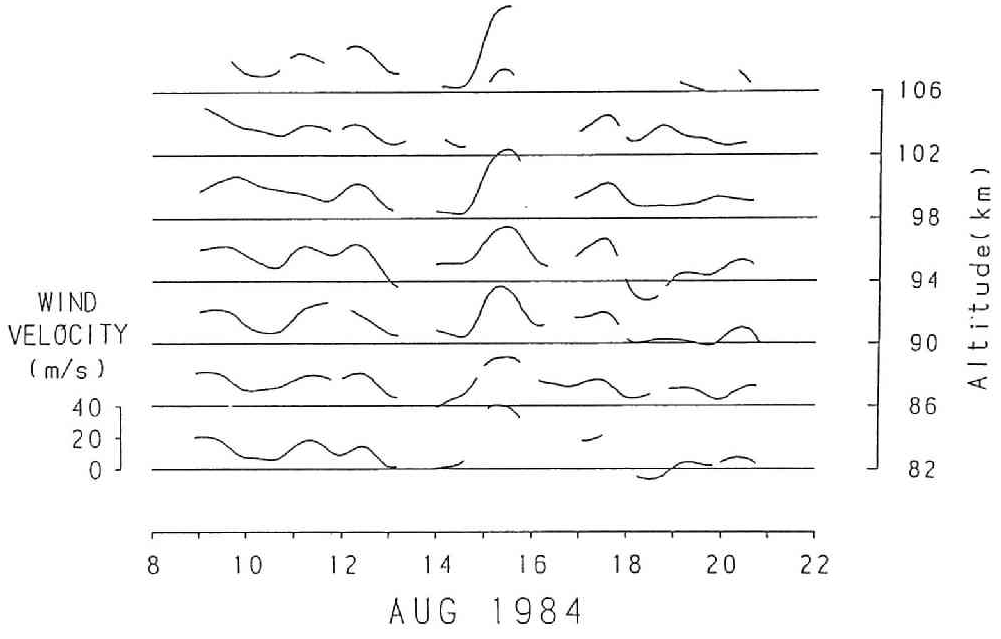

Figure 3.17: Eastward wind velocities observed by the Kyoto meteor radar after filtering short-period components less than 32 hr.

over the altitude range where the rocket measurements were carried out, the vertical profiles seem to show overall continuity.

In Figs. 3.15 and 3.16 we notice that the amplitude of the vertical component was less than 2 ms^{-1} throughout the region and did not show distinct day-to-day variation. However, considerable day-to-day differences are recognized between horizontal wind profiles above 80 km. The amplitudes of the zonal components were as small as 10–15 ms^{-1} on 14 August, while they ranged from 30 to 60 ms^{-1} accompanied with a large wind shear at 80–90 km in the following day. The meridional component was generally southward on 14 August and became northward on 15 August. In each wind component, small-scale fluctuations with short vertical wavelengths were superimposed on the mean profiles.

The oscillations with periods longer then 32 hr are plotted in Fig. 3.17 for the zonal component detected from Kyoto meteor radar observations in the period 9–20 August 1984. The quasi-2-day oscillation seems to have been enhanced in the period of comparison observations, producing differences in background wind fields on 14 and 15 August. The amplitude of the zonal component was thus small on the first day but became large on the following day.

3.4 Concluding remarks

In this chapter, we have shown basic techniques to process the MU radar data, and investigated the performance of the MU radar in the observations of the middle atmosphere.

In Section 3.2, accuracy of spectral parameter estimators were studied. We have compared the performance of the fitting and the moment methods by using computer simulations. The comparison showed that the moment method was better than the fitting technique in large SNR region. Also, we have found a problem of the fitting technique which is the bias toward slightly narrower spectral width estimates. Both the poor performance and the spectral width bias of the fitting method seem to be due to the nature of the statistical fluctuations of the spectral estimates. Because the amplitude of the statistical fluctuation is proportional to the spectral density, parameters are determined mainly by the spectral points around the peak. However, the fitting technique showed better results in the low SNR region especially for the narrow spectrum. In order to estimate the spectral width in this region, the fitting technique is the safer estimator because the spectral width obtained by the moment method tends to show large positive bias to the true width.

In order to improve the estimation errors of the spectral parameters, we should use the moment method when SNR is adequate to produce better results, and use the fitting method in the low SNR region. This switching between both methods seems to be a good compromise for the stratospheric observations. For the mesospheric observation, however, the fitting method shows an adequate performance because usually $S_N < 10$ in the mesosphere.

As shown in 3.2.4, the performance of both fitting and moment methods are much worse than the Cramér-Rao bound expected by using a ML estimator. This is because they utilize only a restricted portion of the spectral components around the peak to determine spectral parameters. Although the theory does not show the algorithm to derive the best performance of the ML estimator, we could obtain the minimum estimation error of the Doppler shift in an ideal case by calculating the logarithm of the model spectra, and fitting a parabolic curve to this. However, this technique is not realistic for the spectra with finite SNR because there are systematic distortions of the spectra. It may be possible to improve the performance of the estimators by producing a fitting technique for $\log[S(f)]$ with taking these distortions into account.

In Section 3.3, We have deduced wind profiles in the mesosphere from both MU radar and Kyoto meteor radar observations. Comparisons of the wind velocities among these different techniques showed fairly continuous vertical profiles in the 65–106 km region. The large day-to-day difference in the wind

fields measured by the MU radar was attributed to a quasi 2-day wave which was observed in the long duration data of the Kyoto meteor radar. We could also infer that the MU radar showed a consistent wind field with that observed by the meteorological rocket sounding at Ryori because both wind fields seemed to show overall continuity. It has been shown that the mean Doppler shift observed by the MU radar represents the real atmospheric motion, and can be used to investigate the atmospheric dynamics in the middle atmosphere.

Chapter 4

Observations with the MU radar

4.1 Introduction

Observations show that gravity waves in the middle atmosphere dissipate and lose their energy through instability processes [Manson *et al.*, 1979; Vincent and Stubbs, 1977; Vincent, 1984a]. Hodges [1967] pointed out that gravity waves could dissipate through convective instabilities when the background potential temperature became superadiabatic. As shown in Chapter 1, gravity waves transfer their momentum to accelerate the mean wind [Lindzen, 1981]. Fritts and Rastogi [1985] have shown that one of the dynamical instabilities in the atmosphere is the Kelvin-Helmholtz instability, which sets in when the Richardson number of the wind profile is less than 1/4 [Drazin, 1958]. It is very important to observe the relation between gravity waves and instabilities in order to understand the dynamics of the middle atmosphere.

By using Doppler radars, VanZandt *et al.* [1979] and Klostermeyer and Rüster [1980, 1981] observed fluctuations of radial wind velocities with rapid phase jumps at certain altitudes. Through comparison with model calculations, these fluctuations were attributed to Kelvin-Helmholtz instabilities induced by a shear at the bottom of the jet stream. In the mesosphere, Klostermeyer and Rüster [1984] observed echo power bursts and simultaneous oscillations of radial velocity at the maximum shear of the wave structure of the background wind. Although these oscillations were attributed to a Kelvin-Helmholtz instability, Klostermeyer and Rüster [1984] did not show the amplitude and phase profiles of the fluctuation.

The MST radars detect returns from turbulence which are expected to be generated by dissipating gravity waves in the mesosphere. Echo power observed

Observation period	8 February 1985	13,14 February 1986
Observation range	60–98.1 km	60–98.1 km
Beam directions	Northward (θ=10°)	Vertical
(θ: Zenith angle)	Eastward (θ=10°)	Northward (θ=10°)
	Southward (θ=10°)	Eastward (θ=10°)
	Westward (θ=10°)	Southward (θ=10°)
		Westward (θ=10°)
Range resolution	300 m	600 m
		(sampled every 300 m)
Time resolution	120 s	150 s
Inter pulse period	730 μs	730 μs
Pulse compression	16 bit complementary	8 bit complementary
Coherent integration	30 times	20 times
Incoherent integration	10 times	6 times

Table 4.1: Observation parameters with the MU radar

by the MST radar is a good index of turbulence intensity, and can be utilized to obtain turbulence structure constant C_n^2 in the atmosphere [VanZandt *et al.*, 1978]. Relations between gravity waves and turbulence layers are also discussed in this chapter.

We have conducted mesospheric observations with the MU radar in two observational periods on 8 February 1985 and on 13 and 14 February 1986 [Yamamoto *et al.*, 1987a,b,d]. The altitude range of the observations was 60–98.1 km. Fundamental observation parameters are listed in Table 4.1. On 8 February 1985, we used four beams pointing northward, eastward, southward and westward each with a zenith angle of 10°. We steered the beam during every inter-pulse period, and 30 successive echoes were coherently integrated. This corresponds to a sampling interval of 87.6 ms, and the Nyquist limit of the radial wind velocity was 18.4 ms^{-1}. Ten successive power spectra of the received signal were incoherently integrated, and stored on magnetic tapes every two minutes. On 13 and 14 February 1986, the major differences of the observation parameters were the range resolution and the number of beam directions. The range resolution was 600 m with 300 m oversampling in this period while it was 300 m in the first observation. Also, we have used the vertical beam additionally to the four oblique beams we used in the first observation.

Echo power, radial wind velocity and spectral width are determined by a

least squares fitting of Doppler spectra. By taking into account the vertical wind velocity, the eastward and northward components of wind velocities were calculated by using Eq. (3.12) from radial wind velocities measured in east-west and north-south directions, respectively.

4.2 A saturated inertia gravity wave

With the observations on 8 February 1985, Yamamoto *et al.* [1987b] have found a monochromatic inertia gravity wave in the mesosphere. In this section, we show results of the observations and discuss the relations among gravity waves, wind fluctuations, and echo power intensity.

4.2.1 Inertia gravity wave

Figure 4.1 shows horizontal wind profiles observed on 8 February 1985, each of which is a 2-hr average determined every hour. The dashed lines are the vertical linear trends. The trends of the northward wind velocities lie between -30 and 30 ms^{-1}, and show a northward shear of approximately 4.5 $ms^{-1}km^{-1}$. The vertical linear trends of the eastward wind velocities lie between 10 and 50 ms^{-1} with an eastward shear of approximately 3.5 $ms^{-1}km^{-1}$ in the first three profiles. The eastward wind profiles at 14 and 15 LT, however, exceed 50 ms^{-1} at altitudes above 75 km. These data seem to be contaminated because of the weak echo power, and we exclude eastward wind profiles after 14 LT from the following discussions. Until 14 LT, all northward and eastward wind profiles clearly show a monochromatic wave-like structure superposed on each vertical linear trend. We note that the amplitude of the wave-like structure is large and comparable to the range of the vertical linear trend of the wind profile. The vertical phase velocity of the wave is approximately 0.4 $kmhr^{-1}$, which is estimated by using the northward wind profiles. From the profile at 13 LT, the vertical wavelength is approximately 5.6 km, and the apparent period is approximately 13 hr. The vertical wavelength seems to be too short for that of the fundamental modes of semidiurnal tides usually detected in the mesosphere [Kato, 1980]. By using the data obtained by the Kyoto meteor radar, we found that, in February 1985, the vertical wavelength of the semidiurnal tide was 75 km in the altitude range of 80–110 km. The amplitudes of the semidiurnal and diurnal tides were both less than 10 ms^{-1} in the altitude range of 80–90 km, which agree with seasonal variation of semidiurnal tides detected by the Kyoto meteor radar [Vincent *et al.*, 1987]. We would infer that the wave shown in Fig. 4.1 is not largely affected by semidiurnal tides,

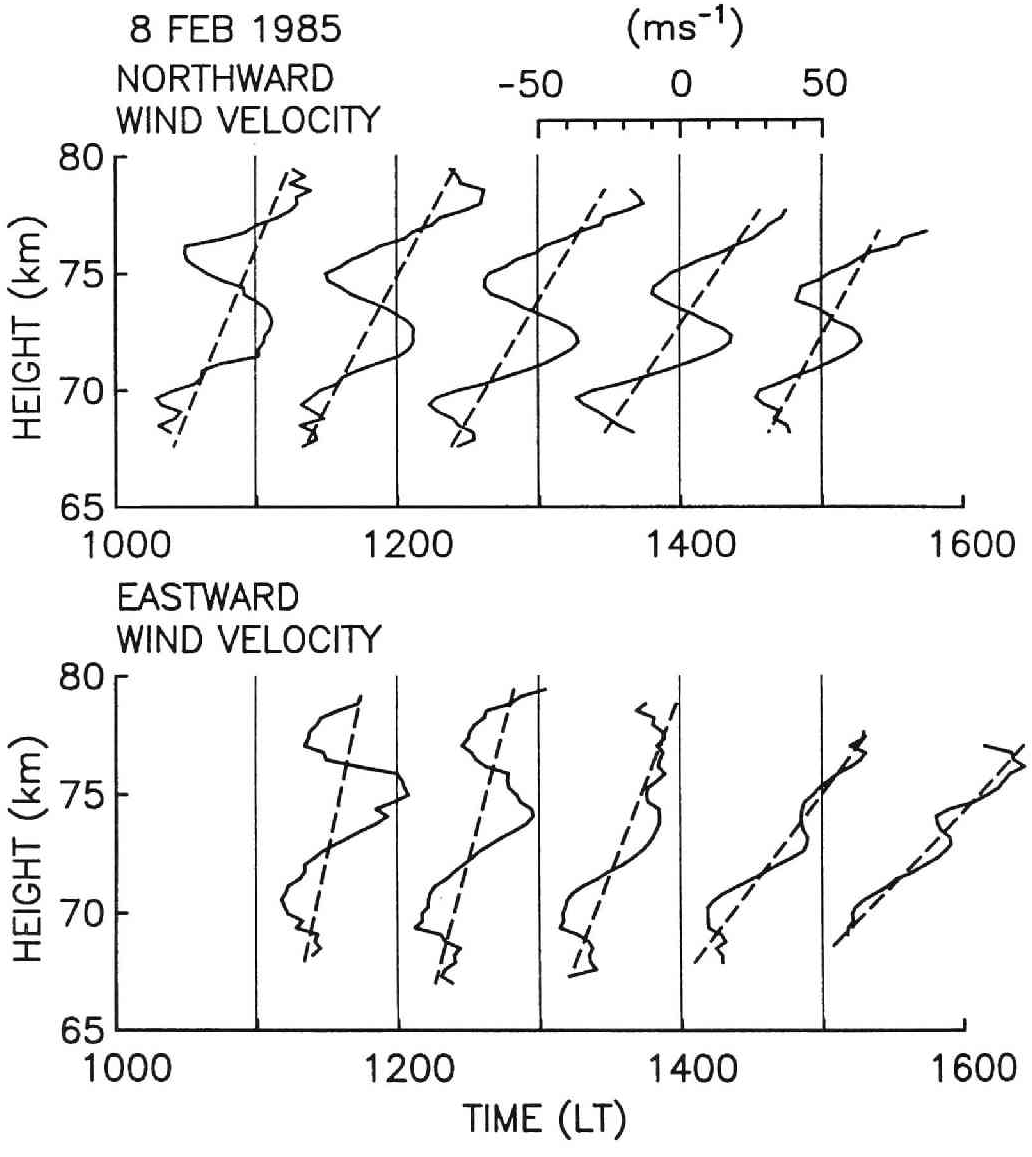

Figure 4.1: Northward (top) and eastward (bottom) wind profiles observed on 8 February 1985. Each profile is averaged over 2 hr with 1 hr overlap. Dashed lines show linear trends of each wind profile.

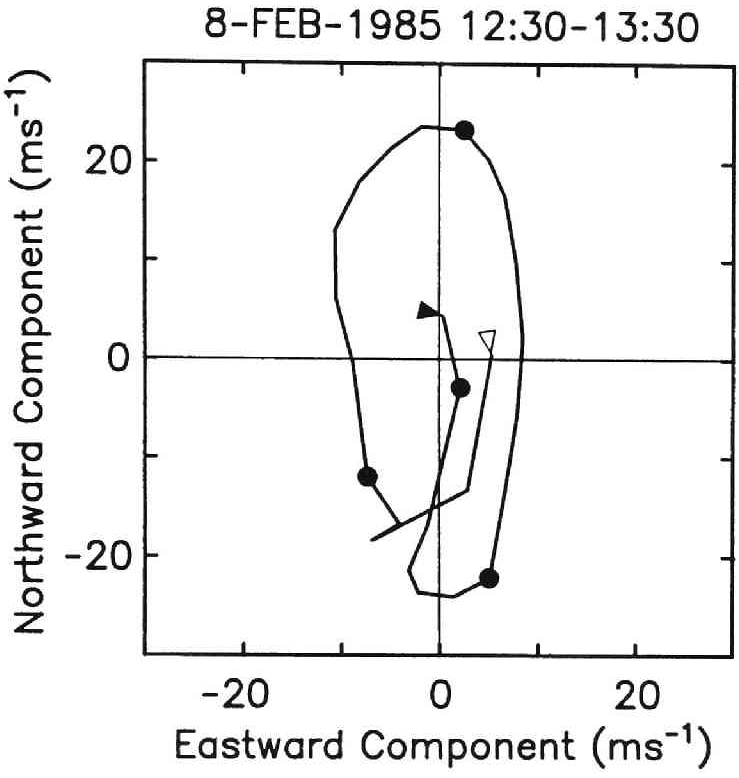

Figure 4.2: A polar plot of the wind velocity averaged over 1230–1330 LT on 8 February 1985. Vertical linear trend of the wind profile is subtracted. The open and solid triangles on the solid line indicate the lowest (68.8 km) and highest altitudes (76.5 km). Circular symbols are plotted at 70, 72, 74 and 76 km.

but is a manifestation of inertia gravity waves.

In order to investigate the polarization of the wave, a height profile of the wind velocity vector is calculated by averaging the eastward and northward components obtained during 1230–1330 LT. Figure 4.2 shows a hodograph of the wind vector after subtracting the vertical linear trend of the profile. The tip of the wind vector moves clockwise with increasing height throughout the whole altitude range. Especially, it shows a clear elliptical motion with a long-axis along the north-south direction below 74 km. This suggests that the wave is an inertia gravity wave which propagates its energy upward [Gossard and Hooke, 1975]. As shown in Eq (1.30), we can estimate the intrinsic period of the gravity wave from the ratio between the long and short axes of the ellipse. It is approximately 8 hr for this wave. The gravity wave appears to propagate in the vertical plane that makes an angle of 7° eastward from the north. As

mentioned above, the apparent period of the gravity wave is approximately 13 hr, which is longer than the intrinsic period of 8 hr. The difference between those periods seems to be due to the Doppler effect, which shows that the gravity wave must be propagating against the northward component of the background wind. Although the direction of the background wind changes within the altitude range, the northward components of the vertical linear trends are negative below 74 km in the region where the hodograph shows clear elliptical motion. Assuming that the vertical linear trend of the wind profile represents the background wind velocity, we infer that the gravity wave propagates northward. According to the dispersion equation for gravity waves, the horizontal wavelength is approximately 600 km, and the background wind velocity should be -8 ms^{-1} to produce the Doppler effect of the wave. This southward wind is realized around 72 km at 13 LT.

4.2.2 Short period fluctuations

We have calculated the power spectral density of radial velocities in order to investigate the fine structure of the wind field. Figure 4.3 shows a contour plot of the power spectra in the southward beam. Although the longer period components generally have higher densities than the shorter components, there is one distinct component with an 8–10 min period evident throughout the altitude range. This component is intense at 68–72 km and 74–78 km altitude, and weak around 73 km. Figure 4.4 shows radial wind velocities in the same beam direction. Components with periods of 6–16 min are picked out by means of a numerical band pass filter. In the altitude regions lower than 72 km and higher than 74 km, fluctuations are intense, and the maximum amplitude of the fluctuation is approximately 5 ms^{-1}. The phases of the fluctuations are almost constant with height above and below 73 km, and the amplitude seems to be the smallest at 73 km. We also note that there is a sudden phase reversal at the altitude of the smallest amplitude. In Fig. 4.5, we compare the radial wind velocities at altitudes the same distance above and below 73 km. The signs of one of the radial wind velocities is reversed, and the positive values shown for the data obtained above and below 73 km correspond to approaching and receding velocities, respectively. The radial wind velocities at the two altitude ranges seem to be not only phase reversed, but also show very similar time variations with each other. This is especially clear when the amplitude becomes large.

Rastogi and Bowhill [1976] and Fukao *et al.* [1979] observed radial wind fluctuations in the mesosphere with periods of 10–15 min and amplitudes of less than 2 ms^{-1}. They explained these oscillations in terms of evanescent sur-

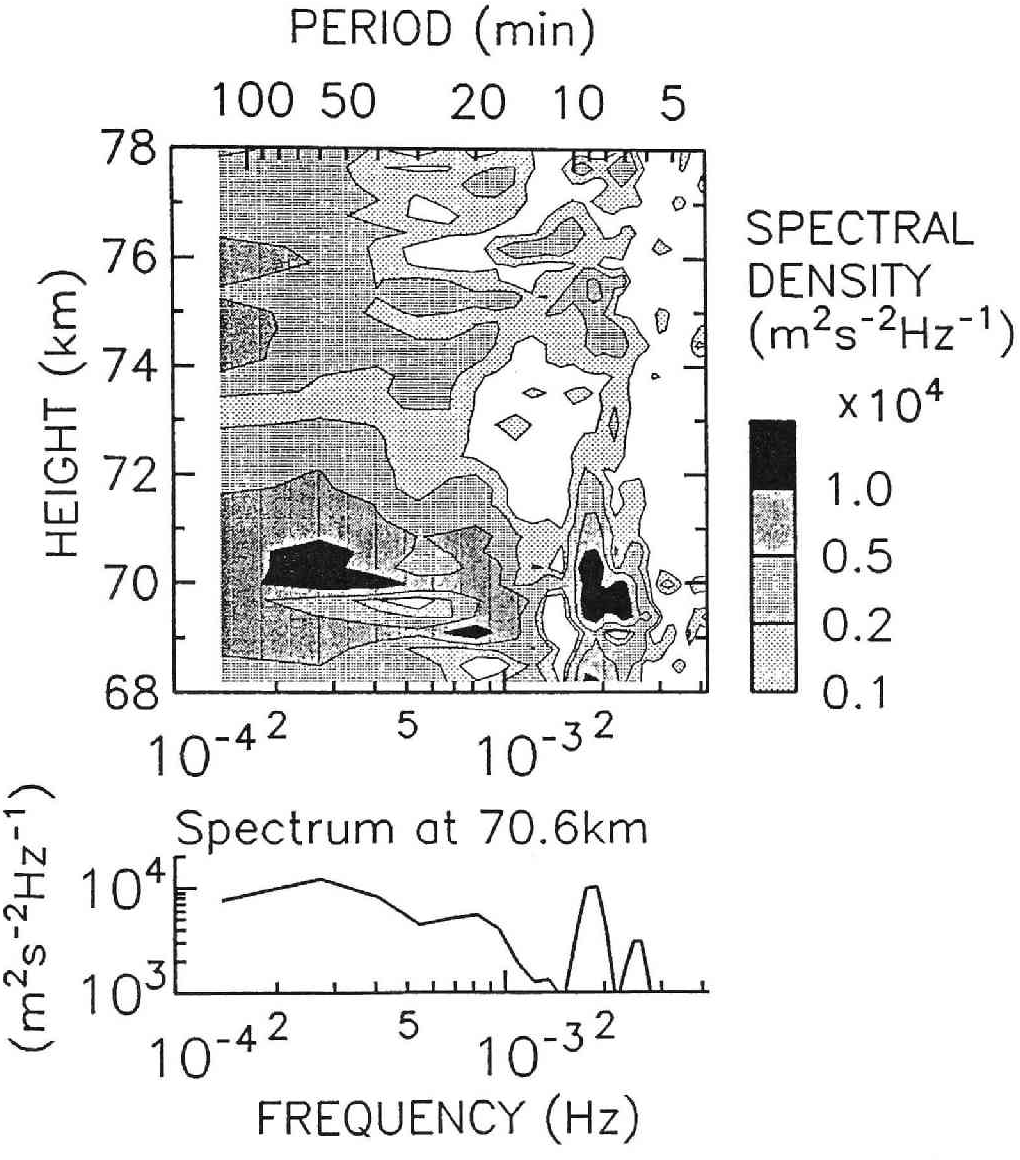

Figure 4.3: The top panel shows the height distribution of power spectral densities of radial wind fluctuations observed during 10–16 LT in the southward beam on 8 February 1985. The bottom panel shows the power spectrum obtained at 70.6 km.

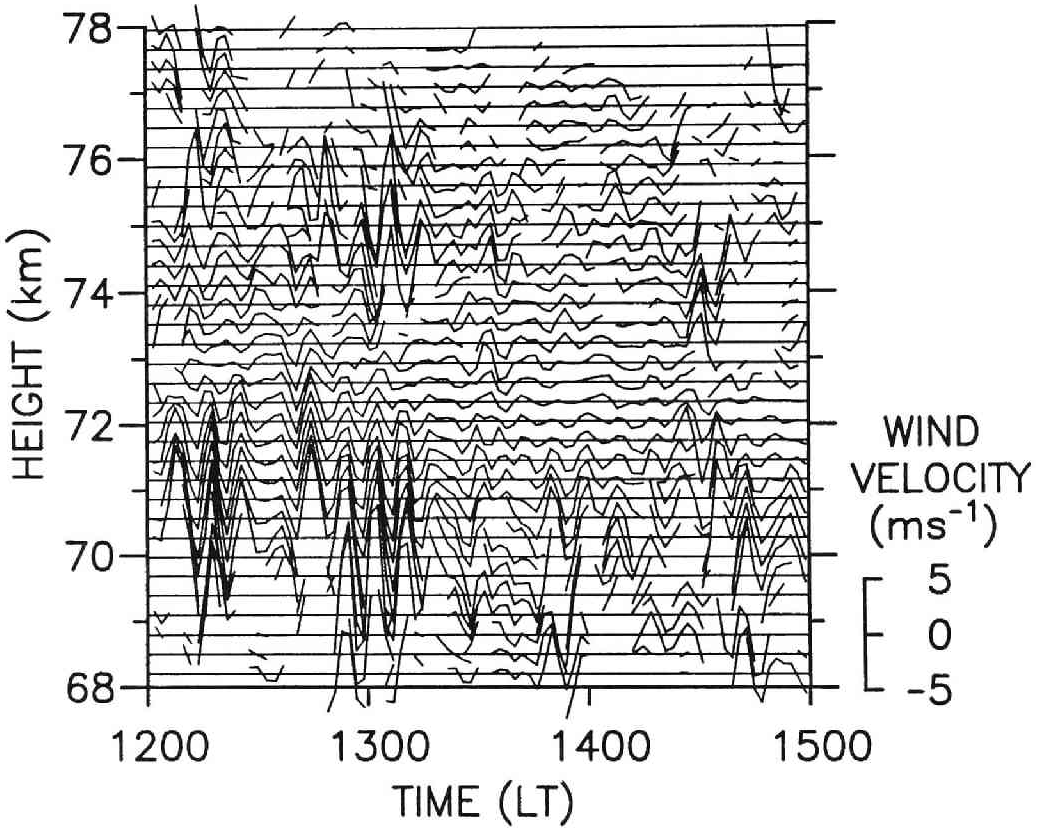

Figure 4.4: Radial wind fluctuations with periods ranging from 6 to 16 min observed in the southward beam on 8 February 1985.

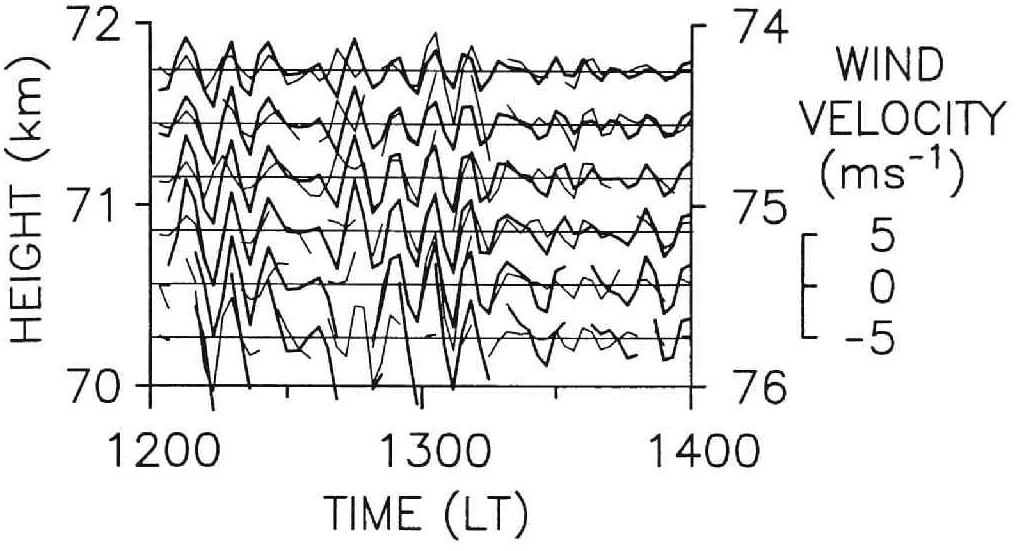

Figure 4.5: Radial wind variations at altitudes the same distances above and below the phase reversal height (73 km), with the sign of one reversed. Thick lines show the variations below 73 km with receding positive, and thin lines show that above 73 km with approaching positive. The left and right vertical axes show the altitudes below and above 73 km, respectively.

face waves with periods near the Brunt-Väisälä frequency. The fluctuations shown in Fig. 4.4, on the other hand, have a clear phase reversal near 73 km, which was not observed in the oscillations mentioned above. Furthermore, the symmetrical nature of the fluctuations above and below 73 km strongly suggests that they belong to one system of instabilities which covers the altitude range of 68–78 km.

Figure 4.6 illustrates the r.m.s. speeds of the radial wind fluctuations averaged in two altitude regions, i.e., 70–72 and 74–76 km. The r.m.s. speed in the lower region is larger than that in the upper region, and the maximum values seem to be approximately 3 and 2 ms^{-1} in the lower and upper regions, respectively. They show a similar variation and simultaneously become large for approximately 20 min. We recognize four events of large fluctuations, the first three of which occur periodically during 1205–1320 LT.

In order to investigate the amplitude and the phase of these fluctuations, we assumed a sinusoidal oscillation with a period of 9 min and fit it to the radial wind velocities for each event by using the least squares fitting method. Figure 4.7 shows the amplitudes and phases of the fluctuations for the four events. The origin of phase is arbitrary. Considering that the estimation error

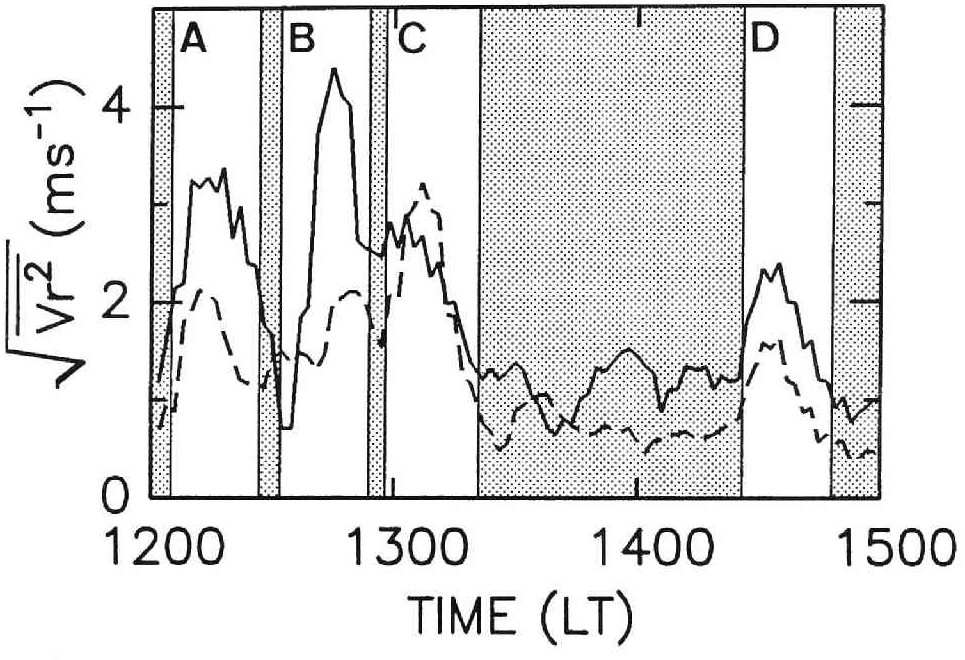

Figure 4.6: Variation of r.m.s. speed of the radial wind fluctuations V_r in Fig. 4.4 averaged in the altitude range of 70–72 km (bold line) and 74–76 km (dashed line). A, B, C and D show events of large fluctuations which occur during 1205–1227, 1232–1254, 1258–1321 and 1424–1446 LT, respectively.

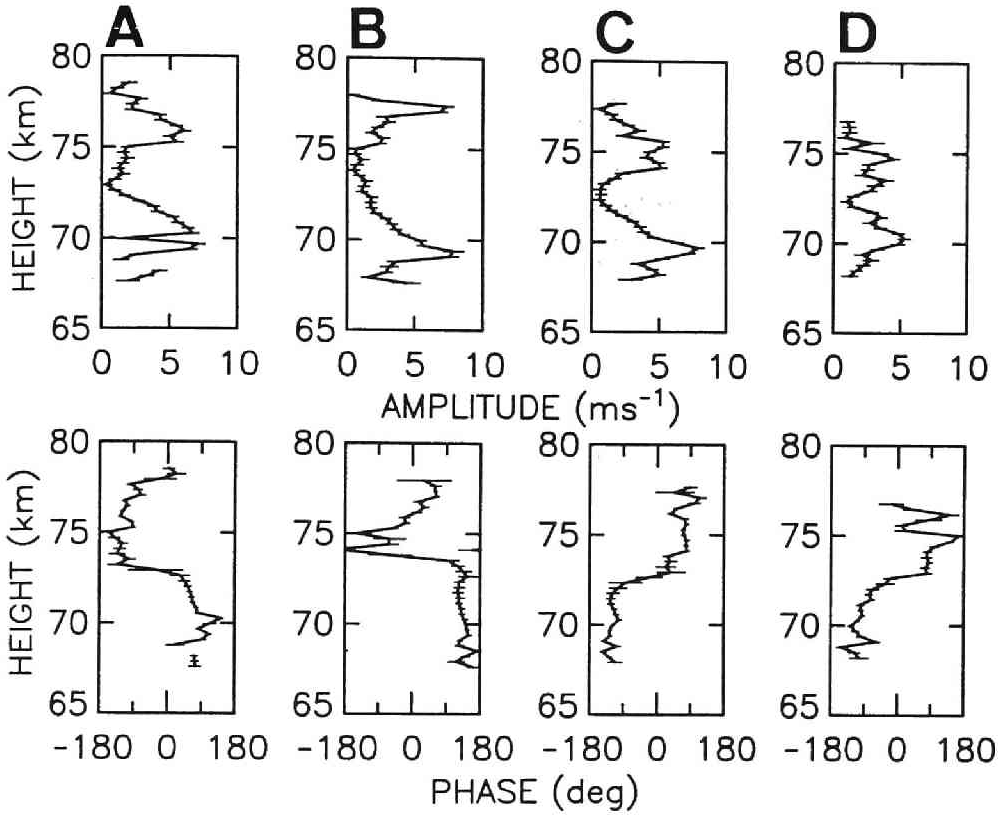

Figure 4.7: Amplitude (top) and phase (bottom) profiles of radial wind fluctuations obtained in each event shown in Fig. 4.6. Radial wind velocities are fitted by assuming a sinusoidal oscillation with a period of 9 min. Error bars on the profile indicate the standard deviation of the estimated amplitudes and phases.

of the phase is approximately $\pm 20°$, it is clear that in each event the phase jumps almost 180° within one or two range gates (i.e. 300–600 m) near the altitude where the minimum amplitude occurs. The maximum amplitudes are larger than 5 ms^{-1} and occur at altitudes 3 or 4 km below and above the phase reversal height. The error in the amplitudes is less than ± 1 ms^{-1}. These similarities imply that instabilities of the same kind occur intermittently at slightly different altitudes. In the troposphere, VanZandt *et al.* [1979] and Klostermeyer and Rüster [1980] have observed radial wind oscillations with periods of 4 to 8 min, and phase jumps of approximately 180° and 100°, respectively. Although the vertical scale and phase variation of our mesospheric fluctuations are slightly larger than those observed in the troposphere, the be-

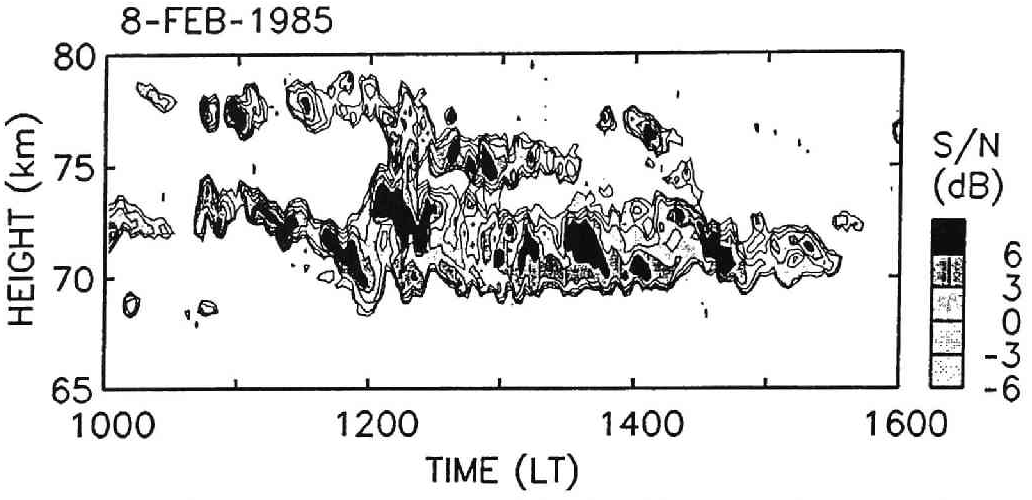

Figure 4.8: Time-height sections of the signal-to-noise ratio observed in the southward beam on 8 February 1985.

havior seems to be very similar. The Richardson number will be discussed in the later section by taking into account the potential temperature fluctuation due to the inertia gravity wave.

4.2.3 Echo power and spectral width

Figure 4.8 shows a time-height section of the signal-to-noise ratio during the observation. Intense scattering layers are shown at 68–80 km; a thin layer at 72 km during 11–12 LT seems to be enhanced around 12 LT and generate a large scattering region during 12–16 LT. This turbulent layer consists of many isolated intense patches with thicknesses of 1–2 km and periods of occurrence of several tens of minutes. Most of them seem to move downward. Wave-like structures are shown in the turbulent layers; they are clear during 1400–1530 LT at 70–73 km with a period of approximately 1 hr. Within the wave-like structure at 70-73 km around 1415 and 1515 LT, we recognize structures like a cat's-eye pattern; the small regions with relatively weak echo power which are surrounded by intense scattering layers.

Figure 4.9 shows profiles of echo power and spectral width (converted to the half-power full width in the unit of ms^{-1}) averaged over 1230–1330 LT. The echo power is enhanced at both 70–72 and 75–76 km altitudes. Peaks of the echo power near 70 and 75 km agree with those of the amplitude of the radial wind fluctuation shown in Fig. 4.7. It is noted that, at 72–73 km where the amplitude of the wind fluctuation is the smallest, the echo power is

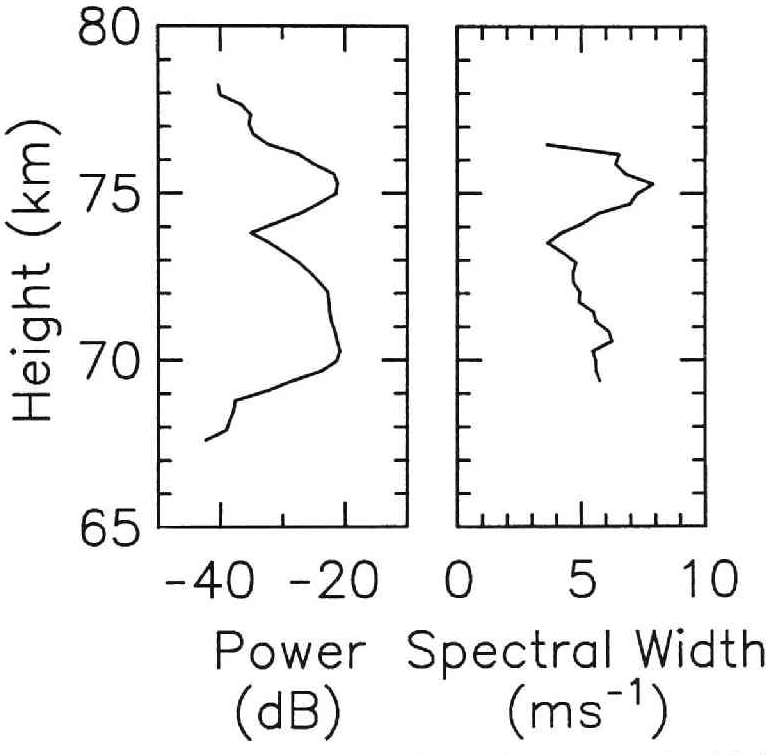

Figure 4.9: Profiles of echo power (left panel) and spectral width (right panel) averaged over 1230–1330 LT on the same day. Note that the spectral width is a half-power full width.

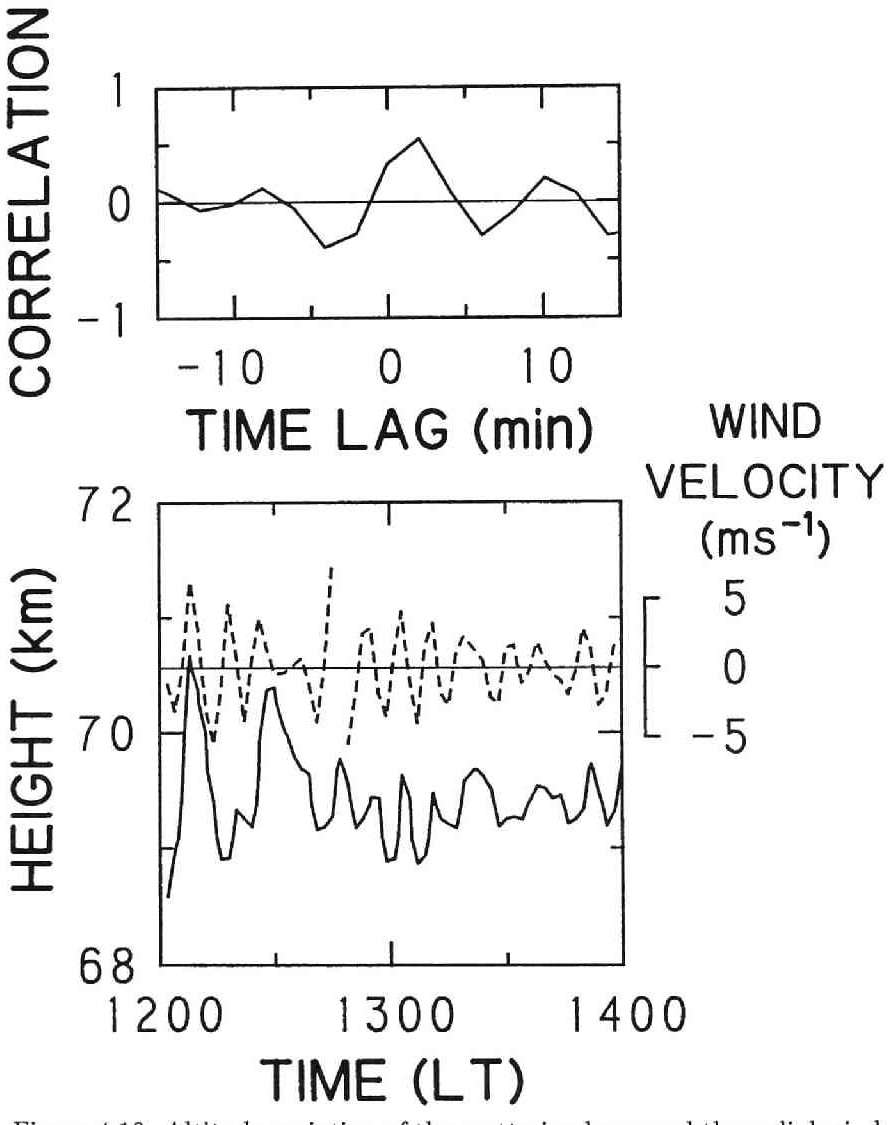

Figure 4.10: Altitude variation of the scattering layer and the radial wind velocities in the southward beam (bottom). The solid line shows the variation of altitude of the constant signal-to-noise ratio contour (−3 dB) around 69.5 km shown in Fig. 4.8. The broken line shows the variation of the radial wind velocity at 70.6 km. Top panel shows cross-correlation coefficient between the altitude variation and the radial velocity shown in the bottom panel. Positive lag shows that the altitude variation lags relative to the radial velocities.

still large and there seem to be large fluctuations in the echo power structure as shown in Fig. 4.8. The minimum echo power appears at a slightly higher altitude than the phase reversal. The spectral width is large at the altitudes where the echo power is large and has a minimum of approximately 4 ms^{-1} at altitudes slightly below 74 km. The peak of 8 ms^{-1} around 75 km is larger than that around 71 km. We also find that time-height distribution of the spectral width is similar to that of the echo power. This implies that the echo power enhancement is not due to the specular reflection, but to turbulence scatter.

As shown in Fig. 4.8, the lower edge of the turbulent layer around 70 km moves up and down. Figure 4.10 displays the altitude at which the signal-to-noise ratio is -3 dB, together with the southward radial wind velocity variation at 70.6 km. The fluctuation of the altitude is a measure of the displacement of the lower edge of the turbulent layer. A similar variation of the radial wind velocities between 12 and 14 LT is also recognized. A cross-correlation between these fluctuations shows that the altitude fluctuation of the turbulent layer lags the radial wind fluctuation by approximately 2 min. Because the period of the fluctuation is 9 min, the altitude of the lower edge seems to lag approximately 90° relative to the radial velocity. With an amplitude of the radial wind fluctuation of about 4 ms^{-1}, the vertical displacement is estimated to be 340 m, which is consistent with the amplitude of the altitude fluctuation at around 13 LT.

4.3 Stability of the atmosphere in the presence of gravity waves

As shown in Fig. 4.1, the shear of the wind velocity is mainly due to the inertia gravity waves which are superposed on the background wind. In order to calculate the Richardson number profile, we have to take into account the fluctuation of potential temperature induced by the inertia gravity wave as well as the wind shear [Hodges, 1967]. Tsuda *et al.* [1985b] have reported the importance of the modification of the Richardson number profiles including both wind and temperature fluctuations due to low-frequency gravity waves.

The Richardson number Ri in the presence of gravity waves are presented by Eq. (1.38). We have calculated Ri of the wind profile averaged over 1230–1330 LT assuming the wind to be a superposition of the linear trend and the inertia gravity wave which propagates toward the north. Parameters of the calculation are shown in Table 4.2, where the wave amplitude is assumed to be constant with altitude, and the background temperature is taken from the CIRA 1972 model. The calculated wind velocity and shear profiles are

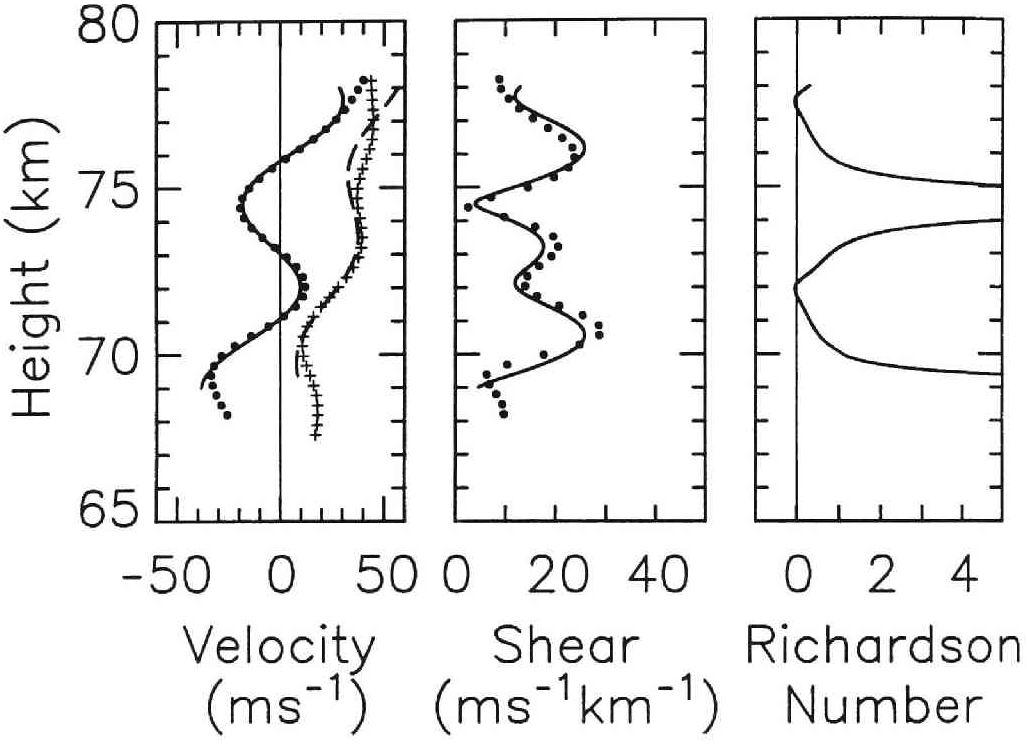

Figure 4.11: Vertical profiles of wind fields (left panel), wind shear (center panel) and the Richardson number (right panel). All lines correspond to the calculated profiles obtained by using the simplified wind model shown in Table 4.2. In the left panel, solid and dashed lines correspond to the northward and eastward components of the wind model, and dots and cross symbols correspond to the northward and eastward wind velocities observed during 1230–1330 LT on 8 February 1985, respectively. Dots in the center panel correspond to the intensity of vector wind shear of the observed wind velocity.

Observation period	8 February 1985
Inertia gravity waves	
Intrinsic period (hr)	8.0
Vertical wavelength (km)	5.6
Propagation direction	7° east from the north
Amplitude* (ms^{-1})	19.0
Mean background wind	
Northward wind	
shear ($ms^{-1}km^{-1}$)	3.7
velocity (ms^{-1}) at 70 km	−14.0
Eastward wind	
shear ($ms^{-1}km^{-1}$)	4.4
velocity (ms^{-1}) at 70 km	13.0

* Maximum wind velocity along the long-axis of the ellipse

Table 4.2: Parameters for the Richardson number calculation for the gravity wave observed on 8 February 1985.

shown in Fig. 4.11. Symbols correspond to the observed values in this figure. The calculated and observed profiles agree well especially between 70 and 75 km. The minimum Richardson number is slightly negative around 72 km; this altitude is different from that of the wind shear maxima at 73.2 and 70.5 km because of the potential temperature fluctuation due to the gravity wave. The other minimum of the Richardson number is shown at 77.5 km, but this does not seem to be reliable because it occurs near the edge of the region of the model calculation. When there is no gravity wave, the Richardson number due only to the background linear trend is 5 or 6. As shown in Fig. 4.12, the altitude of the minimum Richardson number is robust and varies less than 200 m as the amplitude or the vertical wavelength of the gravity wave changes up to ±10%. The altitude of the minimum Richardson number is even less sensitive to changes in other parameters. The minimum Richardson number changes sign as the amplitude and the vertical wavelength are varied.

As mentioned above, the wind profile is well described by the single monochromatic inertia gravity wave, the amplitude of which does not increase with altitude. Also the minimum Richardson number is smaller than the critical value for the onset of shear and convective instabilities. This suggests that the inertia gravity wave is saturated and dissipating its energy. The minimum

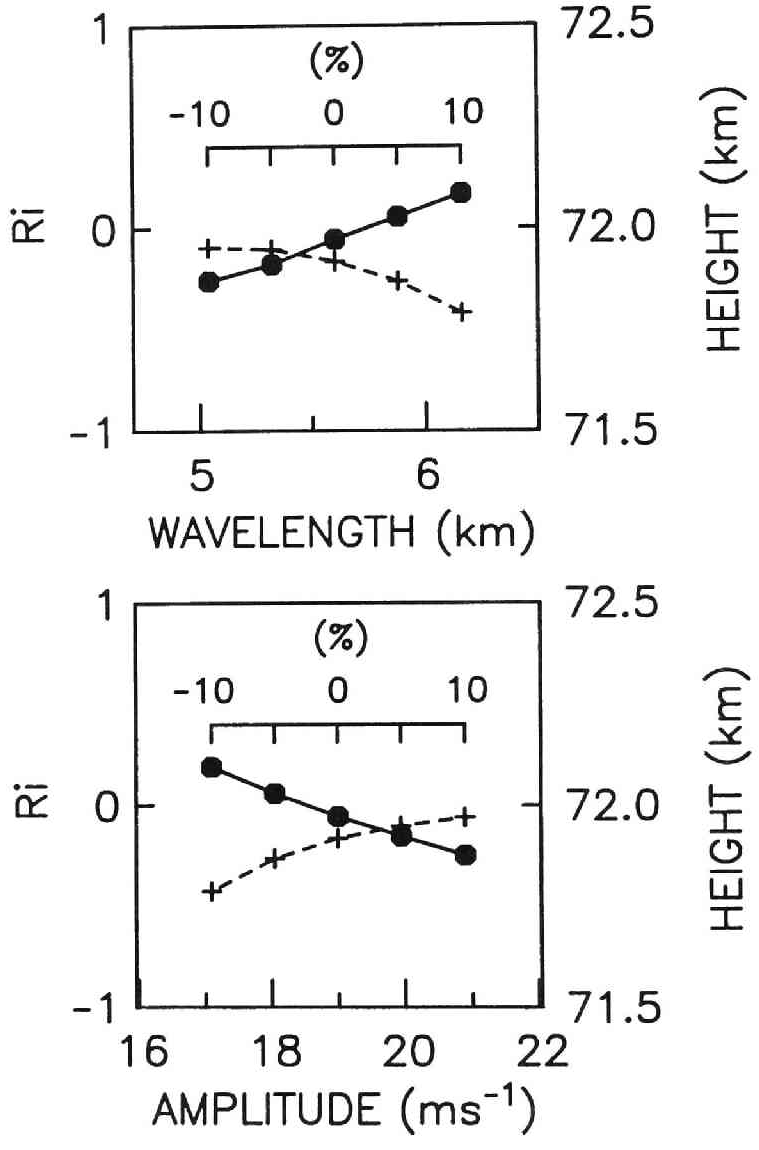

Figure 4.12: Variation of the minimum Richardson number (solid line) and its altitude (dashed line) versus parameters of the gravity wave model shown in Table 4.2. Top and bottom panels correspond to the variations obtained by changing the vertical wavelength and the amplitude of the model up to $\pm 10\%$, respectively; other parameters are not changed in each case. The symbols at the center of the horizontal axes correspond to the minimum Richardson number shown in Fig. 4.11.

value of the Richardson number at 72 km coincides with an enhancement of the echo power in Fig. 4.9. Considering the wave-like structure and small-scale patches in the turbulent layer, the inertia gravity wave seems to induce instabilities that are not observed in the wind velocities, and produce turbulence.

The phase reversals of the radial velocity fluctuations, on the other hand, occur at slightly higher altitudes than that of the minimum Richardson number. At the altitude of the phase reversal, the calculated Richardson number is slightly larger than 1/4 but less than 1, and the wind shear is larger than that at the altitude of the minimum Richardson number. It seems to be possible that the Richardson number at the phase reversal becomes instantaneously less than the critical value of shear or convective instabilities due to the superposition of the smaller scale perturbation. The r.m.s. speed shown in Fig. 4.6 actually shows that the fluctuations occur intermittently. The fluctuation was very similar to that of the Kelvin-Helmholtz instabilities in the troposphere. However, we cannot identify the nature of the fluctuations because the wind field induced by the inertia gravity wave does not produce a parallel stratified shear flow, and instabilities in rotational shear flow have not been studied theoretically. The radial wind fluctuations seem to be due to shear or convective instabilities with the largest vertical scale among those observed as the echo power enhancement. Although another possibility is that the fluctuation is induced by the parametric instability, it seems to be beyond the scope of these observations to determine the mechanism of the fluctuation.

4.4 Turbulence layers related to gravity waves

MST radar observations have revealed that mesospheric turbulence regions are distributed discontinuously in time and space [Harper and Woodman, 1977; Czechowsky *et al.*, 1979]. By SOUSY radar observations with height resolution of 150 m, Röttger *et al.* [1979] have classified various structures of turbulence regions into blobs, sheets and layers although the mechanisms to produce the different structures is not explained. It is also reported that the maximum echo power appears around the altitude of the maximum vertical wind shear [Rüster, 1984; Rüster and Klostermeyer, 1985].

From MU radar observations of the mesosphere, we have frequently found evidence of inertia gravity waves with periods around 10 hr and vertical wavelengths ranging from 4 to 20 km. In this section, we discuss relations between structure of scattering layers and Richardson number profiles modified by inertia gravity waves [Yamamoto *et al.*, 1987a].

4.4.1 A monochromatic inertia gravity wave

Figure 4.13 shows eastward wind profiles observed on 13 February 1986. Each profile is a 2-hr average determined every hour at each altitude accompanied with a background linear trend averaged over 8–16 LT. The smoothed wind profiles are obtained by removing fluctuations with vertical wavelengths smaller than 6 km by a low-pass filter. A wave-like structure with a vertical wavelength of approximately 18 km is recognized in the filtered wind profile, which suggests a manifestation of an inertia gravity wave. A phase line, which is determined by connecting points where the profiles go across the linear trend wind, clearly shows a downward progression of phase. The vertical phase velocity is estimated as 0.6 kmhr^{-1}. Figure 4.13 also shows that intense scattering layers at the 70–75 km altitudes distribute discretely in height with thickness of a few kilometers, and propagate downward. The upper pair of arrows in the echo power contour at 72–77 km altitudes indicates locations of the phase line drawn in the wind profiles. The lower pair of arrows are shifted downward by half of the vertical wavelength of the gravity wave. The progression of the structure of the scattering layers at 70–75 km is almost parallel to the downward propagation of the wind fields. The other intense scattering layer at 63–68 km centered at noon appears around the phase line indicated by the lower pair of the arrows, but does not show clear downward motion.

In order to investigate the polarization of the wave, a wind velocity vector is calculated by averaging the eastward and northward components during 12–14 LT. Figure 4.14 shows a hodograph of the wind vector after subtracting the vertical linear trend of the wind. The tip of the wind vector moves clockwise with increasing height. By removing components with vertical wavelength smaller than 6 km, the wind vector shows an elliptical rotation, although contaminations by smaller scale fluctuations are still recognized. This shows that the wave is an inertia gravity wave propagating upward [Gossard and Hook, 1975]. From the ratio between the long and short axes of the ellipse, the intrinsic period of the wave is estimated to be approximately 9.7 hr. The direction of the long axis shows that the wave seems to propagate horizontally either to the north-west or the south-east. According to the polarization equation of gravity waves of Eq. (1.34), the vertical wind component is almost in-phase with the horizontal component along the propagating direction [Gossard and Hook, 1975]. Unfortunately, the vertical wind velocity in 12–14 LT was not systematic enough to determine the profile. However, the sign of the vertical wind velocities obtained before and after the wind vector determination have suggested that the inertia gravity wave may have propagated to the north-west.

By using the characteristics of the inertia gravity wave in 12–14 LT listed

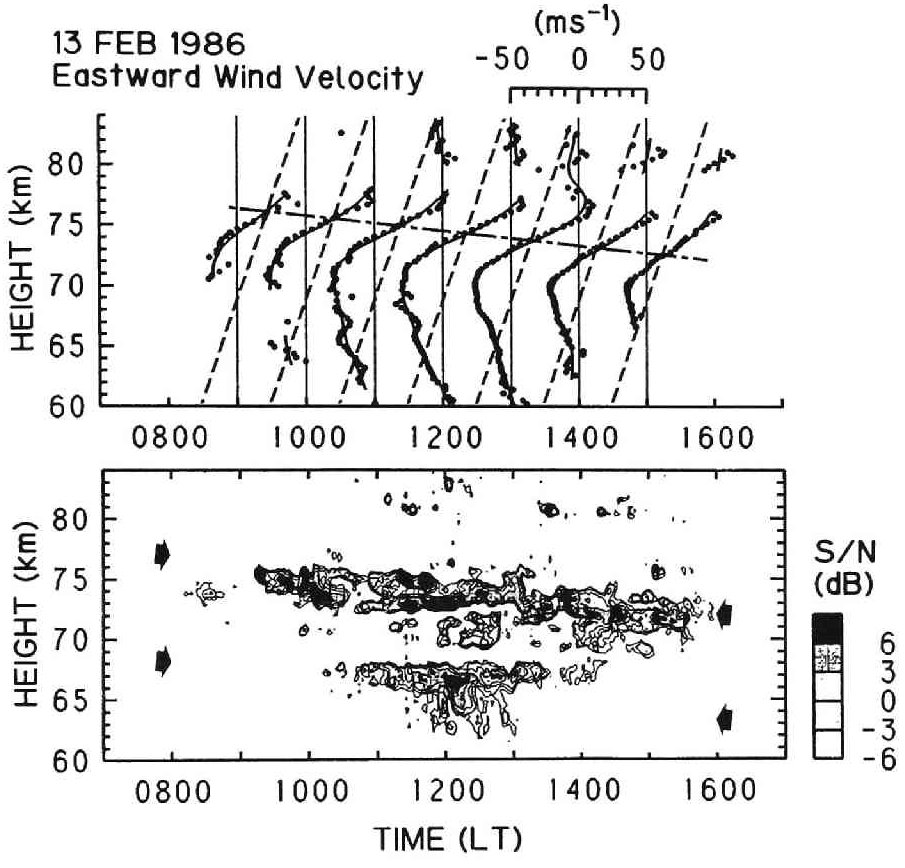

Figure 4.13: Wind profiles (top) and echo power contour (bottom) observed on 13 February 1986. Dots in the top panel show eastward wind profiles each of which is a 2-hr average determined every 1 hr. Dashed lines show a vertical linear trend of the wind profile averaged over the whole observation period. Thick curves denote wind profiles after low-pass filtering with a cutoff vertical wavelength of 6 km. A chained line indicates a phase line connecting points where filtered wind profile go across the linear trend. Two pairs of arrows in the bottom panel correspond to the phase lines with vertical spacing of half of the wavelength of the inertia gravity wave.

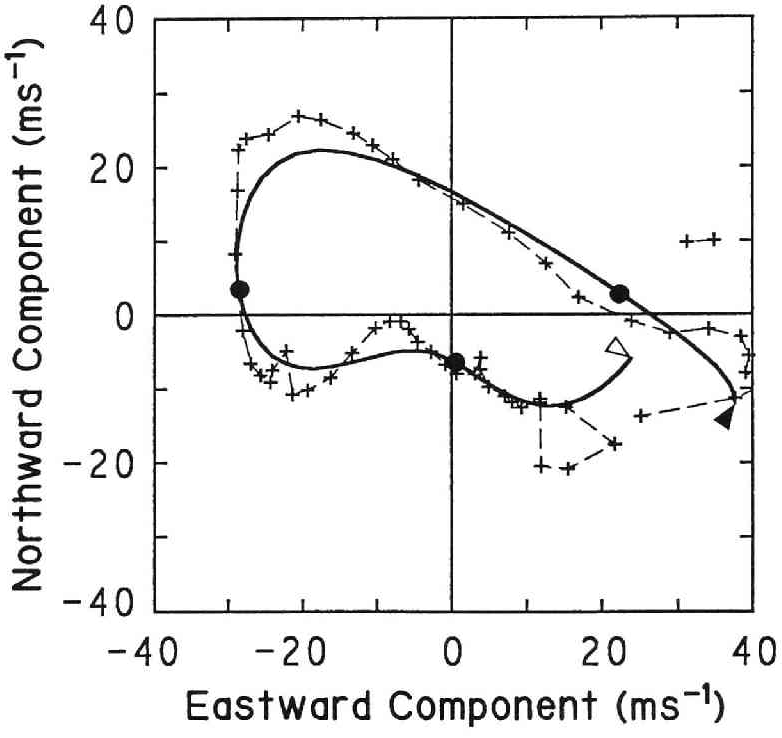

Figure 4.14: A polar plot of the wind fields observed in 12–14 LT on 13 February 1986. Cross symbols show determinations of wind vectors at each altitude. Vertical linear trend of the wind profile is extracted. The smoothed curve is obtained by using the low-pass filter with a cutoff vertical wavelength of 6 km. The open and solid triangles on the solid line indicate the lowest (60.2 km) and highest altitudes (77.5 km). Circular symbols are plotted at 65, 70 and 75 km.

in Table 4.3, a corresponding Richardson number profile is calculated as shown in Fig. 4.15. It has minimum values of 3.2 and 1.8 at 67 and 73 km altitudes, respectively. Note that the altitudes of the minimum Richardson number do not necessarily agree with those of the maximum wind shear. Enhancements in the echo power profile detected at 67 and 73 km altitudes coincide with the minima of the Richardson number profile. Also, the minimum of the echo power profile at 69 km corresponds to the altitude of the local maximum of the Richardson number. A vertical profile of spectral width has peaks at around 65 and 75 km, and a broad minimum of about 0.5 ms^{-1} at around 70 km.

As shown in Fig. 4.15 (a), the wind profile averaged over 2 hr is well described by the model wind field which is a superposition of the monochromatic

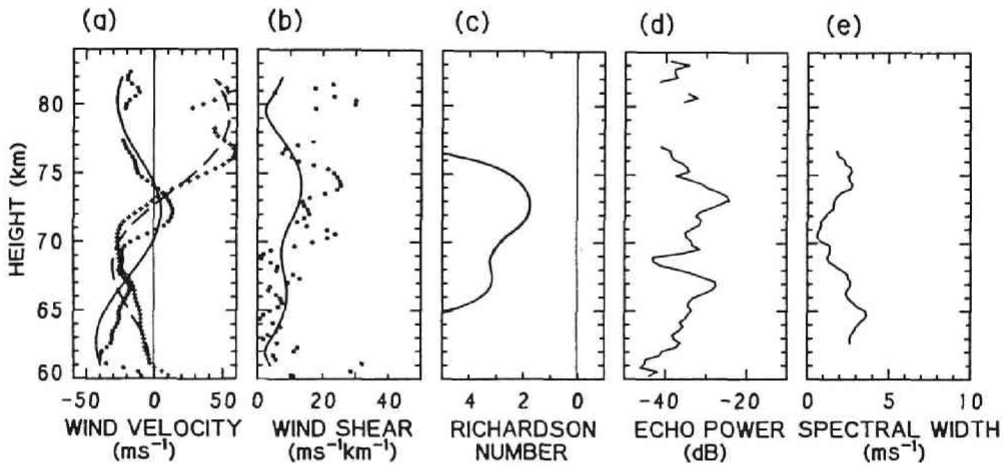

Figure 4.15: Vertical profiles of (a) wind fields, (b) wind shear, (c) Richardson number, (d) echo power and (e) spectral width observed in 12–14 LT on 13 February 1986. Dots and cross symbols in (a) correspond to northward and eastward wind components averaged over 2 hr, respectively. Solid and dashed lines in (a) shows northward and eastward components of the model wind which is obtained by assuming the linear trend and the inertia gravity wave listed in Table 4.3, respectively. Dots in (b) correspond to intensity of vector shear of the observed wind velocities shown in (a), and a solid line to that of the model wind. The Richardson number profile is obtained by using the model wind.

Observation period	13 February 1986	14 February 1986	
Inertia gravity waves		I	II
Intrinsic period (hr)	9.7	8.9	9.0
Vertical wavelength (km)	17.6	12.5	3.0
Propagating direction	58° west from the north	53° west from the north	westward
Amplitude* (ms^{-1})	30.0	29.4	6.0
Mean background wind			
Northward wind			
shear ($ms^{-1}km^{-1}$)	0.9	2.2	
velocity (ms^{-1}) at 70 km	−16.0	−8.0	
Eastward wind			
shear ($ms^{-1}km^{-1}$)	3.3	0.4	
velocity (ms^{-1}) at 70 km	1.0	25.0	

∗ Maximum wind velocity along the long-axis of the ellipse

Table 4.3: Parameters for the Richardson number calculations for gravity waves observed on 13 and 14 February 1986.

inertia gravity wave on the vertical linear trend. The amplitude of the wave does not seem to increase with altitude. This implies that the wave is saturated. However, the minimum value of the Richardson number associated with the wave and mean flow is not small enough to excite either convective or shear instabilities [Fritts and Rastogi, 1985]. It is likely that the inertia gravity wave produces regions with relatively small Richardson number, where it may become smaller than the critical values due to the possible superposition of smaller scale fluctuations, and thus turbulence layers are easily produced.

4.4.2 Superposition of inertia gravity waves

A similar observation to that in 4.4.1 has been made on 14 February 1986. Wind fields shown in Fig. 4.16 indicate an inertia gravity wave with a vertical wavelength and downward phase velocity of 12.5 km and 0.8 $kmhr^{-1}$, respectively. A polar plot of the filtered wind fields is shown in Fig. 4.17. The elliptical motion of the wind vector indicates that the inertia gravity wave has an intrinsic period of 8.9 hr, which is slightly shorter than the inertia gravity wave detected on the previous day. The propagation direction of the wave was determined as in the case shown in 4.4.1, and was in the north-west direc-

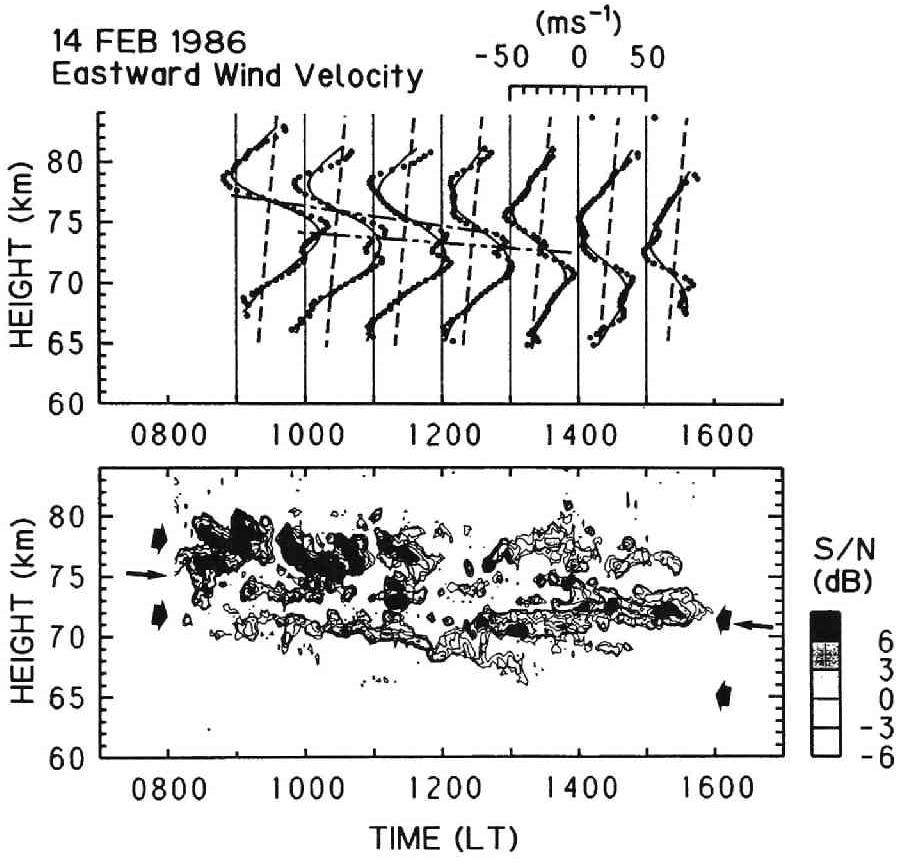

Figure 4.16: The same as Fig. 4.13 except for the observations on 14 February 1986. Two kinds of phase lines with downward phase velocities of 0.8 and 0.4 kmhr^{-1} are indicated as chained and doubly-chained lines (top), and thick and thin arrows (bottom), respectively.

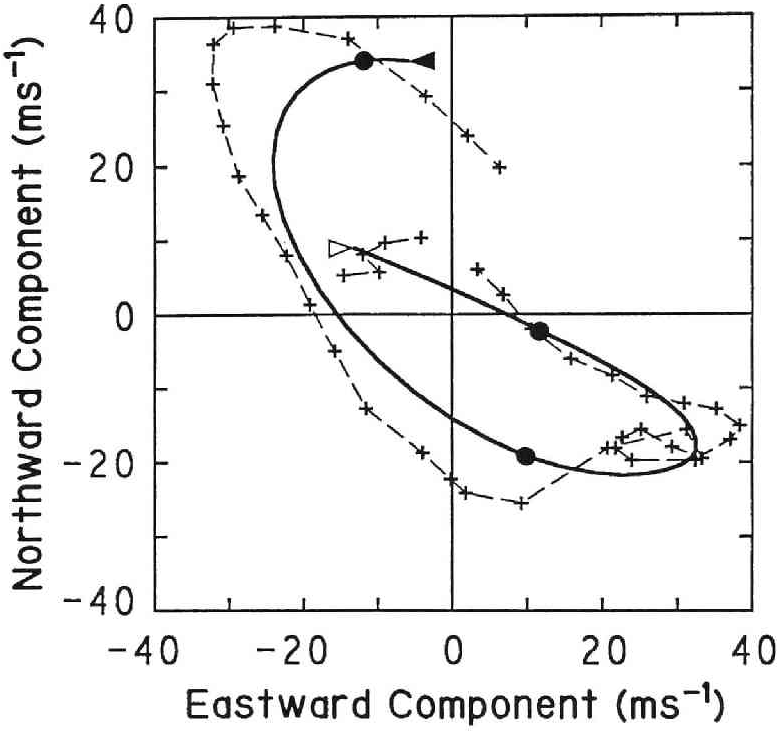

Figure 4.17: The same as Fig. 4.14 except for the observations in 10–11 LT on 14 February 1986. The open and solid triangles on the solid line indicates the lowest (67.6 km) and highest altitudes (80.6 km). Circular symbols are plotted at 70, 75 and 80 km.

tion. This suggests that we have observed the same inertia gravity wave on two consecutive days. However, echo power profiles, also plotted in Fig. 4.16, show a much more complicated structure than in Fig. 4.13. Although the overall structure of intense scattering regions shows downward progression, which seems to agree with the phase line of the inertia gravity wave as indicated by the pair of thick arrows in Fig. 4.16, the scattering region has fine structures with various time-height scales.

In the 70–76 km region of the wind profile without filtering, another wave-like variation is recognized. The vertical wavelength and downward phase velocity of the wave is approximately 3.0 km and 0.4 kmhr^{-1}, respectively. The phase line of this wave is also indicated by the thin arrows in the echo power contour. Thin turbulence layers at 74 km around 10 LT and at 70–72 km in 13–14 LT seem to show a similar descending motion to the phase line indicated by the thin arrows. In Fig. 4.17, the wind vector without filtering

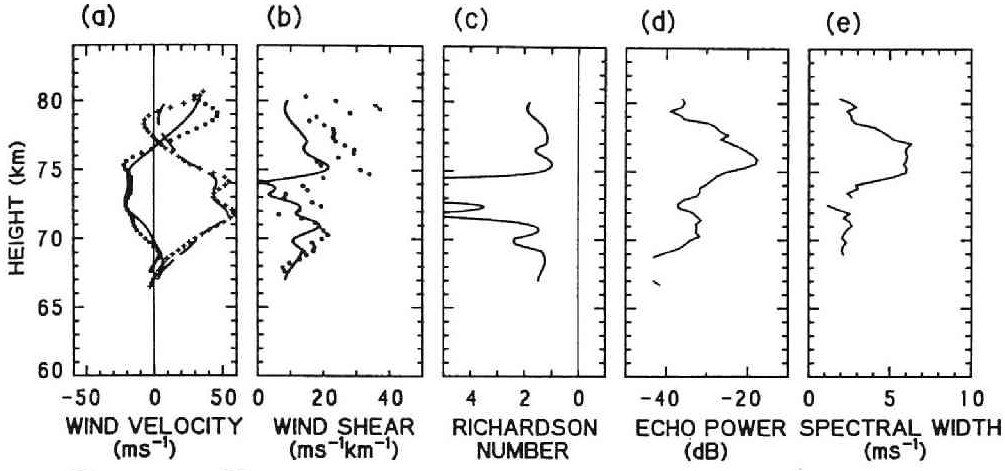

Figure 4.18: The same as Fig. 4.15 except for the observations in 10–11 LT on 14 February 1986.

shows a corresponding elliptical motion[1] superposed on the rotation due to the wave with larger vertical wavelength. The intrinsic period of the wave seems to be approximately 9 hr. Considering the vertical component of the wind, this wave seems to propagate westward.

Figure 4.18 shows the filtered wind profile determined during 10–11 LT and the Richardson number profile calculated by assuming wind fields as a superposition of a linear trend and two gravity waves (I) and (II). As summarized in Table 4.3, we have assumed an inertia gravity wave (I) with vertical wavelength of 12.5 km in the whole altitude range. Another gravity wave (II) with vertical wavelength of 3.0 km is superposed within 69–77 km altitudes in order to approximate fine structure of the wind fields; the amplitude is set to 6 ms^{-1} between 72 and 74 km, and linearly tapered off to 0 ms^{-1} at the 77 and 69 km altitudes. The Richardson number profile has two broad minima of approximately 1.0 in the altitude regions above 75 km and below 71 km, which generally agree with intense peaks of the echo power profile and spectral width. These minima of Richardson number at around 71 and 75 km are attributed to the superposition of the two gravity waves with different vertical wavelengths, and can not be explained by assuming only the larger scale inertia gravity wave. The Richardson number became large at the 73–74 km altitudes where the echo power becomes weak as can be recognized from Fig. 4.18.

Although the echo power profile shown in Fig. 4.18 is complicated, its structure seems to be correlated with the behavior of the gravity waves. It might be appropriate to interpret the structures of the scattering regions observed on

[1]In Fig. 4.17, the structure is found in the dashed line with eastward and northward wind components of 20–30 ms^{-1} and -20 ms^{-1}, respectively. The wind vector also rotates clockwise with increasing height in this region.

14 February 1986 as a superposition of many layers each of which progressed downward following various motions of gravity waves. That is, a mechanism to generate the scattering layer would be the same as that in 4.4.1, but superposition of various gravity waves made the structure of scattering layers complicated.

4.5 Horizontal structure of turbulence layers

The advantage of the MU radar over conventional MST radars is that the MU radar can steer its beam every IPP so that it can observe several areas which are spatially separated from each other almost simultaneously. This capability enables us to investigate small scale structure in the turbulence and wind fields.

Horizontal motions of echo power bursts in the mesosphere were observed by Klostermeyer and Rüster [1984] by calculating the cross-correlation functions between echo power observed in beams pointing in the different directions, although they did not consider the random changes of the scattering pattern in time. Full-correlation analysis is a technique to observe the structure and motion of horizontal patterns by taking the spatial correlation into account [Briggs, 1984]. This technique is utilized with both MF partial reflection and VHF radar observations in order to obtain horizontal wind velocities from the fading patterns detected by three spatially separated receivers.

In this section, this analysis technique is applied to the observations on 8 February 1985 in order to observe horizontal structures of the scattering layers and generation of turbulence by the saturated gravity wave.

4.5.1 Full-correlation analysis

Because the observations on 8 February 1985 were carried by using four oblique beams with a zenith angle of 10°, we could observe the echo power at four spatially separated positions. Figure 4.19 schematically shows the assignment of the four oblique beams and the horizontal pattern of the echo power in the mesosphere that moves with velocity V. We assume that the pattern of echo power $f(x, y, t)$ is a function of position (x, y) and time t, where x and y-axes correspond to the eastward and northward directions, respectively. The spatial and time scales of the horizontal pattern is described by the three dimensional correlation function

$$\rho(\xi, \eta, \tau) = \frac{< f(x, y, t) f(x + \xi, y + \eta, t + \tau) >}{< [f(x, y, t)]^2 >} \tag{4.1}$$

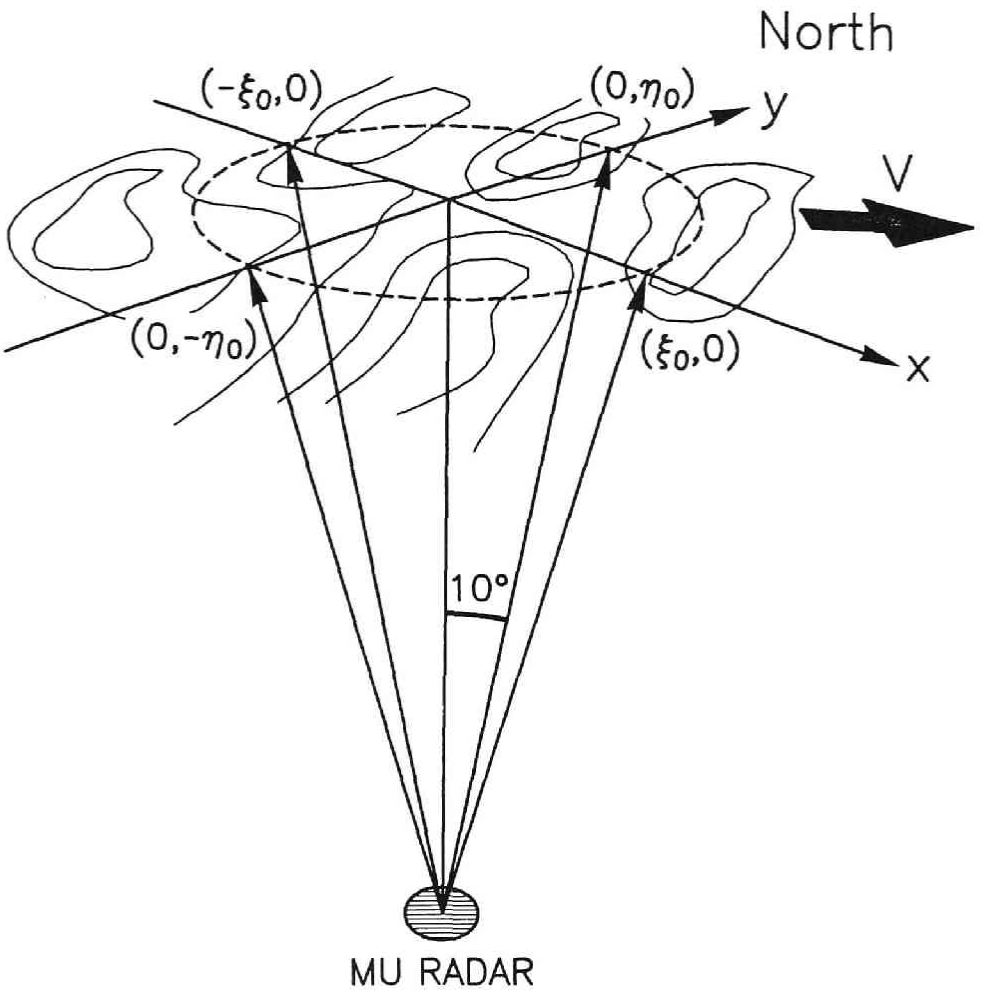

Figure 4.19: Beam assignment used in the MU radar observations on 8 February 1985 together with a schematic diagram of scattering pattern which moves horizontally with velocity V, where x and y-axes correspond to the eastward and northward directions, respectively.

where <> denotes an average, τ is the time lag and ξ and η are spatial lags along the x and y-axes, respectively. The correlation function can be approximated by a family of concentric ellipsoids with the center at the origin [Briggs, 1984]. We therefore write

$$\rho(\xi, \eta, \tau) = \rho(A\xi^2 + B\eta^2 + C\tau^2 + 2F\xi\eta + 2G\eta\tau + 2H\xi\eta) \tag{4.2}$$

where A, B, C, F, G and H are constants. Here, we assume that the correlation function is described by an exponential function as follows:

$$\rho(\xi, \eta, \tau) = \exp[-(A\xi^2 + B\eta^2 + C\tau^2 + 2F\xi\eta + 2G\eta\tau + 2H\xi\eta)] \tag{4.3}$$

Because we observe echo power in the four beams, the cross-correlation functions between echo power observed in different beams can be described by $\rho(\xi, \eta, \tau)$; e.g., the cross-correlation function between the echo power observed in the northward beam $(0, \eta_0)$ and the eastward beam $(\xi_0, 0)$ corresponds to $\rho(\xi_0, -\eta_0, \tau)$. In order to determine the parameters of Eq. (4.3), we have utilized a least squares fitting technique to the cross-correlation function between the echo power in the four beams. An example of the cross-correlation functions is shown in Fig. 4.20, which corresponds to the scattering pattern observed in 10–16 LT at 71.4 km. In this figure, we chose three cross-correlation functions of the echo power observed in the beams pointing the eastward, southward and westward, although we used the cross-correlation functions with all of the combinations among the four beams in order to determine the parameters in Eq. (4.3). The auto-correlation function used is an average of those calculated in the four beams. The solid curves show the fitted correlation functions. We cannot apply the fit to the negative correlation coefficients because of Eq. (4.3), but the fitted curves seem to be close to the observed values for positive correlation coefficients.

When we obtain the parameters, the horizontal velocity of the scattering echo pattern is calculated as a 'tilt' of one axis of the ellipsoids relative to the τ-axis. The x and y components of V are V_x and V_y, respectively, and are given by

$$\begin{aligned} AV_x + HV_y &= -F \\ HV_x + BV_y &= -G \end{aligned} \tag{4.4}$$

[Briggs, 1984]. The motion of the scattering pattern shown in Fig. 4.20 has been estimated to be $V_x = 9.6$ ms^{-1} and $V_y = 27.5$ ms^{-1}. In order to find a spatial scale for the scattering pattern, the particular ellipse for which $\rho = 0.5$ may be defined as the 'characteristic ellipse', which is described by

$$A\xi^2 + B\eta^2 + 2H\xi\eta = C\tau_{0.5}^2 \tag{4.5}$$

where $\tau_{0.5}$ is a time lag at which the auto-correlation function is equal to 0.5, i.e. $\rho(0, 0, \tau_{0.5}) = 0.5$ [Briggs, 1984].

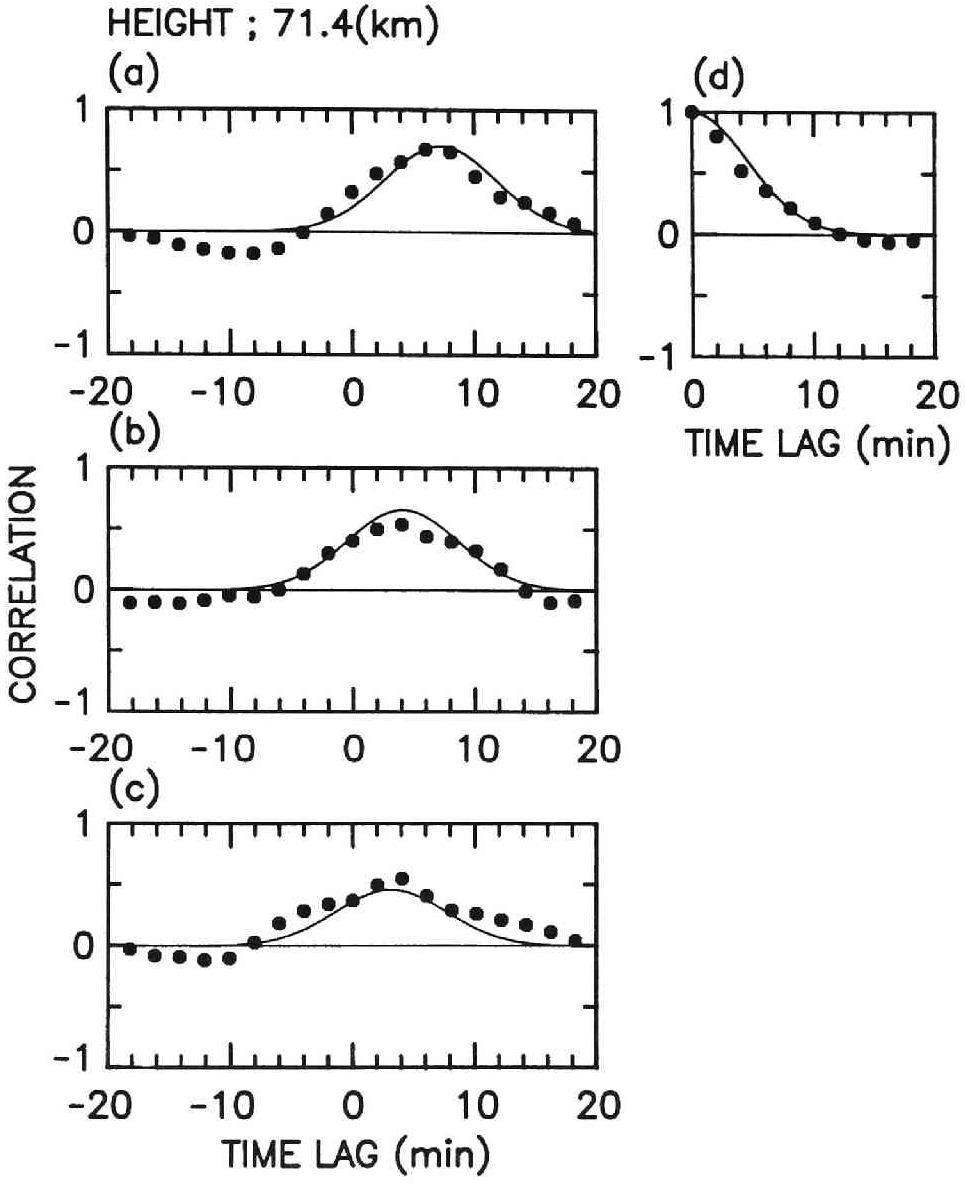

Figure 4.20: Cross-correlation functions between echo power observed in (a) the southward and eastward, (b) the southward and westward and (c) westward and eastward beams. Panel (d) shows the average auto-correlation function of all the beams. The solid line in each panel corresponds to $\rho(\xi, \eta, \tau)$ obtained by the least squares fitting method.

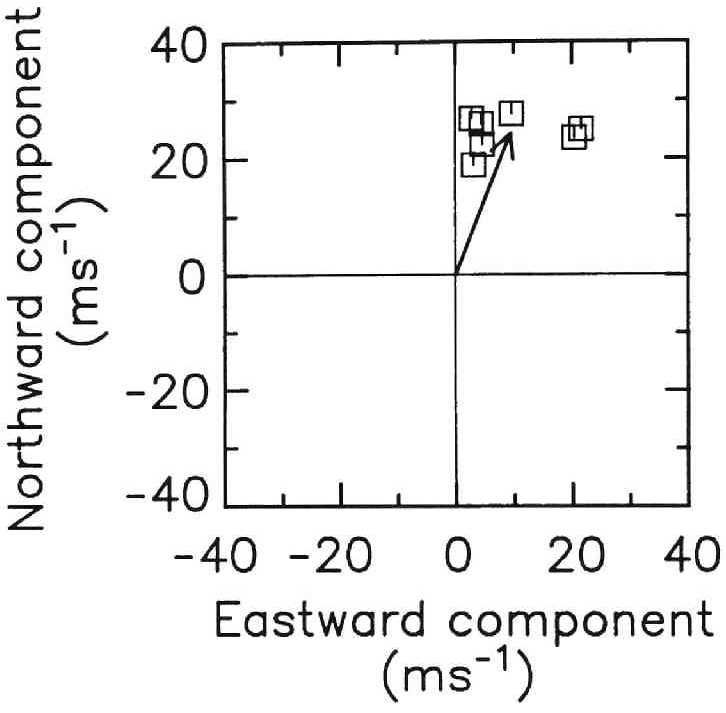

Figure 4.21: Horizontal motion of scattering pattern observed at 10–16 LT in the altitude region of 69–72 km. An arrow shows the averaged velocity.

4.5.2 Observational results

By using the data observed in 10–16 LT, we have calculated the motion of the scattering pattern. Figure 4.21 shows the result obtained in 69-72 km. All of the data are distributed in the region with positive V_x and V_y and show that the fluctuation patterns in this altitude range move toward the north-northeast. The average of the horizontal velocities, which is shown by an arrow, is $V_x = 9.5$ ms^{-1} and $V_y = 24.2$ ms^{-1}.

The characteristic ellipses of the scattering pattern are shown in Fig. 4.22. The size and the direction of these ellipses are similar to each other. The long axis of these ellipses seem to lie in the east-west direction, which is almost perpendicular to V. The length of the long and short axes of the characteristic ellipse, which show the spatial scale of the scattering pattern, are approximately 50 and 20 km, respectively. Because we can determine the three dimensional correlation function for the scattering patterns, we can obtain a correlation time of the structure along the motion of the fluctuation pattern. As shown in Fig. 4.23, they are approximately 700 s at all altitudes.

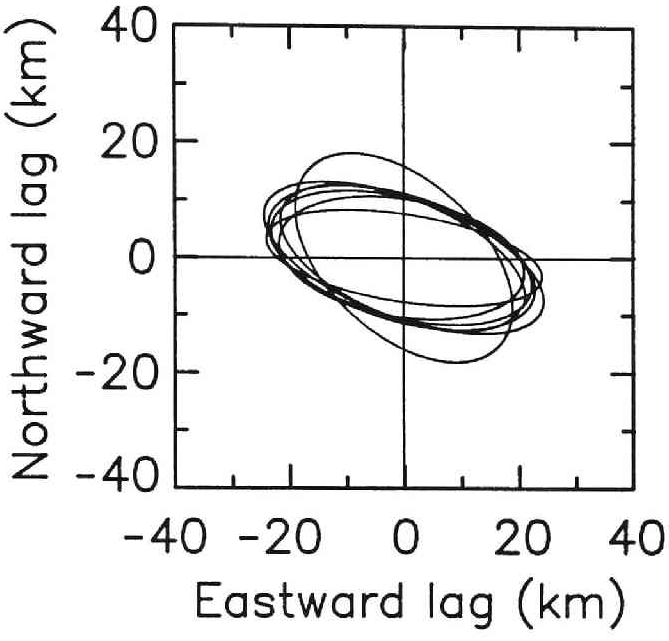

Figure 4.22: The characteristic ellipse of the scattering pattern observed at 10–16 LT in the altitude region of 69–72 km.

Because (V_x, V_y) is an average over 6 hr, we should compare the motion of the scattering pattern with the vertical trend of the wind profile. The vertical trend in Fig. 4.1 shows a wind toward the east or the southeast around 70 km although the scattering pattern moves to the north-northeast. However, the direction of the motion of the fluctuation pattern seems to be well associated with the horizontal propagation direction of the inertia gravity wave. Because, as shown in Section 4.2, the inertia gravity wave propagates northward at approximately 20 ms^{-1}, the wavefront of the gravity wave moves toward the northeast in the strong eastward wind.

For turbulence in the inertial subrange, the energy dissipation rate per unit mass and time is

$$\varepsilon = \alpha^{-2/3}\sigma^3 k_0 \tag{4.6}$$

where α is the Kolmogoroff's constant of about 1.6, σ and k_0 are the width of the echo power spectrum and the wavenumber associated with the largest vortex in the turbulence layer, respectively [Lilly *et al.*, 1974]. k_0 can be approximated as $k_0 = \omega_B/\sigma$, where ω_B is the Brunt-Väisälä frequency [Sato, 1981]. Assuming the turbulence energy per unit mass $E \sim \sigma^2$ and $\omega_B \approx$

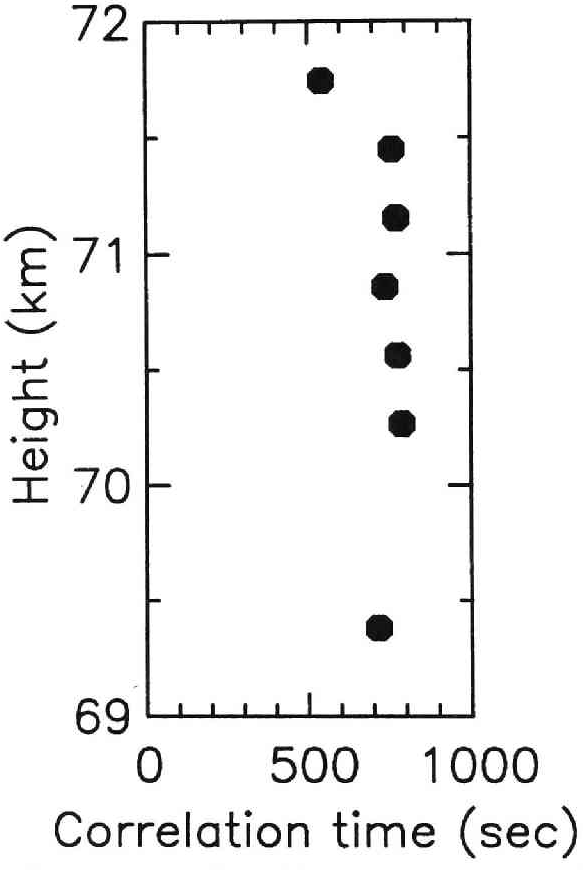

Figure 4.23: The correlation time of the scattering pattern along the horizontal motion observed at 10–16 LT in the altitude region of 69–72 km.

2×10^{-2} s, the lifetime of the dissipating turbulence is estimated as

$$\tau_{turb} = \frac{E}{\varepsilon} \approx \frac{2}{\omega_B} \sim 100(\mathrm{s}) \tag{4.7}$$

This value is much smaller than the time scale of the scattering pattern shown in Fig. 4.23.

Röttger and Ierkic [1985] have observed horizontal trajectories of turbulence blobs in the mesosphere. The motions were detected by using the interferometer technique within 3–4 km of the echoing region of the vertical beam. The blobs showed the horizontal motions in the same direction of the background wind determined by the Doppler shift. It seems to be because the analysis technique was equivalent to the spaced antenna drift and Doppler shift measurements, and the interferometer technique traced the motion of the isolated turbulence itself. In our analysis, on the other hand, the distance between echoing regions of eastward and northward beams was approximately 17 km at altitude of 70 km. Considering the large correlation time of the scattering pattern, the motion we observed is not the one of isolated turbulence detectable within a transmitting beam, but the motion of the region where turbulence are being generated. Another filtering effect may arise because we used the echo power averaged in the echoing region, while Röttger and Ierkic [1985] could detect the micro-structures inside the beam.

Klostermeyer and Rüster [1984] have observed the horizontal motion of the scattering pattern by using a simple correlation technique, and mentioned that the motion was identical to the background wind velocity. Because of their actual zenith angle of 6°, the distance between vertical and eastward beams was 8.4 km at the altitude of 80 km. It is not sure if the motion of the isolated turbulence was detectable with the grid of this size. It is possible that the trace velocities represented the same motion as that of our analysis. In our case, however, we observed a inertia gravity wave with slightly negative Richardson number in the wind field, and this wave strongly produced turbulence through instabilities. It seems to be possible that magnitude of gravity waves in the background wind field could change the situation whether the motion of the scattering pattern is parallel to the background wind or not.

4.6 Discussion and concluding remarks

MU radar observations of the mesosphere with high time and range resolution have shown that inertia gravity waves can be detected in the wind profile. The intrinsic period and the propagating direction of these waves were determined by using the linear polarization equations of gravity waves. The amplitudes of

the inertia gravity waves did not seem to increase with height, which implies that the waves are saturated and lose their energy. It is found that the scattering layers are detected at the altitudes of small Richardson number modified by the inertia gravity waves.

When the amplitude of the inertia gravity wave is relatively small, that is the minimum Richardson number associated with the wave is larger than one, the wave generates a narrow altitude region with smaller Richardson number relative to those in the surrounding altitudes. Smaller scale gravity waves superposed on the inertia gravity wave give further modifications of the Richardson number, and generate turbulence regions by dissipating themselves through shear or convective instabilities. Two cases shown in Section 4.4 correspond to the condition described above. When a monochromatic inertia gravity wave is dominant in the wind fields, scattering regions in 4.4.1 look like layers in the classification of turbulence structures by Röttger *et al.* [1979]. In the case in 4.4.2, we have shown a superposition of scattering layers attributed to various gravity waves, which would be observed as a single thick region if they were observed by an MST radar with height resolution poorer than that used in this study. Differences in structures of the scattering layers of cases in 4.4.1 and 4.4.2 seem to be attributed to characteristics of the wind fields determined by the gravity waves.

On the other hand, the Richardson number induced by the inertia gravity waves sometimes becomes smaller than the critical values for instabilities. The case shown in Section 4.2 corresponded to this condition. We have found that the minimum Richardson number due to the inertia gravity wave was slightly negative, and the turbulence echo power showed a peak at the altitude of the minimum. This implies that the gravity wave is saturated and generates turbulence through instabilities. In the radial wind velocities, we have found fluctuations with a period of 9 min, which show a rapid phase reversal near the minimum Richardson number. Although the fluctuations were very similar to the Kelvin-Helmholtz instabilities observed in the troposphere, it is possible that they were induced by the convective or parametric instabilities. It should be noted that we have not observed the phase reversal in the radial wind fluctuations in the other observations, and the amplitudes of the fluctuations are less than that in this case. Considering the vertical wavelength of the inertia gravity wave, the scattering region of this case is much thicker than those which are confined in the altitudes with the relatively small Richardson number as shown in other cases. Also, we have recognized fine structures in the scattering region in Fig. 4.8. The intense patchy structures could be interpreted as blobs in Röttger's classification [Röttger *et al.*, 1979].

For the data on 8 February 1985, we have applied a new technique to

observe the horizontal motion of scattering layers by fully utilizing the fast beam steerability of the MU radar. The full-correlation analysis technique has allowed us to obtain the horizontal scale and the correlation time of the scattering layers as well as motions. The direction of the horizontal motion of the scattering layers did not agree with that of the background wind velocity, but was associated with the horizontal propagation direction of the inertia gravity wave observed in the wind field. Because the gravity wave showed a negative Richardson number, we inferred that the motion of the scattering pattern we observed was that of the region, where turbulence was being generated by the saturated gravity wave.

From these observations, we have found clear evidence that the structures of the mesospheric scattering layers are closely related to the activity of the inertia gravity waves. Especially, the vertical thickness of the scattering region seems to be associated with the spatial or time scale of the wave which is actually dissipated into turbulence. This study have shown that inertia gravity waves propagating upward from the lower atmosphere saturate in the upper mesosphere, and play important role in depositing their energy into turbulence by shear or convective instabilities.

Chapter 5

Observations with the Kyoto meteor radar

5.1 Introduction

By using the Poker Flat MST radar (65°N, 147°W), power spectral density of gravity waves has been observed [Carter and Balsley, 1982; Balsley and Carter, 1982]. Vincent and Ball [1981] and Vincent [1984a] have studied the gravity wave spectra detected by the partial reflection radar at Adelaide (35°S, 138°E) and Townsville (19°S, 147°E). Frezal *et al.* [1981] also reported meteor radar observations of gravity wave spectra at Monpazier (44°N, 1°E), Kiruna (68°N, 20°E) and Punta Borinquen (18°N, 67°W). All these radar observations have shown similarity of the gravity wave spectra in spite of difference in observation latitudes and heights.

The spectral density, S, is usually described as $S(f) = \alpha f^{-k}$, where α is a constant; k has been found in the range of $1 < k < 2$ [Fritts, 1984]. In order to investigate the contribution of gravity waves to the general circulation of the atmosphere, it is important to observe horizontal phase velocity and horizontal wavelength of gravity waves near the mesopause. Using the partial reflection technique, Vincent and Reid [1983] have shown that dominant horizontal wavelength and phase velocity of gravity waves with periods less than 1 hr are 50 km and 50 ms^{-1}, respectively. However, the estimate of wavelength longer than 200 km was uncertain because of the short beam spacing of approximately 35 km in their radar experiment.

The Kyoto meteor radar has been continuously monitoring the zonal component of the wind fields at the 80–110 km altitudes since May 1983. A great deal of data accumulated in the long duration observations can be utilized for the analysis of gravity waves as well as tides and long-period oscillations [Tsuda

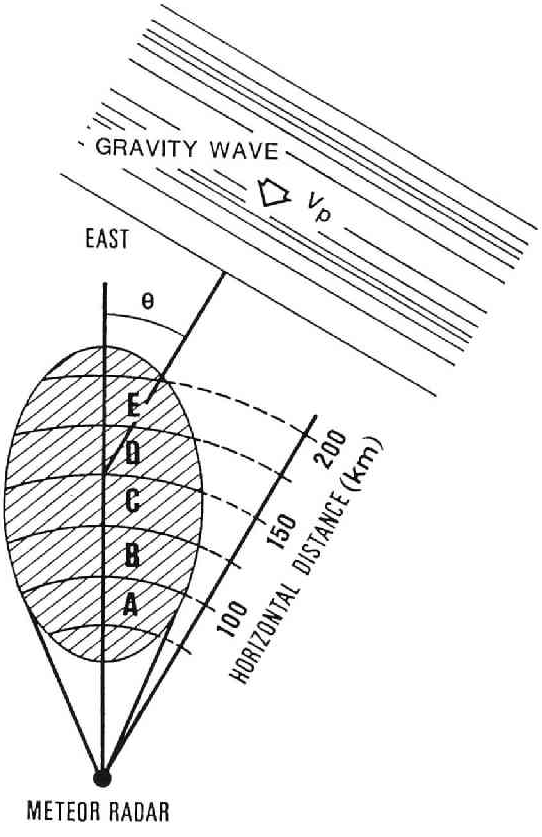

Figure 5.1: Schematic diagram of the illuminating area of the Kyoto meteor radar at the 90–100 km altitude region. This area is divided into five sub-areas to detect the apparent phase velocity.

et al., 1983; Ito *et al.*, 1984], although the time and height resolutions are not as good as those of the MST radars. By using the data of the Kyoto meteor radar, Yamamoto *et al.* [1986] have investigated the power spectral density of eastward component of gravity waves in the period from May 1983 to April 1985. Furthermore, they have developed a new technique to observe an apparent zonal phase velocity of gravity waves by utilizing the large horizontal spread of illuminating area of the Kyoto meteor radar.

5.2 Power spectral density

An ellipse in Fig. 5.1 schematically shows the illuminating area of the Kyoto meteor radar at meteor heights. The altitude distribution of meteor echoes is

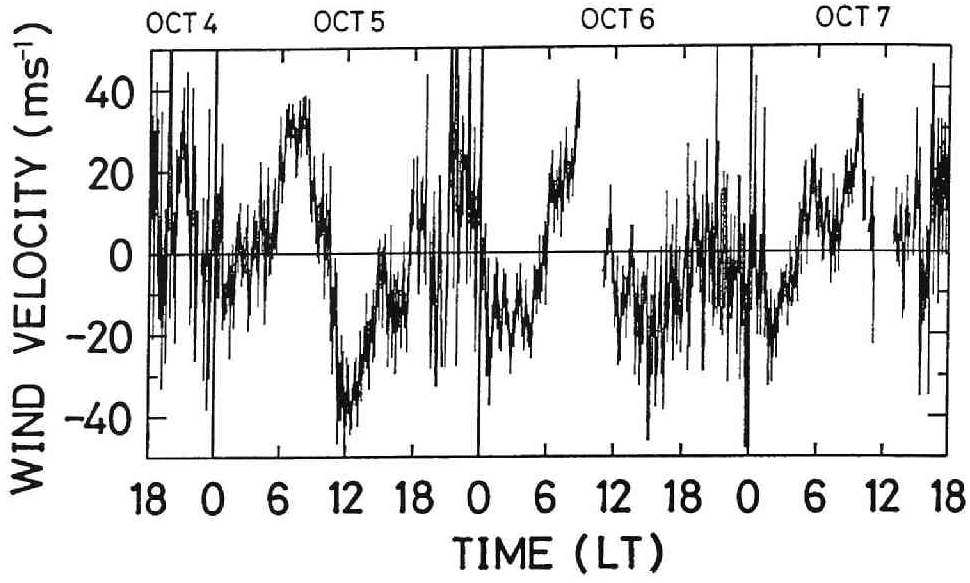

Figure 5.2: The eastward wind velocity detected every 10 min at 90–100 km altitude observed on 4–7 October 1983. Vertical bars indicate the standard deviation.

approximately Gaussian, with a maximum at around 95 km and a standard deviation of several kilometers. Only meteor echoes detected at 90–100 km altitude, where most of them are observed, are used for the analysis of the power spectral density and horizontal phase velocity of gravity waves.

There are two techniques to determine a meteor echo height. Measurements of the range and the arrival angles of the meteor echo by a radio interferometer can give height, elevation and azimuth angles. The decay-height method, which utilizes a relation between altitude and the decay time constant of the echo intensity, gives height and elevation angle. Although the former determines the echo height more accurately than the latter, the number of meteor echoes becomes fairly small, because it needs a better signal-to-noise ratio than the decay-height method. We have adopted the decay-height method for the analysis, since the limited data obtained using the interferometer makes it difficult to adequately determine the power spectral density of the wind fields.

The data length for the analysis of spectra is 72 hr, beginning at 18 LT. The line-of-sight velocity determined from each meteor echo is averaged over 10 min, then converted into the eastward wind velocity assuming zero vertical wind velocity. Figure 5.2 shows an example of the eastward wind field observed on 4–7 October 1983. An autocorrelation function of the wind field is calculated, and it is then transformed to the power spectral density by using FFT. As

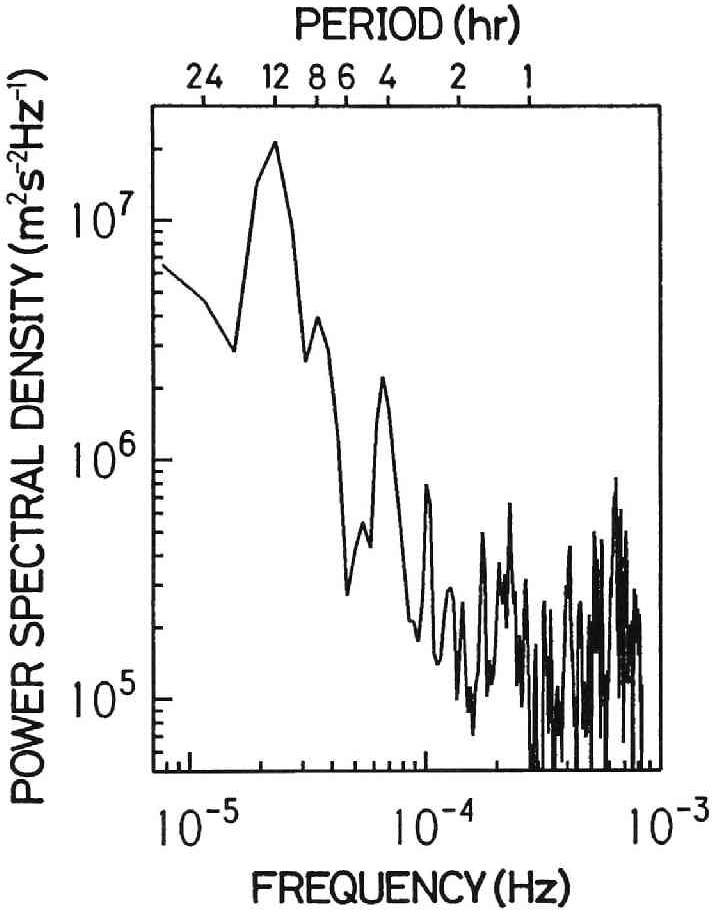

Figure 5.3: Power spectral density of the wind field shown in Fig. 5.2.

shown in Fig. 5.3, the semidiurnal tide is the most intense component. A spectral peak at a period of about 4 hr is isolated in the spectrum. However, the spectral density in the period range 2–12 hr generally decreases with wave frequency.

Each spectral density determined on a three-day basis is accumulated in the periods from May 1983 to February 1984 and from May 1984 to April 1985. The spectra obtained in March and April 1984 are removed from the averaging, because the amount of data was not sufficient to give significant results. As shown in Fig. 5.4, these results agree well with each other in both periods. The component with wave periods less than 2 hr remains almost constant with frequency, which suggests this high frequency part may be contaminated by noise due to the insufficient time resolution of the Kyoto meteor radar. Figure 5.4 also shows the summer average of spectra at 86 km observed at Poker Flat [Carter and Balsley, 1982] and the annual mean at 85 km at Adelaide and Townsville [Vincent, 1984a]. On average, the intensity of the power spectral density detected at Kyoto is smaller than that in the other observations. This could be attributed to filtering of the gravity wave component with smaller horizontal and vertical scales than those of the horizontal observation area shown in Fig. 5.1 and also a vertical extent of 10 km. However, the spectral density observed at Kyoto varies similarly with frequency. The semidiurnal tide shows a sharp spike in the spectra, resembling the Poker Flat observations. An approximately linear relation in the 2–8 hr period seems to be extended to longer period components trough the base of the semidiurnal tide. The spectra in the periods 2–18 hr are approximated as $1.87f^{-1.29}$ and $2.11f^{-1.27}[\mathrm{m^2s^{-2}Hz^{-1}}]$ in 1983 and 1984, respectively, where the conspicuous peak at 12 hr is removed in the fitting.

Figure 5.5 shows the seasonal variation of the power spectral density averaged bimonthly where only components in the wave periods of 2–36 hr are plotted. The semidiurnal tide seems to show seasonal variation, with a maximum in September and October in both years. On the other hand, components with periods smaller than 6 hr do not show a clear seasonal variation. From meteorological rocket observations in the 20–65 km altitude range, Hirota [1984] statistically analyzed the root mean square (rms) amplitude of wind velocity and the temperature fluctuations with vertical wavelengths shorter than 10 km. Hirota showed that the activity and variability of gravity waves were small at mid-latitudes, in contrast to higher latitudes in which there was a notable annual variation. Although the altitude range is different from our observations and the period is not specified in Hirota's analysis, his result is consistent with our observations.

Figure 5.5 also shows the bimonthly values of the coefficients k and α sim-

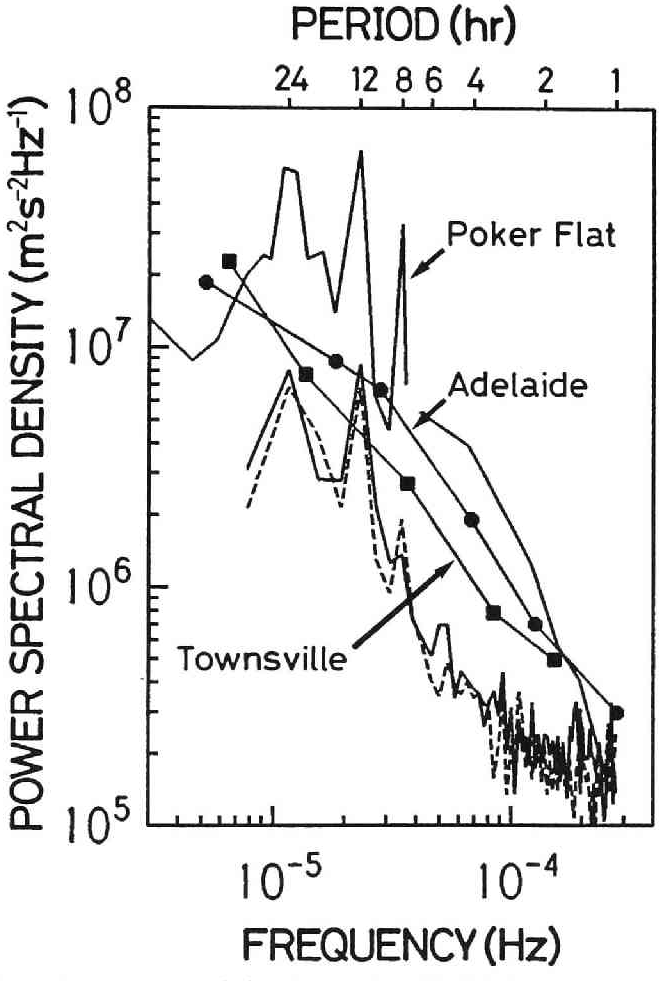

Figure 5.4: Power spectral density in the 90–100 km region averaged in the periods from May 1983 to February 1984 (solid curve) and from May 1984 to April 1985 (dashed curve), accompanied with the annual mean power spectra at Adelaide and Townsville [Vincent, 1984a] and summer average at Poker Flat [Carter and Balsley, 1982].

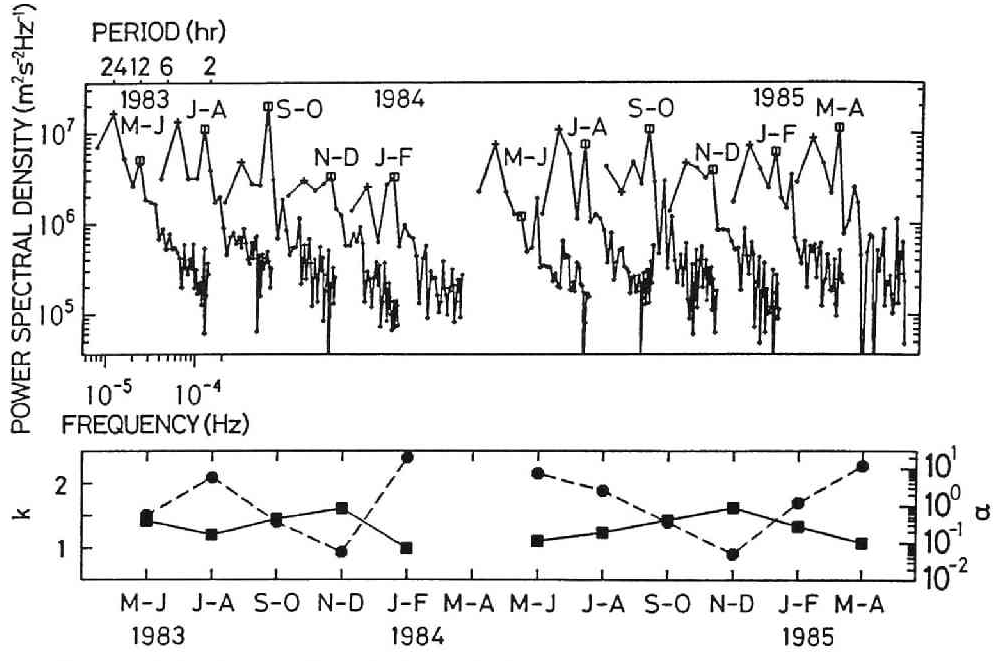

Figure 5.5: Seasonal variation of the power spectral density in the 90–100 km region averaged for every two months for the components with wave periods 2–36 hr (top panel). The horizontal axis of each spectrum should be shifted. Cross and square symbols correspond to diurnal and semidiurnal tides, respectively. Bottom panel shows coefficients α (dashed curve) and k (solid curve) of the fitted curve in the wave periods 2–18 hr, excluding the semidiurnal component.

ilarly calculated as in Fig. 5.4. In November and December in both 1983 and 1984, k becomes slightly large than in other months. The seasonal variations of both k and α seem to be repeated for two years, and α becomes large when k is small.

5.3 Apparent zonal phase velocity

The horizontal extent of the illuminating area of the Kyoto meteor radar ranges from 75 to 200 km in the direction of the antenna main beam. As shown in Fig. 5.1, this area is divided into five sub-areas with a horizontal width of 25 km according to distance from the radar. When a monochromatic gravity wave propagates at an angle of θ relative to the eastward direction, its apparent horizontal phase velocity V_{pa} becomes $V_p/\cos\theta$, where V_p is the ac-

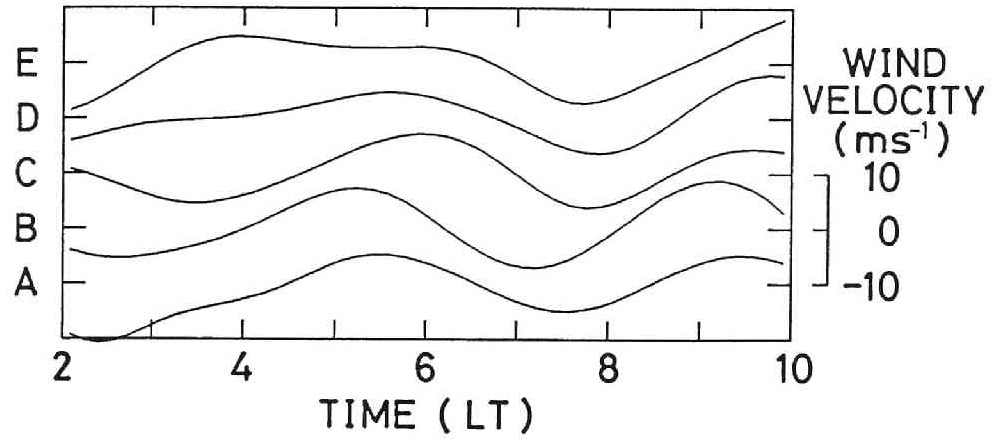

Figure 5.6: Band pass filtered wind fields observed on 7 October 1983 in the five sub-areas shown in Fig. 5.1.

tual horizontal phase velocity in the propagation direction. For the analysis of V_{pa}, the data length is 24 hr, beginning at 18 LT. In order to detect a monochromatic gravity wave, we have calculated the power spectrum of the wind field observed in the whole illuminating area in each day and selected a dominant isolated spectral peak with wave periods of 2–8 hr. Components with periods less than 2 hr are excluded as smaller scale perturbations than the time resolution of the Kyoto meteor radar. Components larger than 12 hr are also excluded so as to remove atmospheric tides. The wind field in each sub-area is processed through a numerical band-pass filter which extracts the specified component. Figure 5.6 shows an example of the wind fields obtained in each sub-area on 7 October 1983. The phase difference between wind fields can be seen. By using the data taken between 0 and 12 LT, a cross-correlation function among filtered wind fields in five sub-areas is calculated. Figure 5.7 shows the cross-correlation function for the wind fields shown in Fig. 5.6. A time lag between wind fields detected in two sub-areas is determined when the maximum of the cross correlation exceeds 0.7. The time lags are not calculated when the total period in which meteor echoes are not available exceeds 30% of the period from 0 to 12 LT. At most, ten time lags can be determined. A least squares fitting is applied for a linear relation between time lags and horizontal distances using a weighting function proportional to the cross-correlation value. The apparent zonal phase velocity corresponds to the inverse of the inclination of the fitted curve. In Fig. 5.7, the value can be inferred as 29 ms^{-1} in the eastward direction.

Because the horizontal separation of the sub-areas is 25 km, the detectable

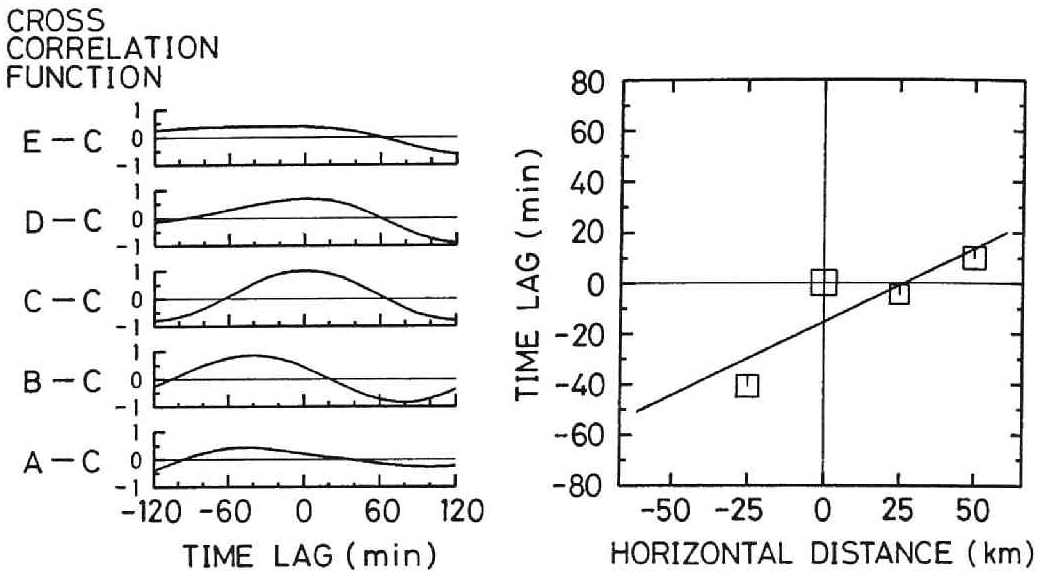

Figure 5.7: Cross-correlation functions of the wind fields in the five sub-areas shown in Fig. 5.6 (left panel), and the time lag versus the horizontal distance (right panel), where the horizontal distance is measured from the sub-area C. The linear curve shows a least squares fitting.

shortest apparent wavelength is 50 km. Assuming a wave period of several hours, this implies that the gravity waves with a phase velocity less than approximately 5 ms^{-1} cannot be detected in our analysis. Considering that the accuracy in the time lag calculation is approximately 20 min, and the largest spacing is 100 km between the sub-areas A and E, a phase velocity exceeding 100 ms^{-1} seems to be uncertain.

The apparent zonal phase velocities for monochromatic gravity waves have been determined in 99 cases during the period from May 1983 to April 1985, and are shown in Fig. 5.8 as a histogram. As a whole, dominant values of V_{pa} are 20 ± 5 ms^{-1} and 30 ± 5 ms^{-1} in the eastward and westward directions, respectively. Gravity waves propagating westward are more frequently recognized than eastward propagating ones. Seasonal mean distributions of V_{pa} are also shown in Fig. 5.8 for summer months (May–August), winter months (November–February) and equinoxes (March–April and September–October). In winter months, the westward propagating gravity waves are dominant, while there seems no clear tendency in the summer months and the equinoxes.

Figure 5.9 shows a histogram of the wave period T for monochromatic gravity waves, where the dominant periods are seen to be in the range 3.4–

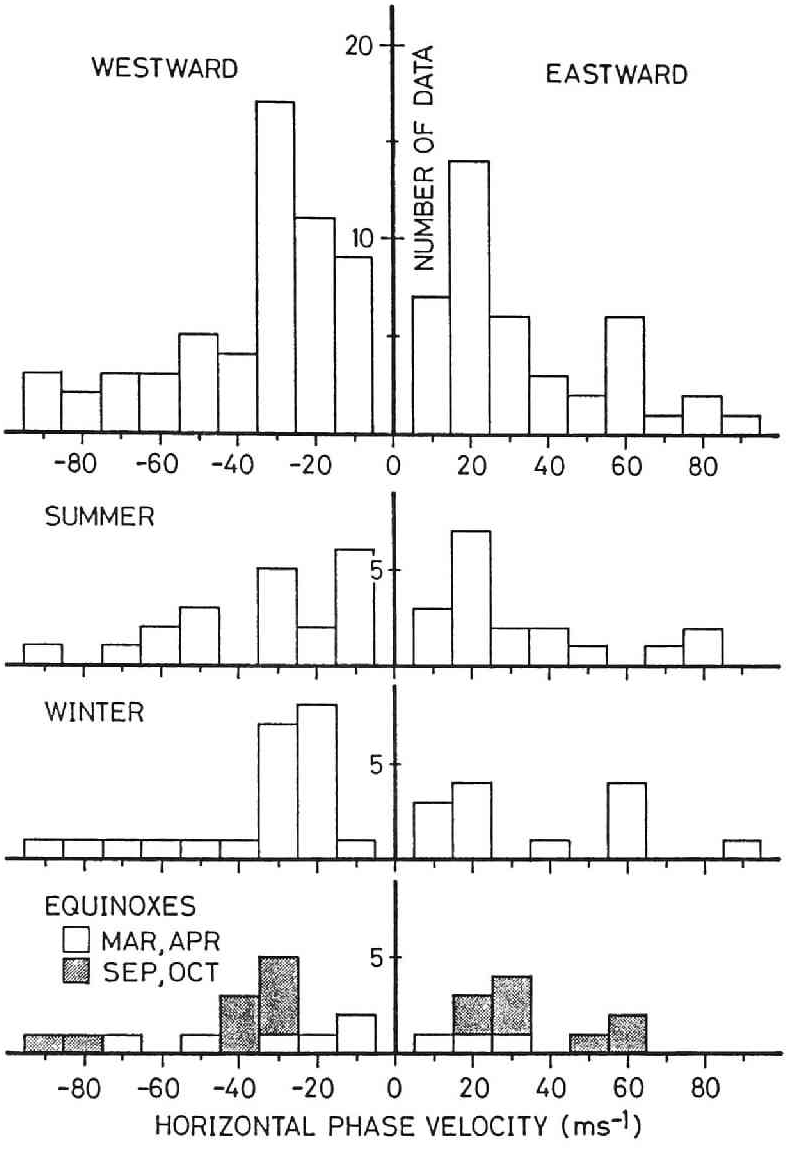

Figure 5.8: Occurrence frequency of the apparent zonal phase velocity of gravity waves during the period from May 1983 to April 1985. Distributions are separately shown for the whole observation period (top panel), summer months (May–August), winter months (November–February) and equinoxes (March–April and September–October). A positive phase velocity corresponds to eastward propagation.

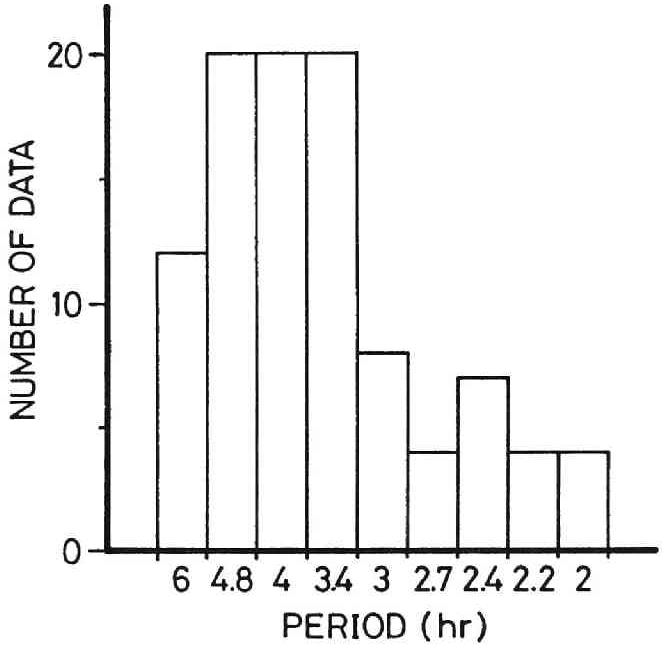

Figure 5.9: Occurrence frequency of the wave period of monochromatic gravity waves during May 1983–April 1985.

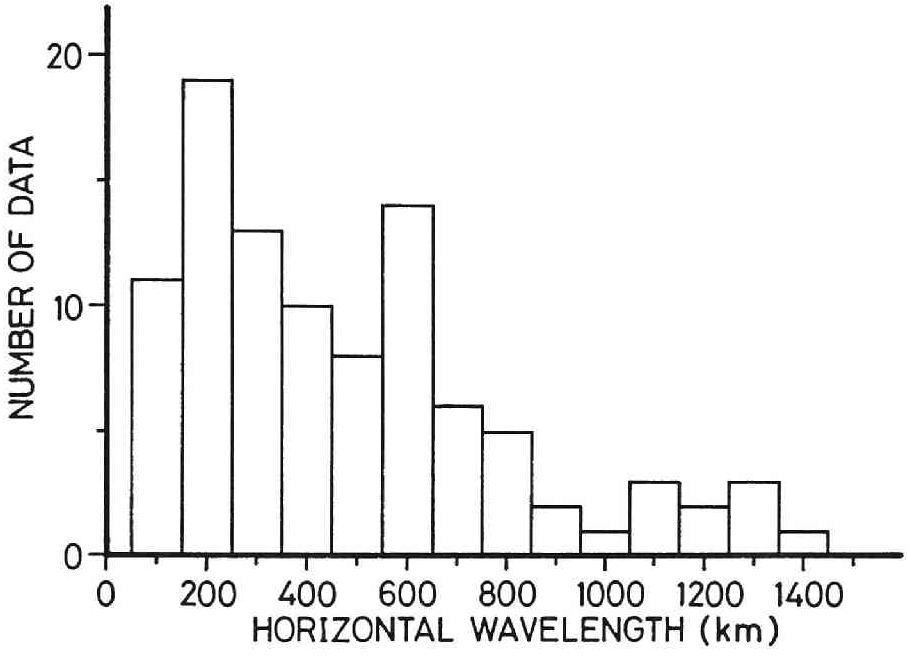

Figure 5.10: The same as Fig. 5.9 except for the apparent horizontal wavelength.

4.8 hr. Figure 5.10 shows the occurrence frequency of the apparent wavelength λ. The number of gravity waves seems to become large when their wavelength becomes small, although peaks in the distribution at 200 ± 50 km and 600 ± 50 km can be recognized. Assuming typical values of V_{pa} and T as 25 ms^{-1} and 4 hr, respectively, λ is inferred as approximately 360 km. Because V_{pa} is usually larger than the actual phase velocity in the propagating direction, this value could be an overestimate. Using two oblique beams with a partial reflection radar, Vincent and Reid [1983] observed a wavelength of approximately 200 km for gravity waves with a period of 4 hr. The result with the Kyoto meteor radar is consistent with their observation.

For every two months, the inverse of the eastward apparent phase velocity V_{pe} (> 0) and the westward phase velocity V_{pw} (< 0) are separately added as

$$S_e = \sum \frac{1}{V_{pe}} \tag{5.1}$$

$$S_w = \sum \frac{1}{V_{pw}} \tag{5.2}$$

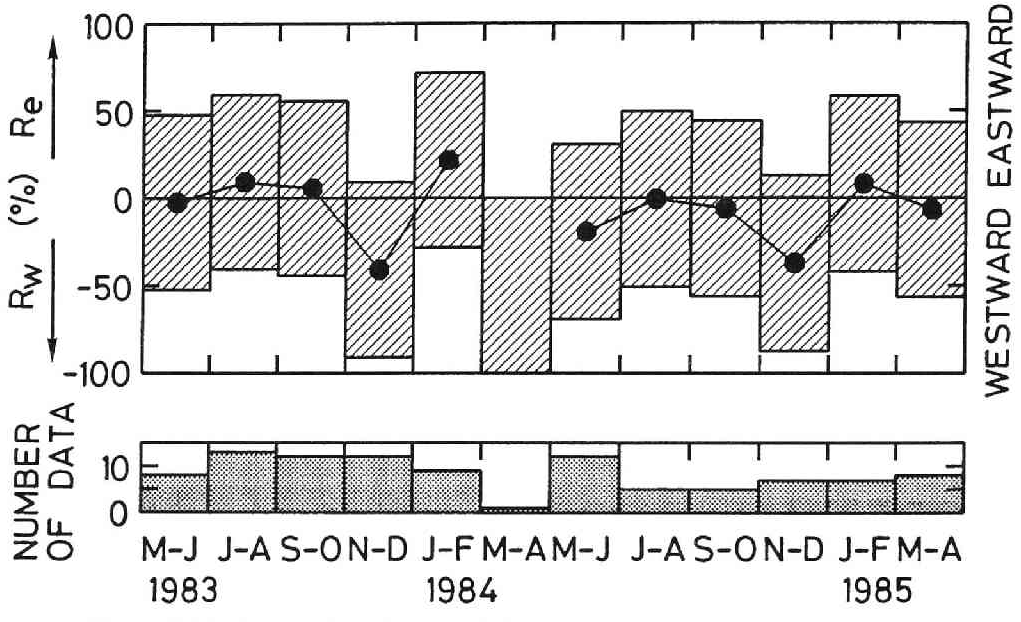

Figure 5.11: Seasonal variation of the percentage occurrence of apparent eastward and westward phase velocities (top panel). The circle denotes the average of R_e and R_w. The number of gravity waves used in the analysis is shown in the bottom panel.

The ratios R_e and R_w are calculated as follows:

$$R_e = \frac{S_e}{S_e - S_w} \tag{5.3}$$

$$R_w = \frac{S_w}{S_e - S_w} \tag{5.4}$$

R_e or R_w indicate the occurrence frequency of the eastward or westward propagating gravity waves weighted by the inverse of the apparent phase velocity. Figure 5.11 shows the seasonal variation of the R_e and R_w. The value in March and April 1984 is not reliable, because only one monochromatic gravity wave was detected. A similar seasonal variation is recognized in both years, such that westward phase velocities are dominant in November and December as has been already described in Fig. 5.8.

5.4 Concluding remarks

In this chapter, we have studied power spectral density, wave period, apparent zonal phase velocity and apparent zonal wavelength of gravity waves observed by the Kyoto meteor radar at altitudes in the range 90–100 km from May 1983 to April 1985. The annual mean power spectra observed at Kyoto decrease with frequency, similarly to the results at Poker Flat, Adelaide and Townsville. The linearly fitted curves of the spectra in the periods 2–18 hr show a small year-by-year variation. The spectral peak corresponding to the semidiurnal tide exceeds the linearly fitted curves, which agrees with the Poker Flat observations. However, absolute comparison of the spectral intensity seems to be difficult, because the time-height resolution of the Kyoto meteor radar observation is not as good as other observations. Monochromatic gravity waves with periods ranging from 3.4 to 4.8 hr are most frequently observed. Using the advantage of large horizontal extension of the illuminating area of the Kyoto meteor radar, we have developed a new technique to determine the apparent zonal phase velocities. Over the whole observation period the typical apparent phase velocity and zonal wavelength have been 25 ms^{-1} and 360 km, respectively. Westward propagating gravity waves are dominant in winter months, especially in November and December.

Chapter 6

Summary and conclusions

This thesis was concerned with radar observation of gravity waves in the middle atmosphere. Two types of radars, the MU radar and the Kyoto meteor radar, were utilized for the observations.

In Chapter 1, general introduction was presented to show the characteristics of the middle atmosphere. Basic equations of gravity waves and a linear theory of the mean wind acceleration due to the breaking of gravity waves were briefly reviewed. Radar techniques to observe wind velocities in the mesosphere, and the observational results were also shown in this chapter.

The MU radar system was shown in Chapter 2. Hardware configuration of the MU radar was described with a detailed explanation of the antenna array system driven by the solid-state power amplifiers. The programs to control the MU radar system are shown as software configuration since the MU radar requires sophisticated computer control owing to its flexibility.

In Chapter 3, data processing techniques used in the mesospheric observations were shown. They consist of techniques to obtain wind velocities from the echo power spectra. The estimation error of the spectral parameters was discussed by means of computer simulations. It was shown that the least squares fitting method was better than the moment method in the region with low signal-to-noise ratio (SNR), especially for narrow spectra. However, the estimation error of the fitting method at infinite SNR was approximately twice that of the moment method. An attempt was made to achieve the theoretical lower bound of the estimation error, which showed 20 times smaller errors in the wind velocities than those of the moment method. As a performance evaluation of the MU radar, comparison observations between the MU radar and the Kyoto meteor radar were shown in this chapter. They showed fairly consistent wind profiles in 65–105 km region. The wind profile observed by a meteorological rocket sounding at Ryori also showed overall continuity to the

winds observed by the MU radar.

Chapter 4 was devoted to the gravity wave observations by using the MU radar. Mesospheric observations with good time-height resolution have found that inertia gravity waves play an important role in producing turbulence layers in the mesosphere. By calculating the Richardson number in the presence of the inertia gravity waves, it was found that scattering layers appeared around the altitude of the minimum Richardson number, and showed descending motions at the vertical phase velocity of the monochromatic inertia gravity waves. A mixture of several scattering layers with different descending motions was observed when wind fields consist of several gravity waves with different vertical wavelengths and phase velocities. The inertia gravity waves in the mesosphere generated the altitude region with relatively small Richardson number, where smaller scale perturbations superposed on the wave seemed to generate instabilities, and produce turbulence. On the other hand, when the Richardson number became slightly negative, the wave itself is dissipated through instabilities, and produces thicker turbulent layer than that in other cases. The radial wind velocities showed large fluctuations with a period of 9 min, which showed a phase reversal near the altitude of minimum Richardson number. The fluctuations seemed to be attributed to the shear or convective instabilities generated by the saturated gravity wave. In order to observe the horizontal structure of the scattering pattern as well as their horizontal motions, a full-correlation analysis technique was applied to the echo power fluctuations. The motion of the scattering pattern did not agree with the background wind velocity, but rather was associated with the propagation direction of the saturated inertia gravity wave. The correlation time of the moving scattering pattern was approximately 700 s, which is much longer than the correlation time of the turbulence itself. This implied that the observed scattering pattern is associated with a region where the inertia gravity wave produced turbulence.

In Chapter 5, gravity wave observations by using the Kyoto meteor radar were presented. The annual mean power spectral densities of the eastward wind velocity were calculated for 1983 and 1984, and were approximated as $1.87f^{-1.29}$ and $2.11f^{-1.27}[\mathrm{m^2s^{-2}Hz^{-1}}]$, respectively. By dividing the observation range of the Kyoto meteor radar into five sub-areas according to the horizontal distance from the radar, the apparent zonal phase velocities of monochromatic gravity waves were determined. Typical values of apparent zonal phase velocity and wave period were 25 $\mathrm{ms^{-1}}$ and 4 hr, respectively. Gravity waves with westward phase velocities have been more frequently detected than that with eastward ones in the whole observation period; especially, they dominated in November and December in both 1983 and 1984.

In conclusion, we have examined the performance of the MU radar for the

mesospheric observations, and studied the behavior of gravity waves in this region. We could establish techniques to detect the gravity waves by using both the MU radar and the Kyoto meteor radar. It was clearly found that the gravity waves were dissipated in the mesosphere, and depositing their energy to produce turbulence. Theoretically, it is known that the mean flow acceleration is the most important role of gravity waves in the middle atmosphere. Further observations of the momentum flux of gravity waves are required to confirm this role. Continuous mesospheric observations are also required to study in more detail the statistical characteristics and the seasonal variation of gravity wave parameters, e.g., their activity, wavelength, period, horizontal propagation direction, and the momentum flux.

References

Aso, T., T. Tsuda and S. Kato, Meteor radar observations at Kyoto University, *J. Atmos. Terr. Phys.*, **41**, 517–525, 1979.

Aso, T., T. Tsuda, Y. Takashima, R. Ito and S. Kato, Observations of lower ionospheric wind by the Kyoto meteor radar, *J. Geophys. Res.*, **85**, 177–184, 1980.

Aso, T. and R. A. Vincent, Some direct comparisons of mesospheric winds observed at Kyoto and Adelaide, *J. Atmos. Terr. Phys.*, **44**, 267–280, 1982.

Avery, S. K., A. C. Riddle and B. B. Balsley, The Poker Flat, Alaska, MST radar as a meteor radar, *Radio Sci.*, **18**, 1021–1027, 1983.

Balsley, B. B. K. S. Gage, The MST radar technique: Potential for middle atmosphere studies, *Pure Appl. Geophys.*, **118**, 452–493, 1980.

Balsley, B. B. and D. A. Carter, The spectrum of atmospheric velocity fluctuations at 8 km and 86 km, *Geophys. Res. Lett.*, **9**, 465–468, 1982.

Balsley, B. B, W. L. Ecklund and D. C. Fritts, VHF echoes from the high-latitude mesosphere and lower thermosphere: Observations and interpretations, *J. Atmos. Sci.*, **40**, 2451–2466, 1983.

Balsley, B. B. and A. C. Riddle, Monthly mean values of the mesospheric wind field over Poker Flat, Alaska, *J. Atmos. Sci.*, **41**, 2368–2375, 1984.

Beer, T., *Atmospheric waves*, 300pp., Adam Hilger Ltd., London, 1974.

Bendat, J. S. and A. G. Piersol, *Random data: Analysis and measurement procedures*, pp. 189–193, Wiley-Interscience, New York, 1971.

Bender, C. M. and S. A. Orszag, *Advanced mathematical methods for scientists and engineers*, 593pp., McGraw-Hill, New York, 1978.

Briggs, B. H., Radar observations of atmospheric winds and turbulence: a comparison of techniques, *J. Atmos. Terr. Phys.*, **42**, 823–833, 1980.

Briggs, B. H., The analysis of spaced sensor records by correlation techniques, *Handbook for MAP*, **13**, 166–186, 1984.

Briggs, B. H., G. J. Phillips and D. H. Shinn, The analysis of observations on spaced receivers of the fading of radio signals, *Proc. Phys. Soc. London*, **B63(2)**, 106–121, 1950.

Carter, D. A.,and B. B. Balsley, The summer wind field between 80 and 93 km observed by the MST radar at Poker Flat, Alaska (65°N), *J. Atmos. Sci.*, **39**, 2905–2915, 1982.

CIRA, *COSPAR International Reference Atmosphere*, Akademie-Verlag, Berlin, 1972.

Countryman, I. D. and P. M. Dolas, Observations on tides in the equatorial mesosphere, *J. Geophys. Res.*, **87**, 1336–1342, 1982.

Craig, R. L. and W. G. Elford, Observations of the quasi 2-day wave near 90 km altitude at Adelaide (35°S), *J. Atmos. Terr. Phys.*, **43**, 632–641, 1981.

Czechowsky, P., R. Rüster and G. Schmidt, Variations of mesospheric structures in different seasons, *Geophys. Res. Lett.*, **6**, 459–462, 1979.

Czechowsky, P., G. Schmidt and R. Rüster, The mobile SOUSY Doppler radar: Technical design and first results, *Radio Sci.*, **19**, 441–450, 1984.

Dolas, P. M. and R. G. Roper, Prevailing wind in the meteor zone (80–100 km) over Atlanta and its association with midwinter stratospheric warming, *J. Atmos. Sci.*, **38**, 182–188, 1981.

Doviak, R. J. and D. S. Zrnić, *Doppler radar and weather observations*, pp. 113–115, Academic Press, Orlando, 1984.

Drazin, P. G., The stability of a shear layer in an unbounded heterogeneous inviscid fluid, *J. Fluid Mech.*, **4**, 214–224, 1958.

Elford, W. G., Prevailing winds in lower thermosphere, *Nature*, **261**, 123–124, 1976.

Farley, D. T., Multiple-pulse incoherent-scatter correlation function measurements, *Radio Sci.*, **7**, 661–666, 1972.

Felgate, D. G., A. N. Hunter, S. P. Kingsley and H. G. Muller, Comparative studies of E-region ionospheric drifts and meteor winds, *Planet. Space Sci.*, **23**, 389–400, 1975.

Forbes, J. M., Middle atmosphere tides, *J. Atmos. Terr. Phys.*, **46**, 1049–1067, 1984.

Fraser, G. J., The measurement of atmospheric winds at altitudes of 64–120 km using ground-based radio equipment, *J. Atmos. Sci.*, **22**, 217–218, 1965.

Fraser, G. J., Seasonal variation of southern hemisphere mid-latitude winds at altitudes of 70–100 km, *J. Atmos. Terr. Phys.*, **30**, 707–719, 1968.

Frezal, M. E., M. Glass, J. L. Fellous and M. Massebeuf, Simultaneous meteor radar observations at Monpazier (France, 44°N) and Punta Borinquen (Puerto Rico, 18°N). III-The latitudinal variations of the energy of gravity waves (2–8 h) in the high mesosphere, *J. Atmos. Terr. Phys.*, **43**, 543–547, 1981.

Fritts, D. C., Gravity wave saturation in the middle atmosphere: a review of theory and observations, *Rev. Geophys. space phys.*, **22**, 275–308, 1984.

Fritts, D. C. and P. K. Rastogi, Convective and dynamical instabilities due to gravity wave motions in the lower and middle atmosphere: Theory and observations, *Radio Sci.*, **20**, 1247–1277, 1985.

Fritts, D. C. and R. A. Vincent, Mesospheric momentum flux studies at Adelaide, Australia: Observations and a gravity wave-tidal interaction model, *J. Atmos. Sci.*, **44**, 605–619, 1987.

Fukao, S., T. Sato, S. Kato, R. M. Harper, R. F. Woodman and W. E. Gordon, Mesospheric winds and waves over Jicamarca on May 23–24, 1974, *J. Geophys. Res.*, **84**, 4379–4386, 1979.

Fukao, S., T. Sato, I. Hirota and S. Kato, A preliminary radar observation of long-period waves in the tropical mesosphere over Jicamarca, *J. Geophys. Res.*, **85**, 1955–1957, 1980a.

Fukao, S., S. Kato, T. Aso, M. Sasada, and T. Makihira, Middle and upper atmosphere radar (MUR) under design in Japan, *Radio Sci.*, **15**, 225–231, 1980b.

Fukao, S., Y. Maekawa, T. Sato and S. Kato, Fine structure in mesospheric wind fluctuations observed by the Arecibo UHF Doppler radar, *J. Geophys. Res.*, **90**, 7547–7556, 1985a.

Fukao, S., T. Sato, T. Tsuda, S. Kato, K. Wakasugi and T. Makihira, The MU radar with an active phased array system, 1. Antenna and power amplifiers, *Radio Sci.*, **20**, 1155–1168, 1985b.

Fukao, S., T. Tsuda, T. Sato, S. Kato, K. Wakasugi and T. Makihira, The MU radar with an active phased array system, 2. In-house equipment, *Radio Sci.*, **20**, 1169–1176, 1985c.

Fukao, S., T. Sato, T. Tsuda, M. Yamamoto and S. Kato, High resolution turbulence observations in the middle and lower atmosphere by the MU radar with fast beam steerability: Preliminary results., *J. Atmos. Terr. Phys.*, **48**, 1269–1278, 1986.

Fukuyama, K., Incoherent scatter radar observations of wavelike structures in the mesosphere over Arecibo, *J. Geophys. Res.*, **86**, 9152–9158, 1981.

Gage, K. S. and T. E. VanZandt, Wind measurement techniques available for the Middle Atmosphere Program, *J. Geophys. Res.*, **86**, 9591–9598, 1981.

Gage, K. S. and B. B. Balslay, MST radar studies of wind and turbulence in the middle atmosphere, *J. Atmos. Terr. Phys.*, **46**, 739–753, 1984.

Gossard, E. E. and W. H. Hooke, *Waves in the atmosphere*, 456pp., Elsevier, New York, 1975.

Groves, G. V., Wind models from 60 to 130 km altitude for different months and latitudes, *J. Brit. Interplanet. Soc.*, **22**, 285–307, 1969.

Harper, R. M. and R. F. Woodman, Preliminary multiheight radar observations of waves and winds in the mesosphere over Jicamarca, *J. Atmos. Terr. Phys.*, **39**, 959–963, 1977.

Hines, C. O., Internal atmospheric gravity waves at ionospheric heights, *Can. J. Phys.*, **38**, 1441–1481, 1960.

Hirota, I., Climatology of gravity waves in the middle atmosphere, *J. Atmos. Terr. Phys.*, **46**, 767–773, 1984.

Hirota, I., Y. Maekawa, S. Fukao, K. Fukuyama, M. P. Sulzer, J. L. Fellous, T. Tsuda and S. Kato, Fifteen-day observation of mesospheric and lower thermospheric motions with the aid of the Arecibo UHF radar, *J. Geophys. Res.*, **88**, 6835–6842, 1983.

Hocking, W. K., Measurement of turbulent energy dissipation rates in the middle atmosphere by radar techniques: A review, *Radio Sci.*, **20**, 1403–1422, 1985.

Hodges, R. R., Jr., Generation of turbulence in the upper atmosphere by internal gravity waves, *J. Geophys. Res.*, **72**, 3455–3458, 1967.

Holton, J. R., The role of gravity wave-induced drag and diffusion in the momentum budget of the mesosphere, *J. Atmos. Sci.*, **39**, 791–799, 1982.

Houghton, J. T., The stratosphere and mesosphere, *Q. J. R. Meterol. Soc.*, **104**, 1–29, 1978.

Ito, R., T. Tsuda, T. Aso and S. Kato, Long period oscillations in the meteor winds observed over Kyoto during 1978–1983, *J. Geomag. Geoelectr.*, **36**, 173–188, 1984.

Kato, S., *Dynamics of the upper atmosphere*, 233pp., D. Reidel Publ. Co., Dordrecht, 1980.

Kato, S., T. Ogawa, T. Tsuda, T. Sato, I. Kimura and S. Fukao, The middle and upper atmosphere radar: First results using a partial system, *Radio Sci.*, **19**, 1475–1484, 1984.

Kato, S., T. Tsuda, M. Yamamoto, T. Sato and S. Fukao, First results obtained with a middle and upper atmosphere (MU) radar, *J. Atmos. Terr. Phys.*, **48**, 1259–1267, 1986.

Klostermeyer, J. and R. Rüster, Radar observation and model computation of a jet stream-generated Kelvin-Helmholtz instability, *J. Geophys. Res.*, **85**, 2841–2846, 1980.

Klostermeyer, J. and R. Rüster, Further study of a jet stream-generated Kelvin-Helmholtz instability, *J. Geophys. Res.*, **86**, 6631–6637, 1981.

Klostermeyer, J. and R. Rüster, VHF radar observation of wave instability and turbulence in the mesosphere, *Adv. Space Res.*, **4**, 79–82, 1984.

Leovy, C. B., Radiative equilibrium of the mesosphere, *J. Atmos. Sci.*, **21**, 327–341, 1964.

Lilly, D. K, D. E. Wako and S. I. Adelfang, Stratospheric mixing estimated from high-altitude turbulence measurements, *J. Appl. Meteor.*, **13**, 488–493, 1974.

Lindzen, R. S., Turbulence and stress owing to gravity wave and tidal breakdown, *J. Geophys. Res.*, **86**, 9707–9714, 1981.

Maekawa, Y., Winds and waves in the tropical middle atmosphere observed by hi-power VHF/UHF Doppler radars, Ph.D. thesis, Dep. of Electr. Eng., Kyoto Univ., Kyoto, Japan, 1985.

Maekawa, Y., T. Aso, J. Röttger, P. Czechowsky, R. Rüster, G. Schmidt, I. Hirota, R. F. Woodman and S. Kato, A cooperative synchronous observation of winds and tides in the tropical lower stratosphere and mesosphere using VHF radars at Jicamarca and Arecibo, *J. Geomag. Geoelectr.*, **38**, 81–97, 1986.

Maekawa, Y., S. Fukao, I. Hirota, M. P. Sulzer and S. Kato, Some further results on long term mesospheric and lower thermospheric wind observations by the Arecibo UHF radar, *J. Atmos. Terr. Phys.*, **49**, 63–71, 1987a.

Maekawa, Y., S. Fukao and S. Kato, Vertical propagation characteristics of internal gravity waves around the mesopause observed by the Arecibo UHF radar, *J. Atmos. Terr. Phys.*, **49**, 73–80, 1987b.

Manning, L. A., O. G. Villard and A. M. Peterson, Meteoric echo study of upper atmospheric winds, *Proc. IRE*, **38**, 877–883, 1950.

Manson, A. H., C. E. Meek and R. J. Stening, The role of atmospheric waves (1.5 h–10 days) in the dynamics of the mesosphere and lower thermosphere at Saskatoon (52°N, 107°W) during four seasons of 1976, *J. Atmos. Terr. Phys.*, **41**, 325–335, 1979.

Manson, A. H, C. E. Meek and J. B. Gregory, Long period oscillations in the mesospheric and lower thermospheric winds (60–100 km) at Saskatoon (52°N, 107°W, L=4.3), *J. Geomag. Geoelectr.*, **33**, 613–621, 1981a.

Manson, A. H., C. E. Meek and J. B. Gregory, Winds and waves (10 min–30 days) in the mesosphere and lower thermosphere at Saskatoon (52°N, 107°W, L=4.4) during the year October 1979 to July 1980, *J. Geophys. Res.*, **86**, 9615–9625, 1981b.

Manson, A. H., C. E. Meek and J. B. Gregory, Gravity waves of short period (5–90 min), in the lower thermosphere at 52°N (Saskatoon, Canada); 1978/1979, *J. Atmos. Terr. Phys.*, **43**, 35–44, 1981c.

Manson, A. H, C. E. Meek, M. Massebeuf, J. L. Fellous, W. G. Elford, R. A. Vincent, R. L. Craig, R. G. Roper, S. Avery, B. B. Balsley, G. J. Fraser, M. J. Smith, R. R. Clark, S. Kato, T. Tsuda and A. Ebel, Mean winds of the upper middle atmosphere (60–110 km): A global distribution from radar systems (M.F., Meteor, VHF), *Handbook for MAP*, **16**, 239–253, 1985.

Massebeuf, M., R. Bernard, J. L. Fellous and M. Glass, The mean zonal circulation in the meteor zone above Garchy (France) and Kiruna (Sweden), *J. Atmos. Terr. Phys.*, **41**, 647–655, 1979.

Matsuno, T. and T. Shimazaki, *Atmospheric science course: 3, Atmosphere in the stratosphere and mesosphere* (in Japanese), 279pp., Tokyo Univ. Publ., Tokyo, 1981.

Matsuno, T., A quasi-one-dimensional model of the middle atmospheric circulation interacting with internal gravity waves, *J. Meterol. Soc. Japan*, **60**, 215–226, 1982.

Miller, K. L., S. A. Bowhill, K. P. Gibbs and I. D. Countryman, First measurements of mesospheric vertical velocities by VHF radar at temperate latitudes, *Geophys. Res. Lett.*, **5**, 939–942, 1978.

Murgatroyd, R. J., The structure and dynamics of the stratosphere, in *The global circulation of the atmosphere*, edited by G. A. Corby, pp. 159–195, Royal Meteorological Society, London, 1969.

Probert-Jones, J. R., The radar equation in meteorology, *Quart. J. Roy. Meteor. Soc.*, **88**, 485–495, 1962.

Rastogi, P. K. and S. A. Bowhill, Gravity waves in the equatorial mesosphere, *J. Atmos. Terr. Phys.*, **38**, 51–60, 1976.

Reid, I. M and R. A. Vincent, Measurements of the horizontal scales and phase velocities of short period mesospheric gravity waves at Adelaide, Australia, *J. Atmos. Terr. Phys.*, **49**, 1033–1048, 1987.

Röttger, Structure and dynamics of the stratosphere and mesosphere revealed by VHF radar investigations, *Pure Appl. Geophys.*, **118**, 494–527, 1980.

Röttger, J., P. K. Rastogi and R. F. Woodman, High-resolution VHF radar observations of turbulence structures in the mesosphere, *Geophys. Res. Lett.*, **6**, 617–620, 1979.

Röttger, J. and H. M. Ierkic, Postset beam steering and interferometer applications of VHF radars to study winds, waves, and turbulence in the lower and middle atmosphere, *Radio Sci.*, **20**, 1461–1480, 1985.

Rüster, R., Winds and waves in the middle atmosphere as observed by ground-based radars, *Adv. Space Res.*, **4**, 3–18, 1984.

Rüster, R. and J. Klostermeyer, Instabilities and turbulence at mesospheric heights as observed by VHF radar, *Handbook for MAP*, **18**, 216–219, 1985.

Sato, T., Coherent radar measurements of the middle atmosphere and design concepts of the MU radar, Ph.D. thesis, Dep. of Electr. Eng., Kyoto Univ., Kyoto, Japan, 1981.

Sato, T. and R. F. Woodman, Spectral parameter estimation of CAT radar echoes in the presence of fading clutter, *Radio Sci.*, **17**, 817–826, 1982.

Schmidt, G., R. Rüster and P. Czechowsky, Complementary code and digital filtering for detection of weak VHF radar signals from the mesosphere, *IEEE Trans. Geosci. Electron.*, **GE-17**, 154–161, 1979.

Skolnik, M. I., *Introduction to radar systems*, 581pp., McGraw-Hill, New York, 1980.

Smith, S. A. and D. C. Fritts, Poker Flat MST radar and meteorological rocketsonde wind profile comparisons, *Geophys. Res. Lett.*, **11**, 538–540, 1984.

Stubbs, T. J., The measurement of winds in the D-region of the ionosphere by the use of partially reflected radio waves, *J. Atmos. Terr. Phys.*, **35**, 909–919, 1973.

Tatarskii, V. I., *The effects of the turbulent atmosphere on wave propagation*, 472pp., U.S. Dep. of Commer., 1971.

Tetenbaum, D., S. K. Avery and A. C. Riddle, Observations of mean winds and tides in the upper mesosphere during 1980–1984, using the Poker Flat,

Alaska, MST radar as meteor radar, *J. Geophys. Res.*, **91**, 14539–14555, 1986.

Tsuda, T., Kyoto meteor radar and its application to observation of atmospheric tides, Ph.D. thesis, Radio Atmospheric Science Center, Kyoto Univ., Uji, Japan, 1982.

Tsuda, T., T. Aso, Y. Takashima, R. Ito and S. Kato, Meteor radar observations at Kyoto in two C.T.O.P. periods, *J. Atmos. Terr. Phys.*, **42**, 461–469, 1980.

Tsuda, T., T. Aso and S. Kato, Seasonal variation of solar atmospheric tides at meteor heights, *J. Geomag. Geoelectr.*, **35**, 65–86, 1983.

Tsuda, T., M. Yamamoto, T. Sato, S. Kato and S. Fukao, Comparison observations between the MU radar and the Kyoto meteor radar, *Radio Sci.*, **20**, 1241–1246, 1985a.

Tsuda, T., K. Hirose, S. Kato and M. P. Sulzer, Some findings on correlation between the stratospheric echo power and the wind shear observed by the Arecibo UHF radar, *Radio Sci.*, **20**, 1503–1508, 1985b.

Tsuda, T., T. Nakamura and S. Kato, Mean winds observed by the Kyoto meteor radar in 1983–1985, *J. Atmos. Terr. Phys.*, **49**, 461–466, 1987a.

Tsuda, T., S. Kato and R. A. Vincent, Long period wind oscillations observed by the Kyoto meteor radar and comparison of the quasi-2-day wave with Adelaide HF radar observations, *J. Atmos. Terr. Phys.*, in press, 1987b.

VanZandt, T. E, J. L. Green, K. S. Gage and W. L. Clark, Vertical profiles of reflectivity turbulence constant: Comparison of observations by the Sunset Radar with a new theoretical model, *Radio Sci.*, **13**, 819–829, 1978.

VanZandt, T. E., J. L. Green, W. L. Clark and J. R. Grant, Buoyancy waves in the troposphere: Doppler radar observations and a theoretical model, *Geophys. Res. Lett.*, **6**, 429–432, 1979.

Vincent, R. A., Gravity-wave motions in the mesosphere, *J. Atmos. Terr. Phys.*, **46**, 119–128, 1984a.

Vincent, R. A., MF/HF radar measurement of the dynamics of the mesopause region—A review, *J. Atmos. Terr. Phys.*, **46**, 961–974, 1984b.

Vincent, R. A., Planetary and gravity waves in the mesosphere and lower thermosphere, *Handbook for MAP*, **16**, 269–277, 1985.

Vincent, R. A. and T. J. Stubbs, P. H. O. Pearson, K. H. Loyd and C. H. Low, A comparison of partial reflection drifts with winds determined by rocket techniques, *J. Atmos. Terr. Phys.*, **35**, 813–821, 1973.

Vincent, R. A. and S. M. Ball, Mesospheric winds at low- and mid-latitudes in the southern hemisphere, *J. Geophys. Res.*, **86**, 9159–9169, 1981.

Vincent, R. A. and T. J. Stubbs, A study of motions in the winter mesosphere using the partial reflection drift technique, *Planet. Space Sci.*, **25**, 441–455, 1977.

Vincent, R. A., and I. M. Reid, HF Doppler measurements of mesospheric gravity wave momentum fluxes, *J. Atmos. Sci.*, **40**, 1321–1333, 1983.

Vincent, R. A., T. Tsuda and S. Kato, A comparative study of mesospheric solar tides observed at Adelaide and Kyoto, *J. Geophys. Res.*, in press, 1987.

Waldteufel, P., An analysis of weather spectra variance in a tornadic storm, *NOAA Tech. Memo*, **ERL NSSL–76**, 80pp., National Severe Storms Laboratory, Norman, Oklahoma, 1976.

Woodman, R. F., High-altitude-resolution stratospheric measurements with the Arecibo 430-MHz radar, *Radio Sci.*, **15**, 417–422, 1980.

Woodman, R. F., Spectral moment estimation in MST radars, *Radio Sci.*, **20**, 1185–1195, 1985.

Woodman, R. F. and A. Guillén, Radar observations of winds and turbulence in the stratosphere and mesosphere, *J. Atmos. Sci.*, **31**, 493–505, 1974.

Wright, J. W., M. Glass and A. Spizzichino, The interpretation of ionospheric radio drift measurements, VIII, Direct comparisons of meteor radar winds and Kinesonde measurements: Mean and random motions, *J. Atmos. Terr. Phys.*, **38**, 713–729, 1976.

Yamamoto, M., T. Tsuda, S. Kato, Gravity waves observed by the Kyoto meteor radar in 1983–1985, *J. Atmos. Terr. Phys.*, **48**, 597–603, 1986.

Yamamoto, M., T. Tsuda, S. Kato, T. Sato and S. Fukao, Interpretation of the structure of mesospheric turbulence layers in terms of inertia gravity waves, *PHYSICA SCRIPTA*, in press, 1987a.

Yamamoto, M., T. Tsuda, S. Kato, T. Sato and S. Fukao, A saturated inertia gravity wave in the mesosphere observed by the MU radar, *J. Geophys. Res.*, **92**, 11993–11999, 1987b.

Yamamoto, M., T. Sato, P. T. May, T. Tsuda, S. Fukao and S. Kato, Estimation error of spectral parameters of MST radars obtained by least squares fitting method and its lower bound, submitted to *Radio Sci.*, 1987c.

Yamamoto, M., T. Tsuda, T. Sato, S. Fukao and S. Kato, Full-correlation analysis of turbulent scattering layers in the mesosphere observed by the

MU radar, submitted to *Pure Appl. Geophys.*, 1987d.

Zrnić, D. S., Estimation of spectral moments for weather echoes, *IEEE Trans. Geosci. Electron., Spec. Issue Radio Meteorol.*, **GE-17**, 113–128, 1979.